Ceramic nanotubes for applications in solar to fuel conversion, batteries, and chemical gas sensing

By

Ibrahim Saleh

A Thesis Submitted to the

Faculty of the Graduate School of the

University of Colorado in partial fulfillment

of the requirement for the degree of

Doctor of Philosophy

Department of Mechanical Engineering

2019

This thesis entitled:

Ceramic nanotubes for applications in solar to fuel conversion, batteries, and chemical gas sensing

Written by Ibrahim Saleh
has been approved for the Department of Mechanical Engineering

_____
Dr. Prashant Nagpal
Department of Chemical and Biological Engineering, University of Colorado, Boulder

_____
Dr. Yifu Ding
Department of Mechanical Engineering, University of Colorado, Boulder

Date_____

The final copy of this thesis has been examined by the signatories, and we find that both the content and the form meet acceptable presentation standards of scholarly work in the above mentioned discipline.

Abstract

Ibrahim Saleh (Ph.D. Mechanical Engineering)

Ceramic nanotubes for applications in solar to fuel conversion, batteries, and chemical gas sensing

Thesis directed by Professor Prashant Nagpal

The design and development of a new class of material is urgently needed today to meet the current challenge of finding safe, reliable, renewable and environment-friendly energy sources. Also, developing new, safe and reliable energy storage system is needed to store the excess and unused energy produced by a renewable energy source such as solar or wind source. In addition, fabricating sensitive, portable and low-temperature gas sensor material is currently required to reduce the sensor' energy consumption, detect toxic and combustible gases and analyze human exhaled breath for medical diagnosis. Fortunately, recent breakthroughs in the fabrication of quasi one-dimensioned metal oxide and ceramic-fiber composites have opened the door to investigate new materials as a potential candidate for the applications of energy and gas sensors.

In this thesis we aim to: i) develop new, simple and cost-effective technique to synthesize doped and undoped inorganic metal oxide nanotube architecture for application in solar to fuel conversion, energy storage batteries, and chemical gas sensing, ii) synthesize and characterize a composite material made from Polymer Derived Ceramics (PDCs) and graphite fiber as high capacity, reliable and cost-effective lithium-ion battery negative electrode.

In the first part of the current work, we explain in detail a new technique of synthesis and doping transition metal oxide, TiO_2, nanotube via electrochemical anodization of titanium metal sheet in organic electrolytes containing a small amount of fluoride ion. We were able to

simultaneously incorporate several anions and cation elements into the TiO_2 nanotube crystal lattice by modifying the electrolyte composition in the anodization electrochemical cell.

Several analytical techniques such as X-Ray diffraction, scanning electron microscopy (SEM) and energy-dispersive X-ray spectroscopy (EDS) were employed to study the structure, morphology and the elemental composition of the fabricated nanotube. The undoped, N-doped, Fe-doped, N-Fe co-doped and N-C co-doped TiO_2 nanotubes were investigated as possible photoanodes candidate for photocatalytic water splitting application. The obtained results showed an improvement in; i) the nanotubes light absorption, especially the N and N-C doped samples, ii) the nanotubes charge transfer efficiency with N and N-Fe doped nanotubes as the most efficient samples, iii) the charge transport efficiency of the doped samples.

In the second part, we investigated N-doped and undoped TiO_2 nanotubes as possible reliable, safe and durable lithium-ion battery anode material. The results showed high and save lithium intercalation/deintercalation potential profile and relatively good cycling stability of both samples besides about a 25% increase in the specific capacity of N-doped nanotube. Also, we fabricate and study the electrochemical behavior of composite material made from polymer-derived ceramics and graphite fiber as possible high capacity lithium-ion battery anode material. The anode electrochemical behavior was evaluated based on the thickness of the SiCO films. Thick films exhibited the typical behavior of bulk SiCO with high first cycle loss. However, thin films, 100 nm thick, show low first cycle as well as high capacity.

In the last part, an effort has been to improve the performance of TiO_2 nanotube as a room temperature gas sensor by modifying its surface properties with anion and cation dopant materials. The investigated gases were; i) Volatile Organic Compounds (VOCs) such as acetone, methanol, ethanol, ii) water, iii) gases such as nitric oxide and carbon monoxide. The results of the study

revealed that the sensitivity and selectivity of cation or/and anion doped TiO_2 nanotubes have increased toward specific target gases such as acetone. It was also observed that undoped and Nb-doped TiO_2 nanotubes detected NO and CO at room temperature.

Acknowledgment

I would like to express my sincere gratitude to my advisor Prof. Prashant Nagpal for his supervision, guidance, encouragement of my Ph.D. study.

Also, I would like to deep thanks Prof, Rishi Raj and my thesis committee for their wisdom and guidance during my Ph.D. study at University of Colorado at Boulder.

I would especially like to thank my family, for their immense love, support, and constant encouragement.

Table of contents

List of Figures

List of tables

Chapter 1

1 Background and Introduction

1.1 Renewable energy

Today approximately 17 TW of energy is consumed globally per a year and more energy demands are expected to rise exponentially in the next few decades owing to the growth in global population, which is expected to increase up by 50% in 2050[1]. Currently, the energy supply comes mainly from non-renewable fossil fuels such as oil, natural gas and coal **Fig (1)**. Unfortunately, with the current high global energy consumption rate, the fossil fuel energy source will be inevitably depleted in about less than 100 years. Another long-term negative impact of burning and consumption the fossil fuel is the amount of the released hazardous unwanted harmful gas products, especially carbon dioxide, to the atmosphere, which eventually will lead to undesirable climate change owing to the increase in global average annual temperature that cannot be reversed **Fig (2)**. Therefore, it is important and critical to find an abundant, renewable, cost-effective, efficient, and environmentally friendly alternative energy source.

There are different forms of renewable energy such as wind, biomass, geothermal and solar, with each one having its advantages and disadvantages. However, solar energy is considerate one of the most viable alternatives to fossil fuel energy sources since it offers abundant and extremely clean energy source with zero greenhouse gas emission. In fact, the sun emits an about 3.86×10^{26} watts of energy with 1 KW/m^2 of energy on the earth surface and according to U.S. Energy Information Administration In 2017, the average annual electricity consumption for U.S. residential utility customer was about 867 kWh per month. Therefore, 200 m^2 residential utility receives about 1000 kW in just 5 hours of a sunny day.

1.2 Hydrogen as an alternative energy source and energy storage

Lately, many researchers have been investigating hydrogen as a potential pollution-free energy source and good alternative energy storage to electrochemical batteries such as lithium-ion batteries due to its;

i) abundance, Hydrogen is the most abundant element in the earth's crust.

ii) high energy density by weight and lowest energy density by volume **Fig (3)**.

iii) offers a longer lifetime and the only H_2 combustion product is water, which makes it environment friendly.

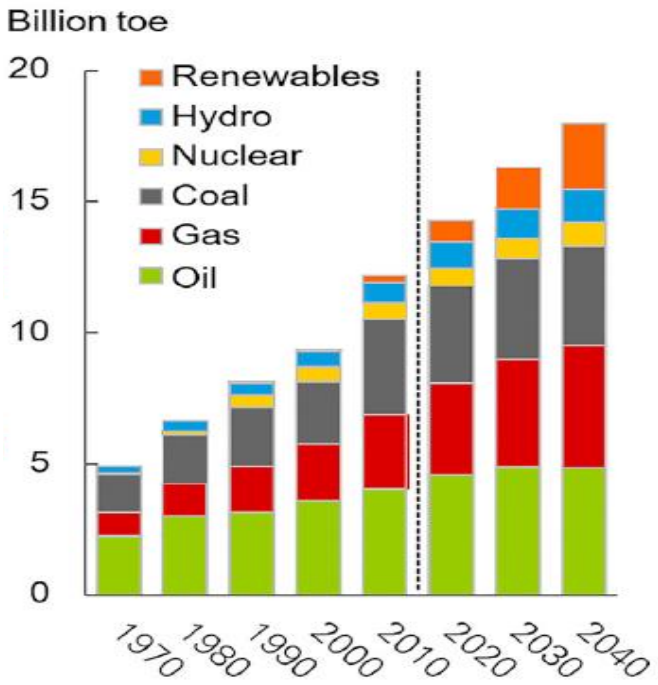

Figure 1: Natural gas and the renewables will account for 75% of global growth through 2040. "TOE" refers to "tons of oil equivalent"[2].

However, hydrogen gas is scarce and cannot be found naturally in the earth's atmosphere. Hence, it must be extracted from other components that contain hydrogen, such as water, which is the most abundant source of hydrogen. The hydrogen gas can be produced by using several methods

including fossil fuel, biomass and water electrolysis using electrical or renewable energy such as solar energy.

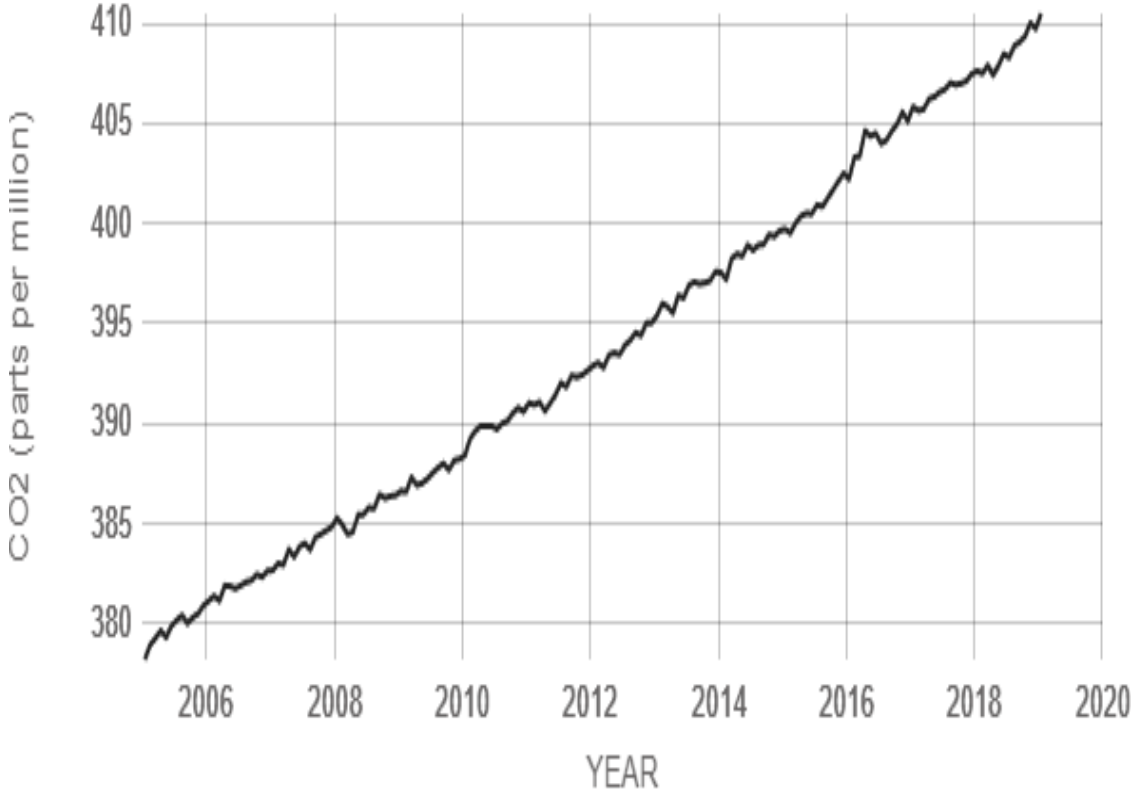

Figure 2: Atmospheric CO_2 levels measured at Mauna Loa Observatory, Hawaiiin recent in years[3].

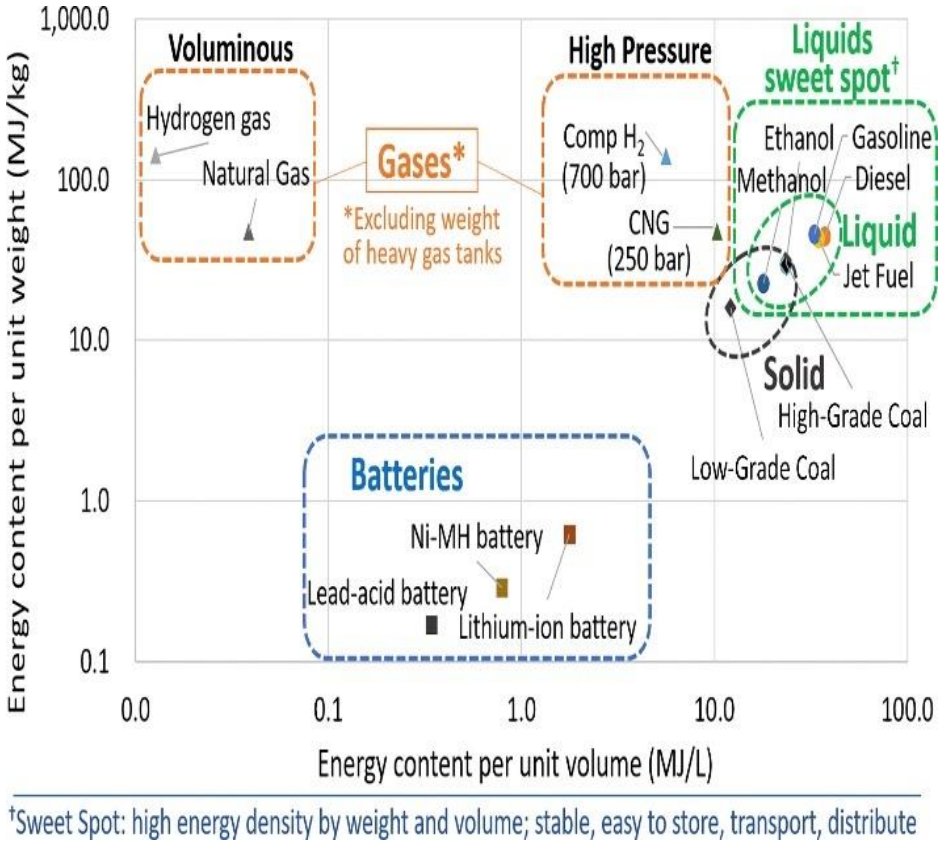

Figure 3: Energy density comparisons of several energy carriers[2].

1.3 Water splitting

Splitting water molecule into its two components elements, hydrogen, and oxygen, can be accomplished using several techniques such as the electrolysis of water, thermal decomposition, radiolysis, and photocatalytic water splitting. The latter is considerate one of the most promising techniques since it uses renewable energy sources, solar energy, instead of electricity besides allowing for large scale production of hydrogen safely and efficiently with minimal environmental impact.

1.3.1 Photocatalysis

The life on earth is powered up by the energy received from the sun via a process called photosynthesis in which the oxygen is released to the atmosphere and biomass is formed by water and carbon dioxide. The photocatalytic reaction is defined as an accelerated light-driven reaction carried out in the presence of photocatalyst material and sunlight. This reaction has a variety of applications such as water treatment[4], air cleaning[5], antibacterial[6] and solar to fuel energy conversion [7].

1.3.2 Photocatalyst material

The efficiency and kinetics of any chemical reaction that requires an excess of energy to drive the reaction, can be significantly enhanced via involvement of the external a chemical agent called chemical catalyst or photocatalyst. The photocatalyst material is used to reduce the reaction activation energy without being altered or consumed in the reaction itself, as in the case of hydrogen generation through photocatalytic water splitting using photo-active catalysts.

Photocatalyst material is usually semiconductor material that absorbs light with energy greater than its bandgap (conduction band minimum as the highest unoccupied energy band and a valance band maximum as the lowest occupied energy band).

The photocatalysis reaction is usually defined as a homogenous reaction when both the reactant and the photocatalyst exits in the same phase such as solid phase. Whereas, the heterogeneous reaction takes place when both the reactant and the photocatalyst has different phases.

In the photocatalysis reaction, the absorbed photon with appropriate energy, equal to or greater than the bandgap energy, excites the electron from the conduction band to the valance band

Fig (4). The excited photogenerated electron and hole can be utilized electrically in the application of photovoltaic cells[8], or chemically in the application of photocatalysis chemical reactions[9]. In both processes, the generated electron-hole charge carrier should be separated and transported to the reaction site quickly to avoid the quick recombination. The following equations demonstrate the photoexcitation of the electron-hole pair upon absorption of photons such that the electron reduces A species and the hole oxides D species.

$$A + e^{-} \xrightarrow{yields} A^{-} \quad (1)$$

$$D + h^{+} \xrightarrow{yields} D^{+} \quad (2)$$

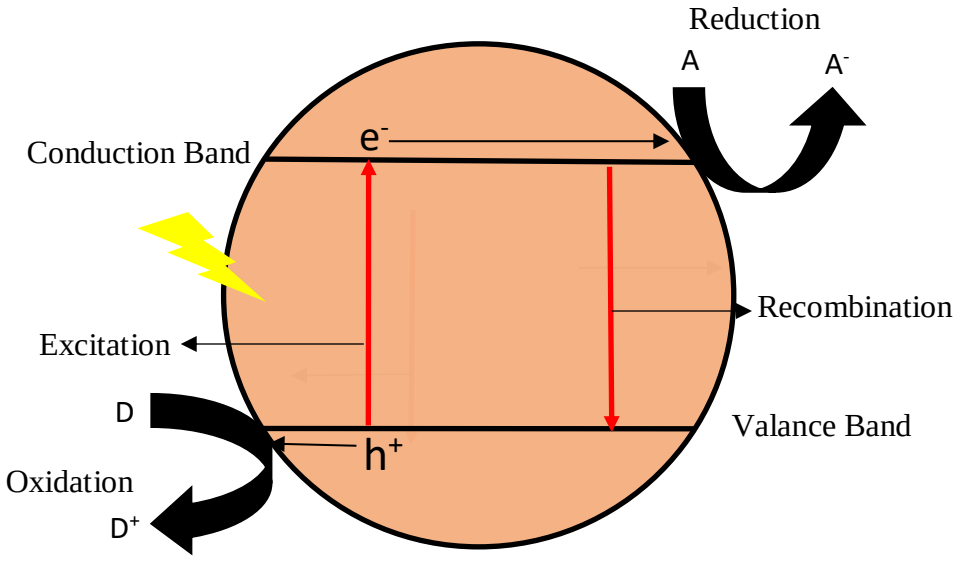

Figure 4: Schematic of the generation of electrons and holes and their reaction with donor and the acceptor species in semiconductor materials.

1.3.3 Photoelectrochemical water splitting

Fujishima and Honda introduced the photoelectrochemical water splitting for the first time in 1972[10], they irradiated n-type semiconductors materials, single crystal titanium dioxide, immersed in an aqueous electrolyte with UV light, and for the first time they were able to convert the solar energy directly to chemical energy in the form of hydrogen. This photoelectrochemical water splitting reaction can be written as:

$$2H_2O \xrightarrow{1} h^+ + 4e^- + O_2 \qquad \text{E = 1.23– 0.059V*pH} \tag{3}$$

$$4H^+ + 4e^- \xrightarrow{0} 2H_2 \qquad \text{E = -0.059V vs NHE *pH} \tag{4}$$

$$2H_2O + photos \xrightarrow{0} 2H_2 + O_2 \tag{5}$$

The water-splitting reaction is an energetically uphill reaction with the Gibbs free energy change, the minimum work required for the reaction to proceed equals to 237 kJ/mol **Fig (5)**.

According to the following equation, the minimum voltage required to split the water into hydrogen and oxygen is 1.23 V.

$$\Delta G^0 = nF\,E^0 \tag{6}$$

where *n* is the number of electrons involved in the reaction, *F* is Faraday's constant and E^0 is the standard cell voltage.

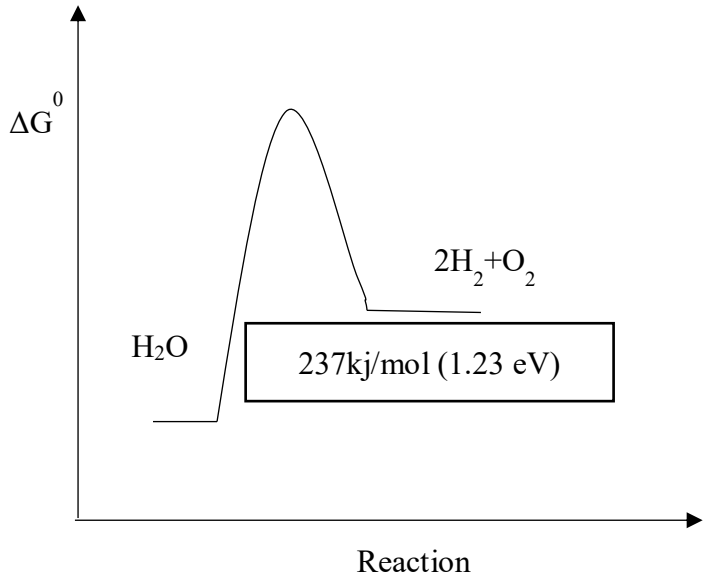

Figure 5: A schematic of the Gibbs free energy of the water splitting.

A typical photoelectrochemical (PEC) cell for water splitting is made from two electrodes, working and counter electrodes, immersed in an aqueous electrolyte **Fig (6)**. The working electrode is usually made from photo-active semiconducting material such as titanium dioxide and the counter electrode usually made from platinum metal.

As we mentioned above the incident photon with energy higher than the semiconductor bandgap will excite an electron from the valance band to the conduction band generating electron-hole pairs. These electrons and holes should be quickly transferred to the electrode/electrolyte interface and undergo redox reaction to avoid the recombination reaction. The water splitting in the electrochemical cell has two half-reactions, oxidation evolution reaction (OER) and hydrogen evolution reaction (HER). Here, the reduction potential for the hydrogen evolution is 0 V vs normal hydrogen electrode (NHE) at standard temperature 298 K, concentrations 1 mol/L and pressure 1 bar, when the electrolyte pH is 0. On the other hand, the oxidation potential of the oxygen evolution

is 1.23 V, However, more potential difference is always needed to split the water due to the overpotential losses.

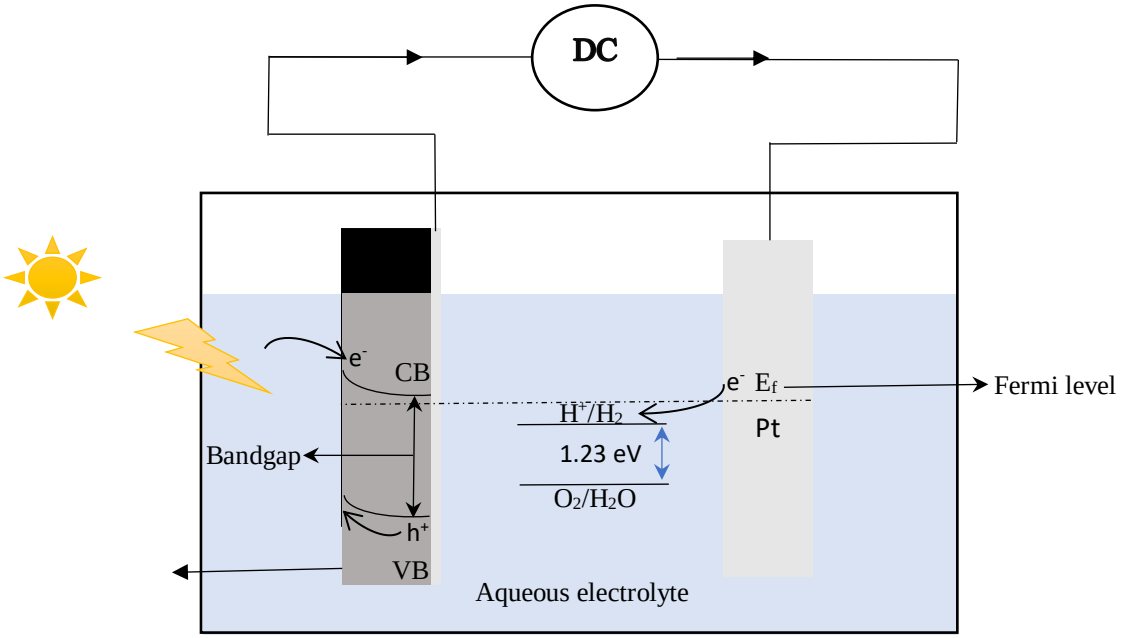

Figure 6: A schematic of Photoelectrochemical cell with n-type semiconductor as a working electrode.

The efficiency of water splitting in this PEC cell depends on the semiconductor material and its electronic structure, which is the key factor that makes photocatalysis happen. Therefore, the choice of an appropriate photo-active electrode is the most important factor in developing an efficient water splitting system. An ideal photocatalyst material should have the following set of properties;

i) The photocatalyst must absorb a broad range of the solar spectra, from near infrared to visible light.

ii) The intrinsic bandgap should be at least equal or bigger than the energy required to split the water molecules, 1.23V.

iii) The appropriate position of the band edges since water splitting depends strongly on the position of conduction and valance band edges which is related to the electron energies in respect to the redox reaction energy levels.

iv) High chemical stability in the dark and under irradiation.

v) Efficient charge transport.

vi) Low overpotentials for reduction/oxidation of water.

vii) The photocatalyst should have high crystallinity since during the transportation of the photo-generated charge carriers from the bulk to the surface, defects inside the bulk and on the surface may act as an electron-hole trap center.

1.3.4 Titanium dioxide as photocatalyst material

Titanium dioxide known as Titania, TiO_2, is a highly chemically stable, insoluble and natural abundance metal oxide [11],[12]. TiO_2 can be found or synthesized as in an amorphous or crystalline structures[13]. The crystalline structures have three main natural polymorphs, anatase, rutile, and brookite. Brookite, orthorhombic crystal structure, is usually difficult to synthesize due to its instability above 150ºC. The anatase and rutile are the most important polymorphs due to their potential utilization for many applications and uses Table 1. In general, anatase is less stable than rutile[14], but more efficient than rutile especially as photocatalyst material.

In the crystalline structure, the titanium is in octahedral coordination where titanium ion is surrounded by six oxygen ion, coordination 6. In the rutile structure, each octahedron is in contact with 10 neighbor octahedrons while in anatase structure each octahedron is in contact with eight neighbor's **Fig (7)**. Moreover, TiO_2 is a wide bandgap semiconductor whose valance band is composed of 2p orbitals of oxygen hybridized with the 3d orbitals of titanium while the conduction band is composed mainly of 3d orbitals of titanium.

The heat treatment of amorphous TiO_2 in oxygen atmosphere converts it to a crystalline anatase structure at a temperature below 400ºC. The Anatase transforms irreversibly into rutile, more thermodynamically stable phase, at a higher temperature which is about 550ºC.

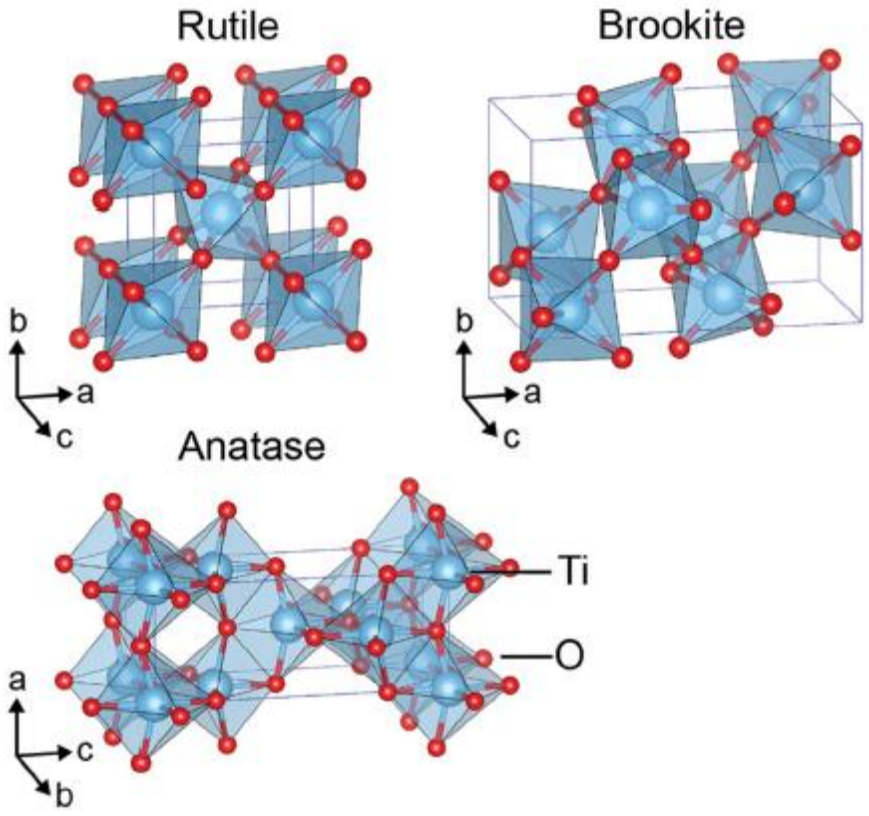

Figure 7: Crystal structures of TiO_2 rutile, brookite, and anatase polymorphs[15].

Table 1: Properties of anatase and rutile polymorphs[14].

Properties	**Anatase**	**Rutile**
Crystal structure	Tetragonal	Tetragonal
Atoms per unit cell (Z)	4	2
Density (g/ cm)	3.8	4.2
Band gap(eV)	3.2	3
Melting point (^{o}C)	Convert into Rutile	1830-1850
Volume of the elementary cell (nm^3)	136.25	62.07

1.3.4.1 TiO_2 nanotube structure

The fabrication of TiO_2 nanotube structure has significant interest for many applications such as dye-sensitized solar cells[14], water splitting[16], gas sensor[17], and lithium-ion battery[18]. In the water splitting application the nanotube structure improves the overall photocatalysis performance due to the following;

i) It shortens the diffusion paths of the charge carrier by providing a vectorial pathway for electron transport along the vertical axis of nanotubes to Ti Substrate.

ii) Increases the electron mobility.

iii) Increases the surface area for more reaction sites.

There are various methods that have been developed to fabricate the nanotube structure including hydrothermal[19], sol-gel[20] and electrochemical anodization in a fluoride-based electrolyte [21]. The latter method is considered the most favorable technique due to the following;

i) The nanotube growing process is simple and cost-effectiveness.

ii) The nanotubes are grown on Ti substrate and thus can be used directly as back-contacted metal-metal oxide.

iii) The nanotube morphology can be tuned and controlled to meet the demand of various uses and application[22],[23],[24].

The nonporous metal oxides were first introduced by Keller el, at[25] where he was able to anodized aluminum metal sheets in an acidic electrolyte, a porous oxide structure of hexagonally close-packed layer was obtained. After that, Hoyer el, at[26] was able to synthesize TiO_2 amorphous nanotubes by electrochemical deposition method into an ordered alumina template.

Assefpour-Dezfuly et. al.[27] fabricated the first porous TiO_2 by etching Ti metal substrate in alkaline peroxide and anodizing it in chromic acid. Zwilling fabricated the first self-organizing nanotube by anodizing Ti metal substrate in an electrolyte containing fluoride ion[28] . This first generation of nanotubes were not well-ordered with rough walls and short length, limited to just about 500 nm. Since then many efforts have been done to manipulate and control the morphology of electrochemical grown TiO_2 nanotubes such as the nanotube's pore diameter[29], wall thickness, inter-spacing[30], length and smoothness. The tuned nanotubes morphology can be achieved by changing the electrochemical anodization parameters such as electrolyte composition, electrolyte pH, anodization voltage and anodization time.

The length of the nanotube was increased by using the second-generation technique[31], [32]. Cai et, al[33] grew longer nanotube by using electrolytes with different range of pH to reduce the metal oxide dissolution rate. However, the aqueous-based electrolyte causes slow growth of nanotubes which can be overcome by using an organic solvent electrolyte. Paulose et. al.[34] fabricated longer and smoother nanotube by using organic electrolyte containing fluoride ions[35].

Growing TiO_2 nanotubes in a fluoride-ion free electrolyte such as hydrochloride solution was another approach to increase the nanotube's length[36]. However, longer nanotube was not obtained due to the high chemical dissolution of metal oxide by the aqueous electrolytes.

1.3.4.2 TiO_2 nanotube anodization parameters

As we already stated, different TiO_2 nanotube morphologies can be achieved by tuning the electrochemical cell's anodization parameters. The anodization electrochemical cell usually contains fluoride-based electrolyte with Ti metal as anode and Platinum as cathode **Fig (8)**. The

grown metal oxide layer could be a compact layer or self-organized nanotube depending on the anodization parameters.

The oxide layer ,nonporous structure, is usually grown in HF-aqueous electrolytes when anodization voltage is less than 10V, but when voltages increased to 10V the nanotube structure start to form with short and rough tubes [22]. However, fabrication of smooth and much longer TiO_2 nanotube was achieved in an electrochemical cell that contains an organic polar electrolytes such as formamide[34], dimethyl sulfoxide[37], ethylene glycol[21], diethylene glycol[38] and glycerol[39] . The possible reason for the nanotube's length increase is the suppression of the oxide dissolution at the top of the grown nanotubes due to much less water content in the organic electrolyte than in HF-aqueous electrolytes which lead to a decrease in the chemical dissolution[39]. In addition, the increased viscosity and lower conductivity of organic electrolytes could increase the nanotube length as well.

Another parameter that can affect the morphology of the nanotube is the aged electrolyte, reused electrolyte, where more stable and better morphology can be achieved. The aged electrolyte has better performance because of its high conductivity caused by more Ti^{+} dissolution.

The concentration of the ion fluoride can also affect the nanotube morphology. Less than 0.1wt.% fluoride ion concentration usually produces porous structure while more than 1 wt.% concentration produces a thin compact oxide layer [39].

The applied voltage controls the nanotube diameter and length with a linear relationship. Also, the anodization time increases the nanotube's length, but if the anodization time is too long the nanotubes could collapse.

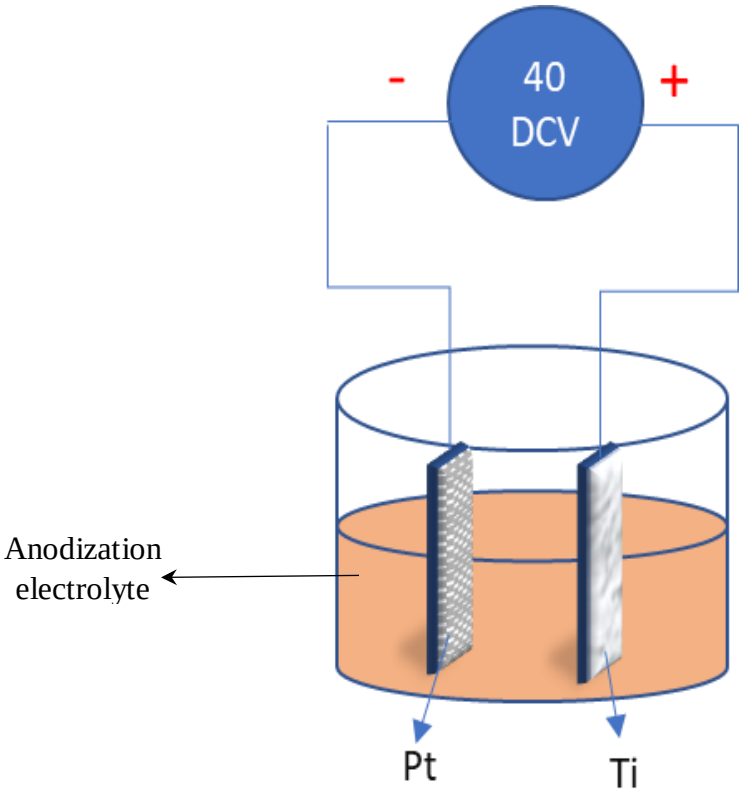

Figure 8: A schematic of the anodization electrochemical cell used for growing TiO_2 nanotube.

1.3.4.3 TiO_2 nanotube growing mechanism

A detailed model for growing and formation of the TiO_2 nanotube was proposed by Mor et. al.[40]. In this model, the nanotube formation is controlled by a competition between anodic metal oxide formation and chemical dissolution of the grown metal oxide **Fig (9)**. When we apply a proper voltage, a compact oxide layer is formed on the Ti metal substrate to create the required electrical field to drive the reaction between the Ti^{+} and water molecules (O^{2-}or OH^{-}) equation (7,8). Further oxide growth is controlled by field-aided ion transport (O^{2-} and Ti^{4+} ions) through the growing oxide. The localized dissolution of the oxide combat layer form pits **Fig (9, b)**. After that, the pits gradually turn into pores (uniformly distributed on the oxide surface).

$$Ti \rightarrow Ti^{+} + 4e^{-} \quad (7)$$

$$Ti^{+} + 2H_2O \rightarrow TiO_2 + 2H^{+} \quad (8)$$

The fluoride ion in the electrolyte accumulated at the positive electrode and under the effect of the electric field, it reacts with the TiO_2 to produce the soluble $[TiF_6]^{2-}$.

$$TiO_2 + 6F^{-} \rightarrow [T_iF_6]^{-} + 2H^{+} \quad (9)$$

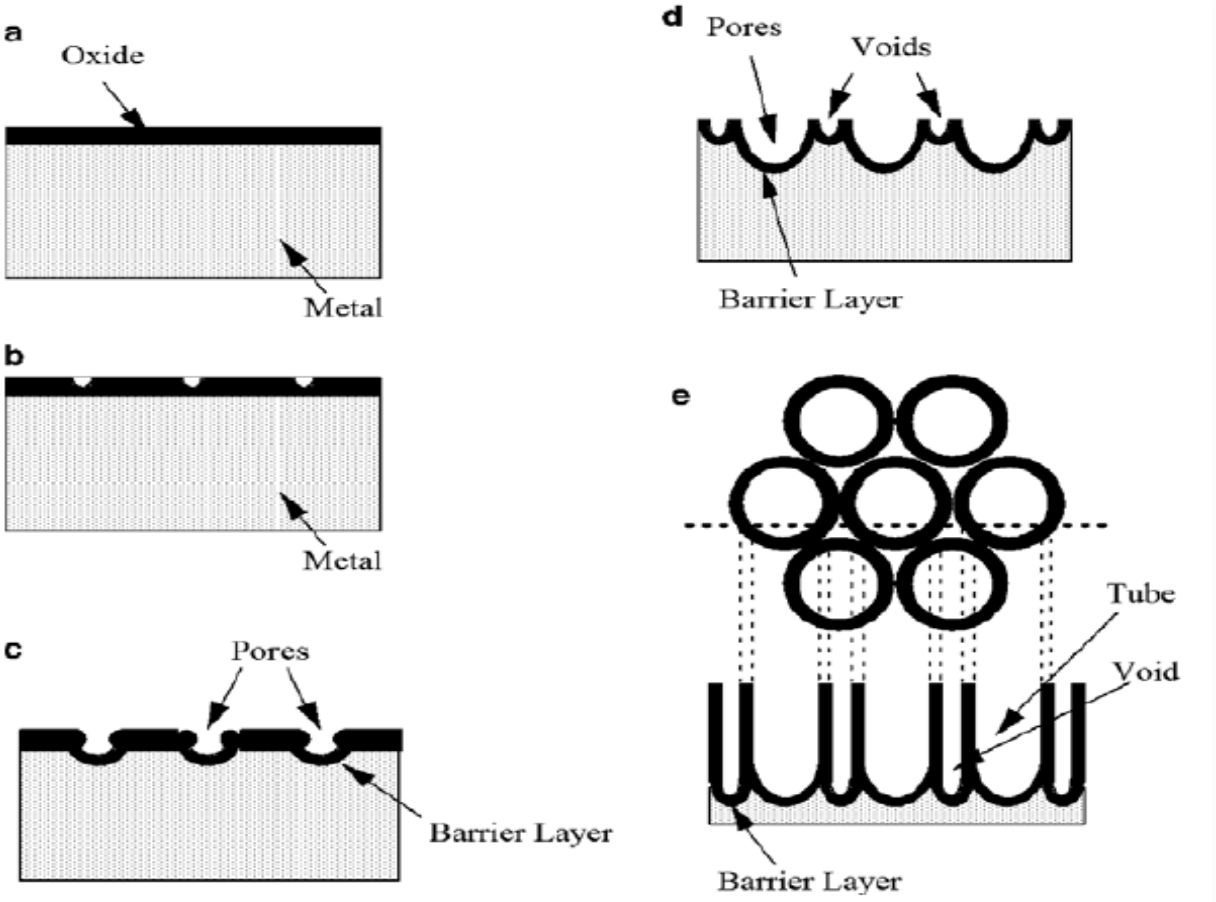

Figure 9: A schematic diagram of nanotube evolution at constant anodization voltage: (a) Oxide layer formation, (b) pit formation on the oxide layer, (c) growth of the pit into scallop-shaped pores, (d) the metallic region between the pores undergoes oxidation and field-assisted dissolution,(e) fully developed nanotubes with a corresponding top view[40].

1.4 Lithium-ion batteries (LIBs)

There is a great interest globally for developing more efficient energy storage systems for several reasons. To start with, the need for clean, abundant, sustainable and environmentally friendly energy sources such as solar, biomass, wind energy has increased, but these sources are not continuously available for release whenever and wherever is needed. Moreover, the growing interest in electrical-powered automotive has lately increased to replace the current gasoline-powered in order to decrease global warming by limiting CO_2 emissions. Also, electrochemical storage devices such as lithium-ion batteries are being used daily across a wide range of portable devices such as cellular phones, laptops, camcorders.

The electrochemical batteries represent an excellent class of energy storage technology owing to their high efficiency, flexibility power and energy characteristics, modularity, and scalability.

There are two major types of batteries: primary batteries, and secondary batteries. The primary battery is non-rechargeable, but the secondary is rechargeable (reversible redox reaction). Currently, the available rechargeable batteries are classified into alkali batteries, capacitors, and lithium-ion batteries. Among them, lithium-ion batteries are currently considerate the most favorable energy storage device owing to their high energy density per weight (lithium is the lightest metal, less toxic, and the most electropositive element with about -3.04 V vs standard hydrogen) Table 2 and **Fig (10)**.

Table 2: Advantages and limitations of the lithium-ion battery.

Advantage	Disadvantage
High energy density	High cost
Good cycling life	No stability at high temperature
Good coulombic efficiency	No stability at overcharging
Low self-discharge rate	High internal resistance
No memory effect	Safety

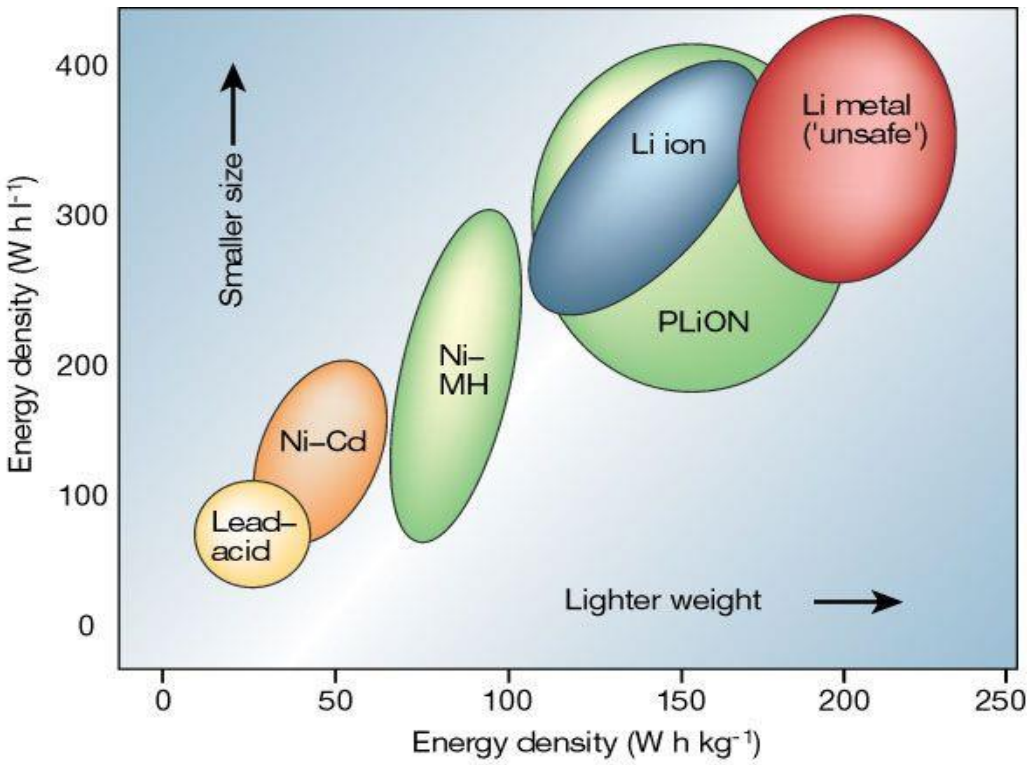

Figure 10: Comparison of the different rechargeable battery in terms of volumetric and gravimetric energy density[41].

1.4.1 Electrochemical principles of LIBs

The lithium-ion battery consists of three major components, two electrodes called a cathode and anode immersed in lithium-ion conducting organic electrolyte, and a porous separator placed between the two electrodes to prevent the electrodes from touching each other, which can lead to short circuit. Ideally, both anode and cathode should have a layered structure in which lithium and lithium-ion can intercalate and deintercalation without interrupting the host material. The cathode is usually made from layered lithium metal oxide such as lithium cobalt oxides, and the anode is made from carbon material such as graphite. The electrode material is selected such as the chemical potential of the lithium is higher in one electrode than the other. The electrolyte must be pure and free of water and has the special property of being able to conduct Li-ion but not Li atom. The architecture of the LIBs can be imagined as a sandwich-like structure with the electrolyte in the middle, and with an electrical connection that transfers the current of from the electrodes to the external electrical circuit.

The electrochemical performance of the battery is characterized by the following parameters:

(i) The energy density which is the amount of lithium that can be stored inside the active materials (it can be obtained experimentally by calculating the area under Voltage-specific capacity curve).

(ii) The power density which is the Watts per unit weight of the active materials (it can be obtained experimentally by multiplying the voltage and the current).

(iii) The other parameters are related to the gradual loss of performance with cycling, life, and safety.

Also, the specific capacity is defined by how much of Li the electrode material can hold per unit mass or volume. It can be defined as follows:

$$SC = \frac{F \times n}{Mwx\ 3.6}\ , \tag{10}$$

Where F is the Faraday constant (96,500 C/mol), n is the number of charge carrier, Mw is the molecular weight of the electrode. The maximum specific capacity that can be obtained from the battery depends on the weight and type of the electrode's material. However, the experimental capacity is always less than the theoretical capacity due to the side reaction between the electrodes and the electrolyte.

The Coulombic efficiency is defined by the ratio between the amount of inserted lithium capacity over the extracted lithium capacity. It is a good indication of the electrochemical reversibility and the possible side reaction between the electrodes and the electrolyte.

$$CE = \frac{\text{Discharge capacity}}{\text{charge capacity}}\ . \tag{11}$$

In LIBs, the difference in the chemical potential of the lithium in the two electrodes is converted into electrical energy by redox reactions at the anode and cathode which can be represented by the following equation:

$$L_i xM \overset{\text{reversible}}{\longleftrightarrow} xL_i^+ + xe^- \tag{12}$$

Where M is the active material and *x* the lithium mole fraction.

During battery charge, electrons are initially extracted from the cathode and the Li-ions are inserted into the anode material, through water-free electrolyte solution, by applying external bias **Fig (11)**. During battery discharge, the moving directions of both Li-ions and electrons are just reversed.

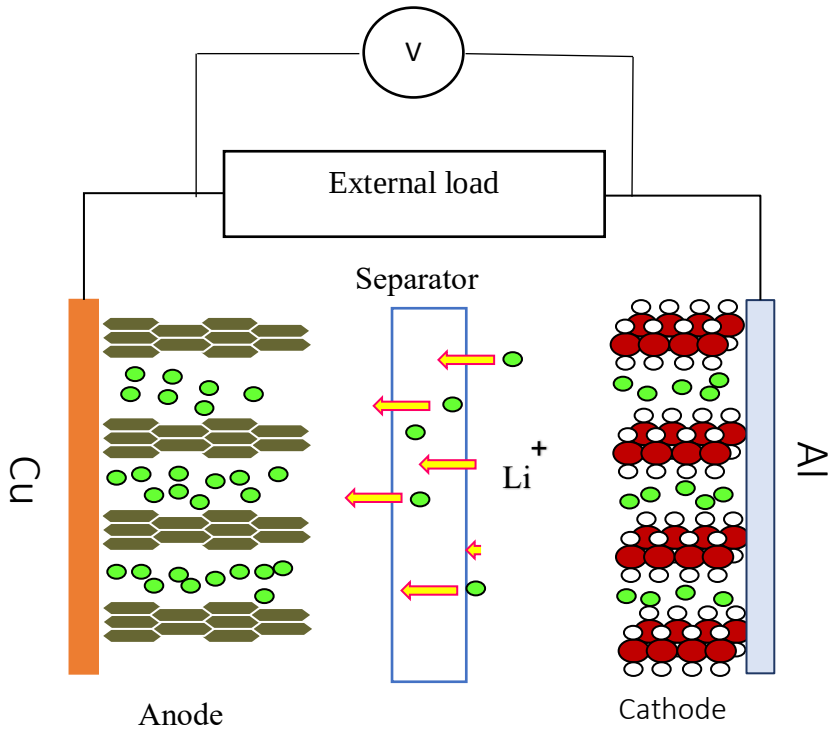

Figure 11: Schematic of the charging process in a lithium-ion.

1.4.2 Material for LIBs

1.4.2.1 Anode materials

The anode in the lithium-ion battery can significantly affect the battery overall electrochemical behavior depending on its chemical, physical and energy storage properties **Fig (12)**. Also, the

selection of proper anode material depends on its durability, on whether it is electronically conducting and how fast Li atoms can diffuse through the material.

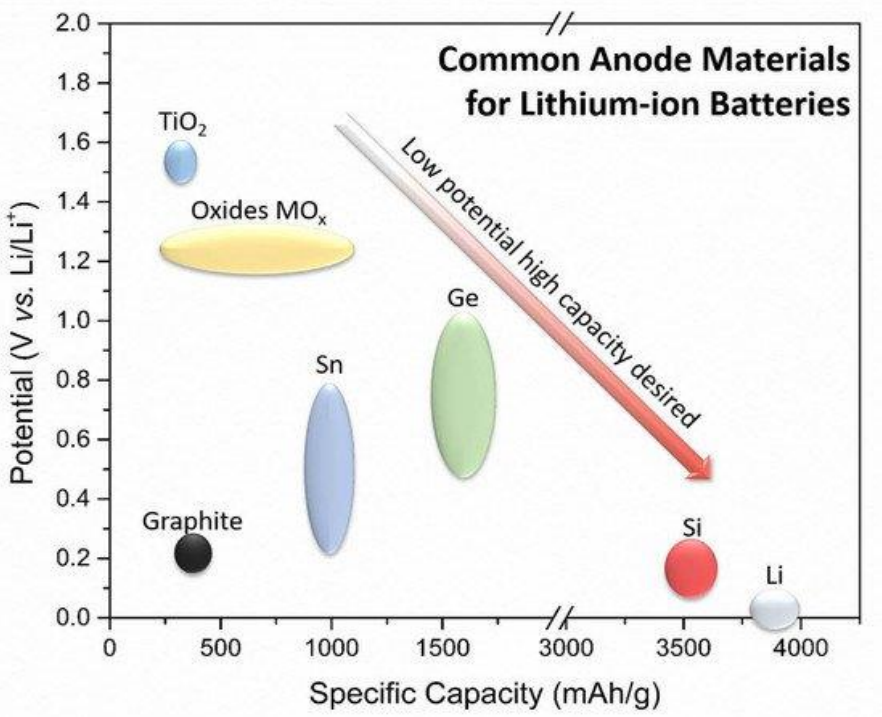

Figure 12: Working potential vs specific capacity of various active anode material[42].

Furthermore, the appropriate structure of anode material significantly improves the overall battery performance. For example, the nanostructure morphology can improve the insertion and extraction of the Li-ion since the diffusion rate depends on the diffusion coefficient and diffusion length in the active material, as follows:

$$\tau = L_i^{+\,2}/D_{L_i} \tag{13}$$

Here, D_{Li} refers to the diffusion coefficient of the active material, L_i^+ is the diffusion length of the Li-ion.

1.4.2.1.1 Carbon anode material

In the past three decades, the most frequently used anode material in LIBs is made from carbonaceous material such as graphite replacing the unsafe and high capacity lithium metal anode. The graphite has low operation potential, good cyclability, inexpensive and considerably abundant. Also, it has a well-defined layered structure of graphite consists of parallel planar layers with honeycomb-like geometry. The bond between the graphite layers is weak leading to change in the interlayer distance during charge and discharge cycles **Fig (13)**. One lithium species per six carbon can be inserted into space between the parallel planar layers leading to the specific theoretical capacity of 372 mAh/g, as shown in the following equation:

;

$$L_i + 6\mathrm{C} + \mathrm{e}^- \rightarrow L_i\mathrm{C}_6\,, \tag{14}$$

Here, *C* refers to carbon and *Li* to the Lithium element.

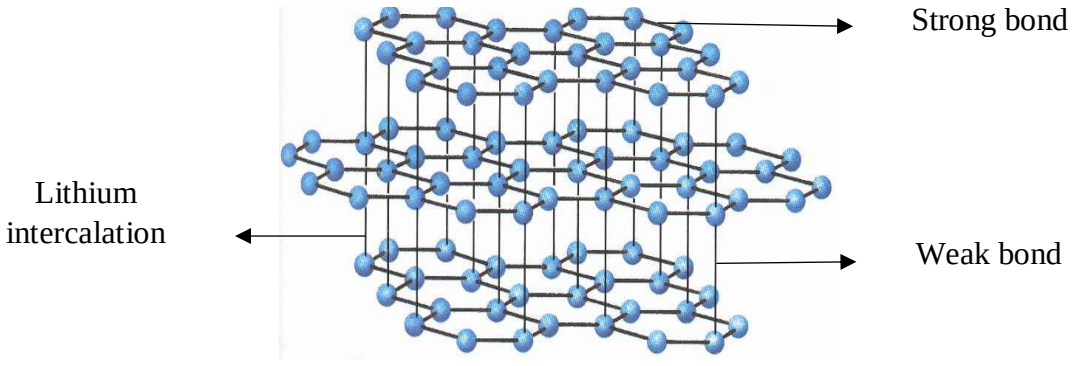

Figure 13: A schematic of the graphite structure.

1.4.2.1.2 Lithium alloys anode material

Materials such as Li- Silicon[43] and Li–Sn [44] have been widely studied as an alternative LIBs anode material in an attempt to replace the traditional anode material (graphite anode). The graphite anode suffers from low capacity and formation of lithium dendrite at the anode surface causing a short circuit and battery failure. Alloying is a good approach to increase intercalation and deintercalation voltage plateau in order to reduce the dendrite formation risk and increase the anode capacity as well. However, Lithium alloys suffer from large volume expansion during Lithium intercalation and deintercalation discharge, leading to poor cycling stability and eventually to battery failure. **Table 3** summarizes the characteristics of different Lithium alloys as anode material.

Table 3: Characteristics of anode alloys of Lithium with various elements.

element	Lithiated phases x	x in Li_xM	Expansion (%)	voltage (V)	Capacity
Si	$Li_{15}Si_4$	3.75	280	0.4	3579
Sn	Li_ySn	0.4	22	0.76	90
Mg	Li_xMg	0−1.95	0-12.5	0.0325	0-2150
Al	LiAl	1	90	0.380	993
Zn	Li_2Zn_5	0.4	39	0.49	164

.

During battery charge, Li ions are electrically driven by external bias into the active material to make an alloy anode. After that, the formed alloy decomposes due to the difference in the lithium chemical potential in the anode and cathode material, leading to release of electrons from the anode into the external load according to the following equation;

$$XL_i^+ + xM + Xe^- \overset{reversible}{\longleftrightarrow} M_xL_{iX} \quad (15)$$

Where M is the active material and X is the mole fraction ranging from 0 to 1.

1.4.2.1.3 Metal oxide anode material

Metal oxides are promising alternative LIBs anode material due to their excellent stability, cyclability, environmentally benign nature, and availability. Moreover, their high lithium intercalation voltage is relatively high, in comparison to a carbon-based electrode. This high intercalation potential can prevent the problematic dendritic lithium from the formation on the anode surface. However, the metal oxide anodes suffer from poor rate capability, low electrical conductivity and fast capacity fading caused by large volume expansion during battery charge and discharge cycling.

There are several approaches that can be adapted to overcome the above-mentioned drawbacks of the metal oxides anode, they include;

i) Fabricating nanostructure anode to shorten Li-ion diffusion and lower the stress caused by lithium insertion into the electrodes.
ii) Doping the metal oxide with anion and/or cation to increase the capacity and electrical conductivity.
iii) Fabricating a composite anode made from the metal oxide and other material such as carbon-based material to increase the capacity and enhance the electrical properties.

The mechanisms of lithium intercalating in metal oxide anodes can be classified into two main reactions:

i) Conversion reaction

$$M_xO_y + 2yL_i^+ + 2ye^- \overset{reversible}{\longleftrightarrow} 2L_{i2}O + xM \quad (16)$$

Where *y* is the Li mole fraction.

ii) intercalation/deintercalation reaction

$$M_xO_y + nL_i^+ + ne^- \overset{reversible}{\longleftrightarrow} 2L_{i2}O + L_iM_xO_y \quad (17)$$

Where n is the Li mole fraction.

Metal oxides such as MoO_2, Co_3O_4, and α-Fe_2O_3 intercalate the lithium according to conversion reaction, whereas few metal-oxides such as TiO_2 follow intercalation/deintercalation reaction.

1.4.2.2 Cathode material

The most commonly used cathodic material in LIBs include lithium iron phosphate $LiFeO_2$, Spinel-based lithium-ion, $LiMn_2O_4$ (LMO) and Cobalt-based such as $LiCoO_2$ **Table 4**. The cathode materials should have the following properties to be considered an excellent cathode material;

1- High capacity.

2- High electronic conductivity which is intrinsic material properties.

3- High lithium conductivity which is related to the diffusion of the L_i^+.

Table 4: Most common LIBs cathodic material properties.

Cathode material	Electronic conductivity ($S.cm^{-1}$)	Theoretical capacity mAh/g	Comment
$LiMn_2O_4$	10^{-5}	148	Low conductivity, high rate, and low cost
$LiCoO_2$	10^{-3}	274	High cost, unstable
$LiFeO_2$	10^{-9}	170	High energy density, low electronic conductivity low cost
$LiNiO_2$	10^{-2}		Unstable, high energy density, low cost

1.4.3 TiO_2 nanotube as anode material of LIBs

Owing to its high lithium intercalation voltage (1.5-1.8 V vs Li/Li^+) and low volume expansion change during charge/discharge cycles, TiO_2 metal oxide is considered one of the most alternative promising substitutes as anode material in LIBs for the applications where the safety is the primary concern and goal.

TiO_2 has three different main polymorphs rutile, anatase (both have tetragonal crystal structure) and brookite (orthorhombic crystal structure). Rutile has a relatively low capacity of around 168 mAh/g and anatase has relatively high (335 mAh/g) while Brookite has unstable crystalline phase and thus is not considered a good choice as anode active material.

The reversible lithium-ion upon charge and discharge into TiO_2 is as following:

$$xL_i^+ + \mathrm{T_i}O_2 + xe^- \overset{reversible}{\longleftrightarrow} L_x\mathrm{T_i}O_2 \quad (0 \le x \le 1) \tag{18}$$

where *x* is the mole fraction ranging from 0 to 1 depending on crystallinity, morphology and the specific surface area. However, the experimental capacity is always less than the theoretical specific capacity due to poor Li-ion diffusion in the TiO_2.

1.4.4 Polymer derived ceramics as anode material of LIBs

Polymer Derived Ceramics (PDCs) are a new class of materials, which as the name suggests, are derived by thermal decomposition, polymerization, of polymeric precursors such as organosilicon in a specific controlled inert atmosphere[45]–[48].

The polymeric precursors are usually made from chain molecules with silicon–group inorganic as the backbone and the organic as functional groups. The different classes of organosilicon polymeric precursors are classified based on polymer backbone Si-X; Organocarbosilanes (Si-C bonds), Organosilazanes (Si-N bonds) and Organosiloxanes (Si-O bonds) **Fig (14)**. The functional radical group bonded into the silicon can be polymerized and pyrolyzed to remove the organic groups to form the required ceramic.

The polymer derived ceramics is generally classified into two main families depending on their chemical composition, silicon oxycarbide (silicon-oxygen-carbon) abbreviated as SiCO and silicon carbonitride (silicon, nitrogen, and carbon) abbreviated as SiCN. The synthesis of carbon rich SiCO or SiCN ceramics can only be possible via the thermal decomposition route due to the

limited solubility of carbon in silica or silicon nitride. The molar composition of these PDCs consists of one-third Si, one-third C, one-third N, and one-third O as shown in **Fig (15)**.

.

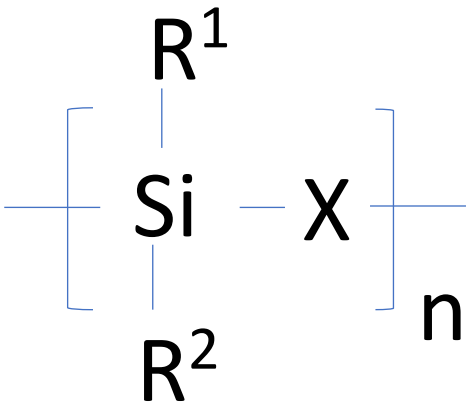

Figure 14: General oversimplified representation of the molecular structure of preceramic organosilicon compounds[49].

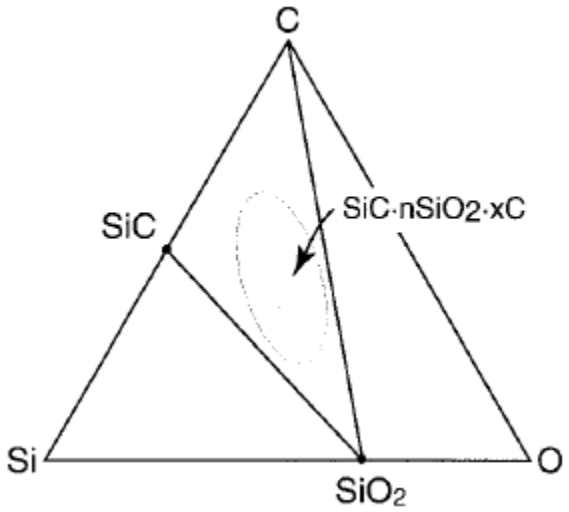

Figure 15: Composition regimes of siliconoxycarbide SiCO [50].

Among different routes to synthesis the PDCs such as casting[51] and photo-polymerization[52] route, the polymer pyrolysis route, decomposition of polymeric precursors, has the advantage of

being simple and cost-effective. **Table 5** summarizes the difference between the polymer pyrolysis route and traditional powder route technology.

Table 5: Difference between ceramic produced via polymer pyrolysis vs traditional powder technology.

Properties	Polymeric precursors polymerization	Traditional powder technology
Purity	Pure ceramic	Less pure
Processing temperature	Significant reduction	High temperature
Machining	Flexible shapes (three-dimension)	Hard to shape
Cost	Inexpensive	Expensive

The PDCs has excellent properties, such as thermal and chemical stability[53], creep resistance[53], [54], corrosion resistance[55], tunable porosity structure with high specific surface area and Li-storage capability[56]. These properties can be tuned and modified by changing the molecular structure of the polymer precursor and the synthesis route. The PDCs unique properties can be attributed to the following;

i) The rich carbon contents.

ii) The special nanodomain, 1-3 nm in size in amorphous PDCs, which consist of graphene-like carbon network, SiO_2 and SiC crystallites **Fig (16).**

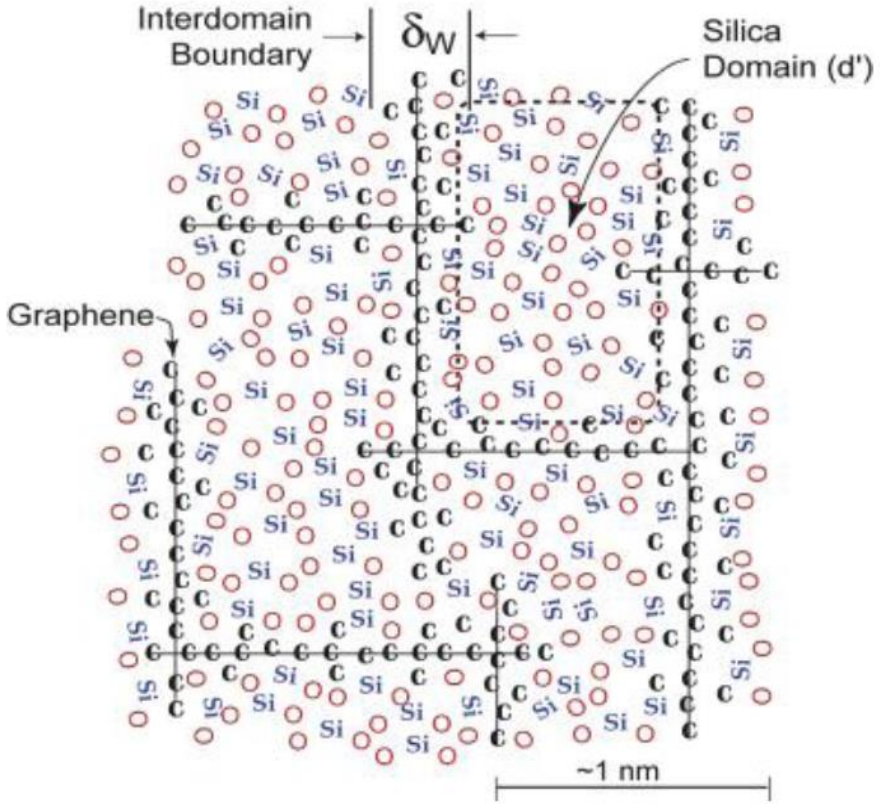

Figure 16: Nanostructure model for the of SiCO [57].

As we mentioned, silicon oxycarbide, SiCO, and silicon carbonitride are the most studied and investigated PDCs ceramics due to their bond nature between the silicon and the carbon in the precursor, organosilicon polymer, that prevent the carbon from reacting and driven out as gas during the thermal treatment[49]. However, during the thermal pyrolyzing of the organosilicon polymer in a controlled inert atmosphere, the hydrogen is driven out as a gas, leaving a ceramic glass. The gradual nature of the chemical decomposition of the polymer and the strong covalent bonds formed as the gases leave the material, strongly limits atomic diffusion within the material. This means that the resultant carbon network and SiOx domains, thermodynamically favored, are

separated only at the nanoscale. The result of this nanoscale microstructure is that SiCO can behave very differently compared to SiOx glass, despite being composed predominantly of SiOx domains.

1.4.4.1 Polymer derived ceramic fabrication

In the polymer pyrolysis route, the liquid precursor is usually crosslinked at temperature range between 150ºC and 400ºC to form an infusible hard epoxy-like solid, and then the epoxy solid is pyrolyzed in inert atmosphere such as argon at temperature range from 800ºC to 1500ºC to lose hydrogen and self-assemble into a pseudo-amorphous ceramic phase consisting of Si-N-O domains separated by "free carbon" in the form of disordered graphene sheets **Fig (17)**.

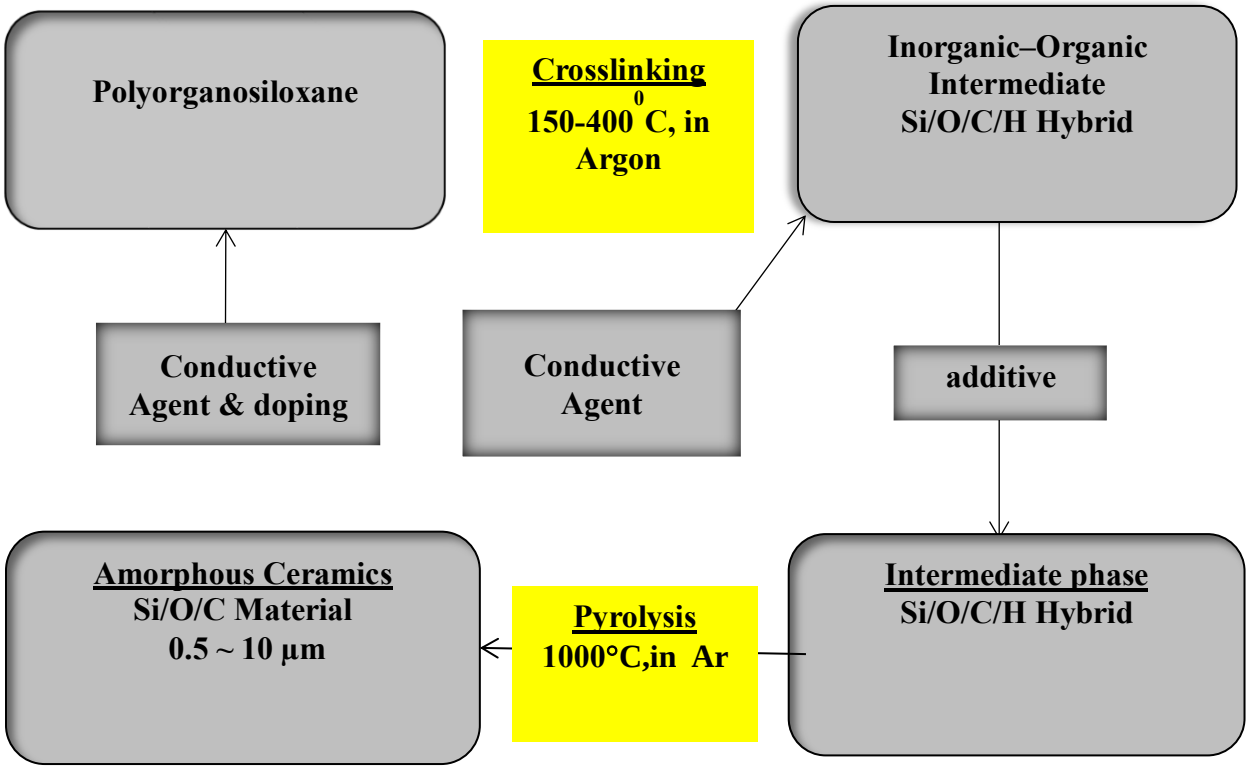

Figure 17: Synthesis procedures of polymer derived ceramics by thermal decomposition route.

1.4.4.2 Polymer derived ceramic characterization

1.4.4.2.1 Thermogravimetric

Thermogravimetric analysis is a good technique to measure the amount of PDCs obtained from the thermal decomposition of the preceramic precursor, polymer into the ceramic conversion. TGA measurement was done by using (STA 409, NETZSCH, Germany) under an inert atmosphere with 10ºC /min ramp to 1025ºC. The mass loss starts at about 450ºC and stops at about 825ºC **Fig (18)**.

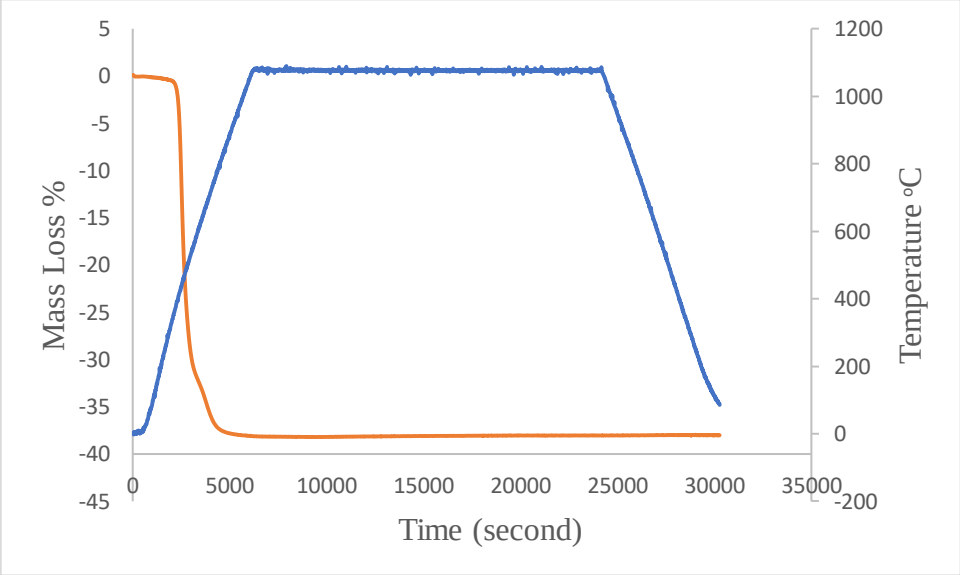

Figure 18: Thermogravimetric analysis (TGA) of polymer derived ceramics.

1.4.4.2.2 X-ray Diffraction (XRD)

X-ray Diffraction (XRD) technique was used to study the crystallinity of the fabricated PDCs samples treated up to 1200ºC. There was no evidence of crystal growth (amorphous).

1.4.4.2.3 BET analysis

The specific surface area of crosslinked-epoxy and PDCs was measured by using Micromeritics ASAP 210, with absorption nitrogen gas and degassing at 150^{o}C for 8 hours. The specific surface area for crosslinked-epoxy and PDCs was measured to be 40 ± 5 and 3±1 m^2/g respectively.

1.4.4.2.4 SEM

The surface morphology of all samples was studied by using Field Emission Scanning Electron Microscope. **Fig (20, a)** shows the surface graphite fiber coated with PDCs and **Fig (19, b)** displays the Surface morphology of PDCs powder.

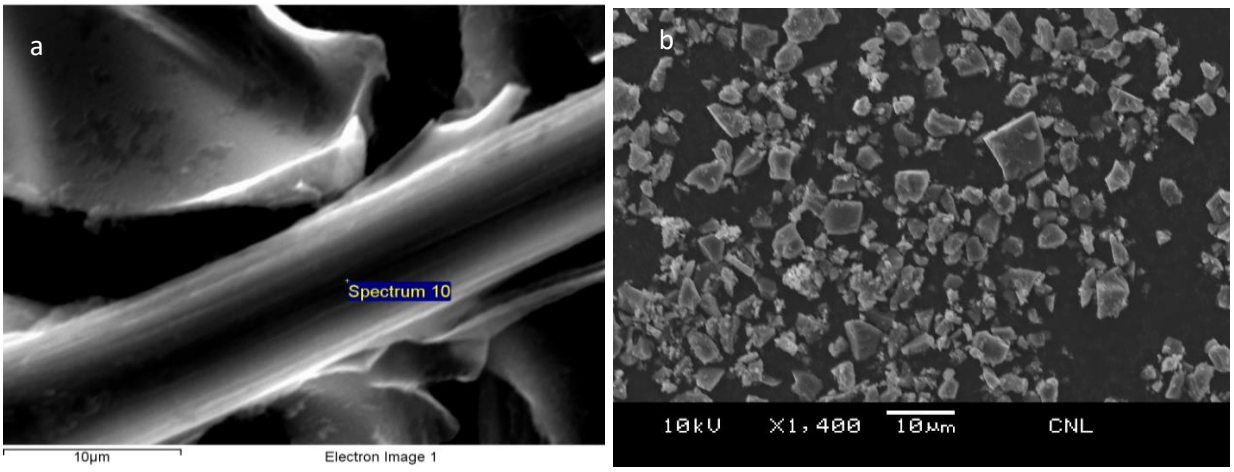

Figure 19: Surface morphology of PDCs powder (a) graphite fiber coated with SiCO (b).

1.4.4.2.5 Elemental analysis

The elemental analysis of SiCO was done by measuring the content of carbon and nitrogen and silicon. The carbon was measured by combustion (LECO Corp., Model C-200) with accelerants as iron chip and Lecocel II HP which nitrogen and oxygen content were analyzed by fusion (LECO Corp., Model TC-600). Cast iron with 3.36 % carbon was used as a standard in carbon analysis and tungsten oxide and aluminum nitride were selected as standards in oxygen and nitrogen analysis. The results of SiCO PDCs heat-treated at 1000^{o}C is shown in **Fig (20)**.

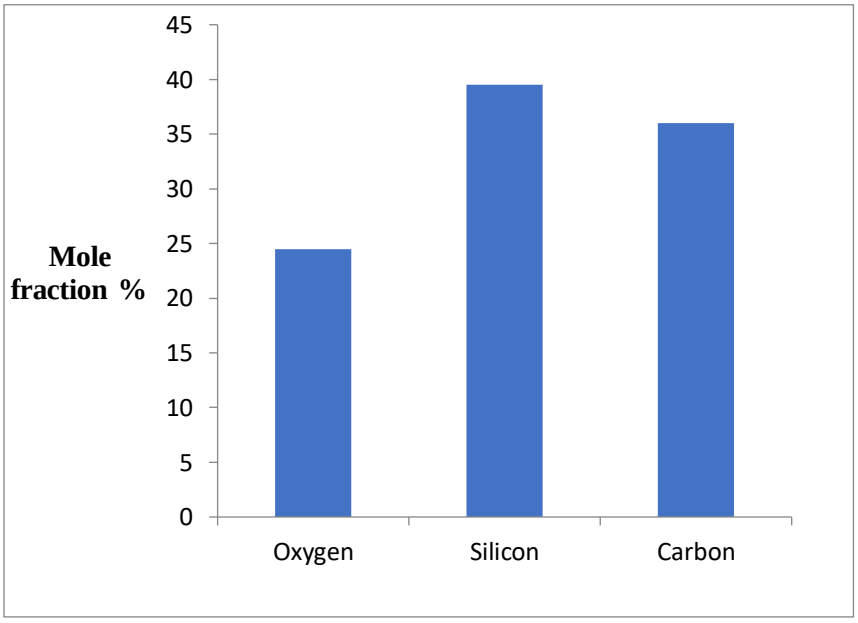

Figure 20: Oxygen, silicon, and Carbon mole fraction in SiCO PDCs heat treaded at 1000ºC.

1.4.4.2.6 Raman spectroscopy

Raman spectroscopy was collected by using micro-Raman spectrometer (Horiba Jobin Yvon, Japan) with a 532nm laser beam in an ambient atmosphere to gain insight into the carbon structure of the obtained PDCs with its sensitive Raman carbon element. **Fig (21)** shows the Raman spectra in the range from 450 to 1900 cm^{-1} for uncoated graphite fiber with G peak at 1589 and D peak at 1358.

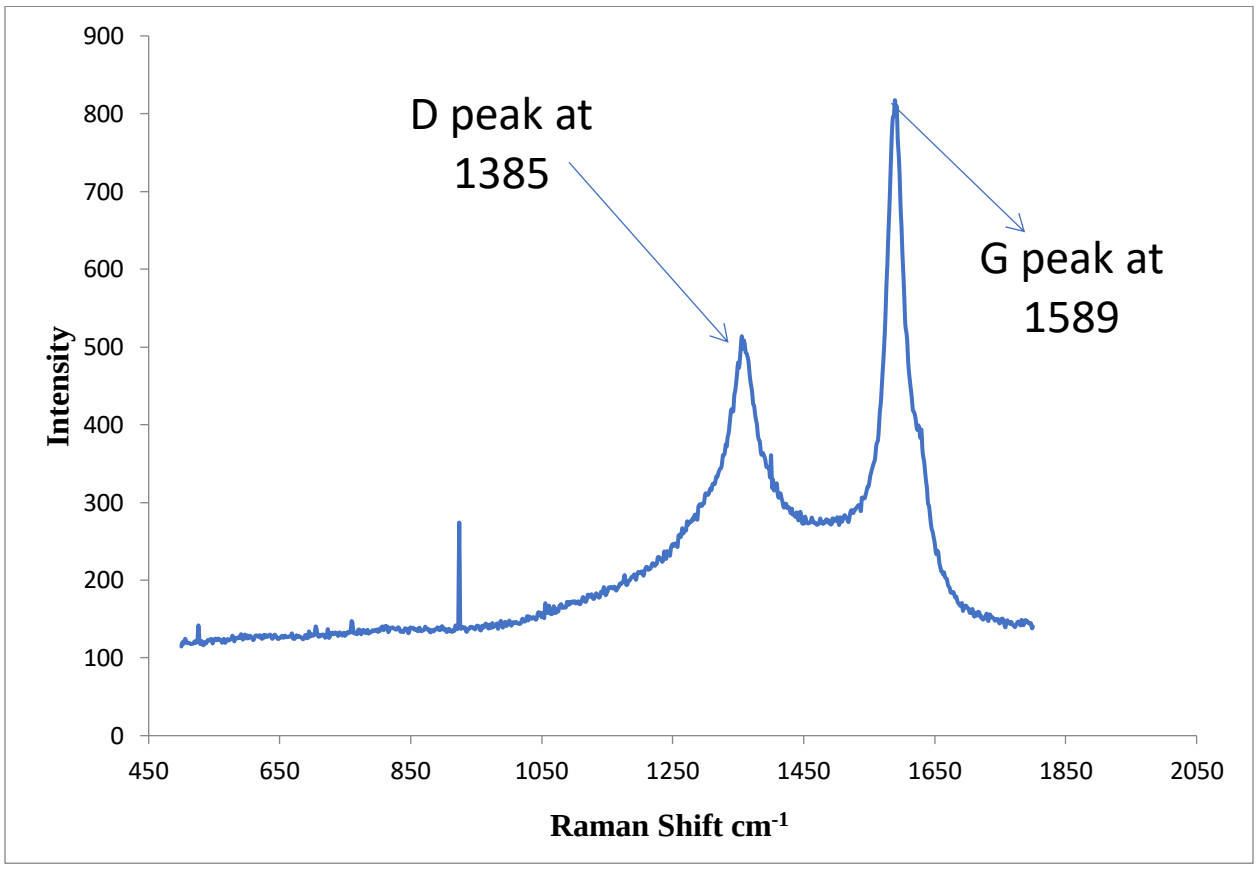

Figure 21: Raman spectra of uncoated graphite fiber.

1.5 Metal oxide as chemical and gas sensor

Developing inexpensive, portable, room temperature and low power-consuming gas sensors have attracted the attention of many researchers due to their wide range of applications such as monitoring toxic gases, detection flammable gases and in situ analysis of exhaled breath in the form of portable devices[58], [59][60][60]–[62].

There are two main techniques to detect gases, direct and indirect detection; i) the direct technique directly measures the physical properties of the target gas, ii) the indirect technique mainly depends on using a chemical reaction or indicator to measure the target gas concentration of, a summary of these detection techniques is listed in Table 6[63].

Metal oxide semiconductors are particularly interesting for applications of gas sensors due to the change in their electrical resistivity upon exposure the gas molecules. The interaction of their surface with gas via the adsorption/desorption process has been first introduced nearly 60 years ago[64]. A few years later it was observed that the electrical properties of the heated metal oxide ,zinc oxide film, were sensitive to the presence of a small concentration of reactive gases in the ambient air[65]. After that, another study observed that the electrical resistivity of tin oxide and zinc oxide changes with the gas composition at the ambient atmosphere[66]. Since then, the metal oxide semiconductor gas sensors have been extensively investigated as a promising alternative gas sensor to other sensing technology such as optical spectroscopy and gas chromatography spectroscopy[66]. These metal oxide sensors are relatively less expensive, portable, robust, easy to use, sensitive to low gas concentration and they consume much less power.

Table 6: Advantages and disadvantages of different gas detection technique[63].

Method	Advantage	Disadvantage
Direct technique		
Optical spectroscopy: measurement of optical absorption, emission or scattering	Offers a direct and rapid, and often highly selective means, of measuring gas concentration with good sensitivity.	The gas must have a significant and distinct absorption, emission or scattering in a convenient region of the optical spectrum.
Mass spectrometry	Very accurate and highly selective means of detecting concentrations of gas, including isotope abundance, etc.	Slowly acting. Very bulky. Very expensive. Not easy to use online, as gas sampling necessary
Gas chromatography	Very accurate and highly selective means of detecting concentration.	Very expensive Not easy to use online, as gas sampling necessary.
Indirect technique		
Interaction with a chemical indicator	Can be highly specific, if a suitable indicator. Can measure total exposure over time (dosimetry), if a non-reversible reaction is used. Can allow operation at a convenient wavelength, when gas has no convenient absorption in that spectral range.	Poisoning can occur and is easily fouled. Sensitive to groups of chemicals, Eg. acid gases, rather than to a specific gas. May exhibit non-reversible behavior, which, in many cases, may be undesirable. May need water vapor present, to act as a catalyst, if "dry" reaction is too slow.
Sensors involving interaction with the surface of a semiconductor, or ceramic layer, e.g. (CHEMFETS and other electrochemical sensors)	Low cost. Can measure total exposure over time, if a nonreversible reaction is used.	Poisoning can occur. May exhibit non-reversible behavior, which may be undesirable. May consume analyte.
Catalytically induced combustion and measurement of the heat change (Pellistor gas sensors)	Low cost and practical means of detecting the presence of flammable gases.	Poisoning can occur. Sensitive to groups of gases, rather than specific gas in a group. If other flammable gas is present, may give a reading which is not predictably related to the lower explosive limit (LEL).

Also, metal oxide semiconductor with high surface to volume ratio, are being increasingly used for gas sensing due to their size-dependent properties and ability to adsorb as much of the target gas as possible on their surface.

The performance of metal oxide gas sensors can be characterized by the following:

i) The sensitivity, which is defined as the effect of the target gas concentration on the electrical properties of the metal oxide and it is usually represented by the following equation (in the presence of the reducing target gas);

$$S = (R_a/R_g) = \Delta n/n, \tag{19}$$

Where *Ra*, *Rg*, Δn, and n are the resistance of the sensor in the air, the resistance in the presence of the reducing target gas, changes in carrier concentration and the initial carrier concentration respectively. In the presence of the oxidizing target gas we use the following equation;

$$S = (R_g/R_a) = \Delta n/n. \tag{20}$$

The sensitive can be as well determined experimentally from the slope of the calibration graph (electrical signal vs gas concentration). The greater the slope of the calibration line, the greater the sensor sensitivity **Fig (22)**.

i) The selectivity, which is the ability of the metal oxide sensor to recognize certain target gas inside a mixture of gases.

ii) The response time, defined as the amount of time it takes for the sensor to measure 90% of the maximum gas level.

iii) The recovery time which is the time required for the sensor to return to its initial signal

iv) Operation temperature is the temperature where the maximum sensitivity is obtained

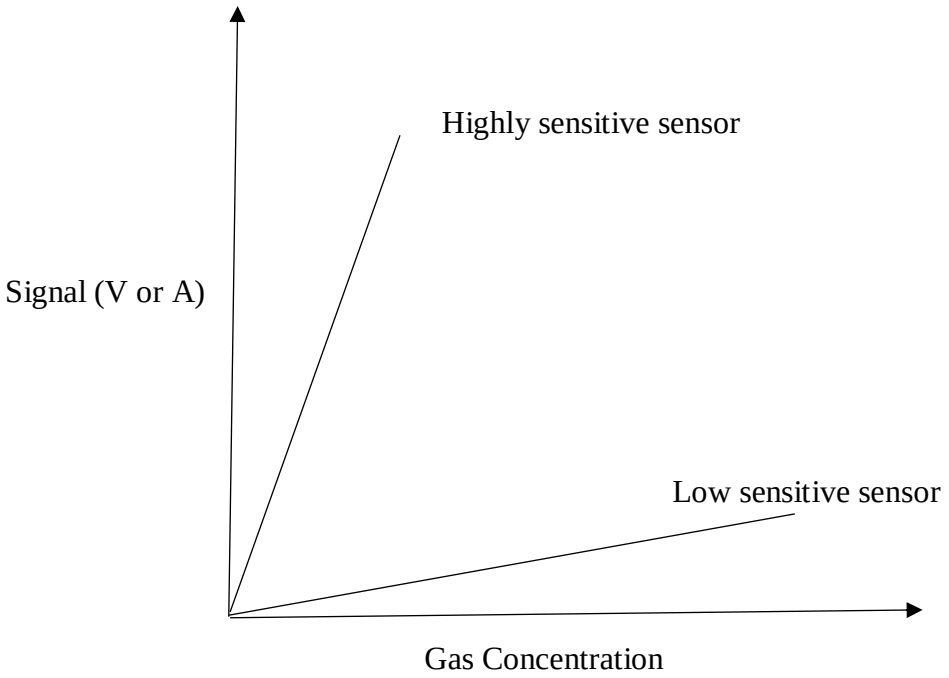

Figure 22: Sensitivity of sensor (slope of concentration vs output signal)

1.5.1 Metal oxide sensing mechanism

The chem-resistive property of the metal oxides semiconductor could be attributed to the change of the depletion layer width, space charge region, formed on the metal oxide surface. This width change acts as a potential barrier during adsorption and deportation of gas molecules on the sensor surface. The relationship between the potential barrier the metal oxide's electrical conductivity can be described in the following equation;

$$G = G_0 e^{-V_e/kT} , \quad (21)$$

Where G_0, k, and T are the electrical conductivity at zero potential barrier, the Boltzmann constant, and the absolute temperature[64]. It noteworthy that besides the nature and properties of the metal oxide material, the environmental conditions such as operating temperature, humidity and the ambient pressure can influence the sensing properties of the metal oxides.

In this work, TiO_2 nanotube is being studied as a gas sensor due to their low fabrication cost, chemical stability and high sensitivity to a wide range of reductive and oxidative gases. The nanotube structure can enhance the sensing process due to their large surface area and oxygen vacancies where the adsorption and desorption of the gas molecule take place. Also, efforts have been made to improve the performance of TiO_2 as a room temperature gas sensor by modifying their surface properties with cation and anion dopant materials. The investigated gases were Volatile Organic Compounds (VOCs) such as acetone, methanol, and ethanol, water, and gases such as nitric oxide gas and carbon monoxide.

Chapter 2

2 Modulating electronic properties and photophysics using co-doping in metal oxide nanotubes: Superlinear photoresponse

Abstract

Metal oxide nanotubes and standalone membranes have been extensively researched for potential applications ranging from electronics, optoelectronics, and photocatalysis, to filtration and gas sensing. Although the wide-bandgap of these nanotubes poses challenges for their utilization for photochemical conversion and charge transport, doped metal-oxide nanotubes provide an alternative to lower their bandgap and provide charge carriers for conduction and photochemistry. While many single dopants have been successfully used, co-dopants can be used to manipulate the electronic density of states, photophysical and photochemical properties to obtain new and unexpected functionalities, sometimes even completely different from the individual dopants. Here we describe co-doped titanium dioxide (TiO_2) nanotube membranes where the combined properties of the co-dopants differ from their monodoped counterparts, provide a detailed mechanistic model to explain the new photophysical and photochemical properties of these co-doped metal oxide membranes, and novel functionalities resulting from such properties like superlinear photoresponse.

2.1 Introduction

Doped metal oxide nanotubes offer distinctive optical, electronic, and electrochemical properties, which combined with their chemical stability and large surface area, make them uniquely suitable for solar energy and solar-to-fuel conversion applications.[21], [40], [67]–[77]. Furthermore, their tunable depletion widths,[78] and chemical gating[79] properties also make them attractive for chemical sensing[80], [81] and breath sensing devices.[82], [83]. While mono-doping of metal oxide, specifically titanium dioxide (TiO_2) nanotubes, allows reduction of their optical bandgap and suitable tuning of their conduction or valence band states[7], [84] to get useful photochemical

and photoelectrochemical properties for solar-to-fuel conversion, they do not allow a precise modulation of total electronic density of states (including both conduction and valence band) to tune their depletion width, occupancy of surface defects, and charge trapping. For examples, many studies have reported the incorporation of non-metal elements, such as nitrogen[7],[85], carbon[86], phosphorous[87], boron[88], sulfur[89] into TiO_2 nanotube lattice host material to enhance its optical and electronic properties. Also, efforts have been made to dope TiO_2 nanotube with the various transition metals such as Nb[21], Cu[90] , Zr[91] and Cr[92] in order to enhance its photocatalytic properties. By contrast, co-doping in these metal oxide nanotubes provides control of donor and acceptor states and fine-tuning of their electronic states, new and unexpected photophysical, photochemical properties like superlinear photoresponse tunable depletion width and chemical gating properties.

In this work, we report a simple, cost-effective, simultaneous and sequential cation and/or anion doping technique to mono-dope and co-dope the TiO_2 nanotubes. Nitrogen is considerate the most effective anion dopant due to its low ionization energy, comparable atomic size to an oxygen atom. The N 2p states narrow the TiO_2 band gap by overlapping with O 2p states of the TiO_2 valence band. The incorporation of nitrogen in the TiO_2 lattice site occurs in two forms, substitutional and interstitial depending on the doing method[93]. In a previous study, we have demonstrated, by using Scanning Tunneling Spectroscopy *(*STS*)* , that doping TiO_2 with N or C could induce defect states above O 2p states leading to bandgap narrowing [21],[7] . Also, the measurement suggested that the N was incorporate in the substitutional form and carbon in interstitial form.

Iron is a good cation dopant candidate owing to ionic radius similarity between Fe^{3+} and Ti^{4+} ions as well as its abundancy[94]. Therefore, we mono-doped and co-doped TiO_2 nanotube with N,

C, and Fe to provide an in-depth understanding of the influence of co-doping on the solar to fuel conversion efficiency of TiO_2 nanotube. It is noteworthy to mention that different experimental conditions, characterization, and electrochemical measurements play a crucial role in the evaluation of the samples as excellent photoactive material Table 7.

To explain the observed differences between mono-doped and co-doped nanotubes, we provide a detailed mechanistic model which explains the observed super-linear photoresponse characteristic in the co-doped nanotubes and their potential use with solar concentrator to achieve several fold-increase in the light conversion efficiency.

Table 7: Photoactivity comparison of different nitrogen co-doped samples.

Dopants	Doping Method	Photoactivity	Comparison with this work
N-Fe [95] N-Cr N-V N-Co	N: 1 Cations: 2	IPCE (420 nm) improved from 0.03 % (undoped) to 0.38 % (Fe), 0.42 % (N), and 1.52 % (N-Fe), with the loading of Co-Bi co-catalysts.	The IPCE (420 nm) improved up to about 6-fold compared to the undoped sample. Slightly higher than [30] Our co-doped sample showed a superlinear relationship between photocurrent and photon flux.
N-Mo [96]	N: 3; Mo: 4	Improved light absorption (Bandgap down to 2.5 eV) with an enhancement of methylene blue degradation by 2~3 folds (vs. N-doped)	The light absorption was enhanced (bandgap down to approximately 2.256 eV) Enhancement of methylene blue degradation with the co-doped sample. Our co-doped sample showed a superlinear relationship between photocurrent and photon flux.
N-Nb [97]	N: 1; Nb: 3	IPCE (420 nm) improved from 0.1 % (undoped) to 0.4 % (N) or 0.35 % (N-Nb), no improvement was seen with Nb.	The IPCE (420 nm) improved up to about 6-fold compared to the undoped sample. Higher than [32] Co-doped sample showed a superlinear relationship between photocurrent and photon flux.
N-V [98]	N: 3; V: 4	Significant decrease in bandgap (down to 2.25 eV). Standalone photocatalytic CO2 to CH4 reduction was enhanced up to 3 folds (vs. N-doped)	Same Significant decrease of bandgap (down to approximately 2.256 eV in N-C co-doped sample). Comparable to [33] Enhancement of methylene blue degradation in co-doped sample N-Fe. Co-doped sample showed a superlinear relationship between photocurrent and photon flux.
N-W [99]	N: 3; W: 4	Extended visible light absorption (tail of the absorption about 600 nm) with an enhancement of methylene blue degradation by 2~4 folds (vs. Undoped)	Comparable light absorption extension to visible light. Enhancement of methylene blue degradation in co-doped sample. Co-doped sample showed a superlinear relationship between photocurrent and photon flux.
N-C [100]	N, C: 3	19% Improvement in photoelectrochemical conversion efficiency with improved light absorption (Bandgap down to 2.65eV) in 550^0C annealing temperature.	Light absorption (bandgap down to approximately 2.256 eV with co-doped sample. Better than [35]. Enhancement of methylene blue degradation in the co-doped sample. Co-doped sample showed a superlinear relationship between photocurrent and photon flux.
N-S [101]	N, S: 3	Strong absorption in visible light	Enhanced visible light absorption with the co-doped sample.

Notes: 1: annealing in controlled gas (ammonia) atmosphere; 2: titanium-alloy anodization; 3: Precursor incorporation in[90] the anodization electrolyte; 4: Hydrothermal treatment;

2.2 Experimental setup

TiO_2 nanotubes (NTs) growth

Undoped and doped TiO_2 nanotube growth was described previously[21]. Briefly, a two-electrode system with a titanium foil (99.6%, 1" x 1", 0.5 mm, as the anode), a platinum sheet (cathode), and fluoride-based non-aqueous electrolyte (ethylene glycol with 0.5% NH_4F and 2% water, and various precursors for doping). Nanotube growing was processed under constant voltage (30 V) condition for three hours. Simultaneous anion doping was conducted by adding correspondent precursors into the electrolyte. A voltage switching technique was used for cation doping **Fig (23)**. Co-doping with different combinations of cation and anions can also be achieved. The conditions for doping are listed in **Table8.** All samples were annealed at 500ºC for 2 hours in an ambient atmosphere before further characterizations.

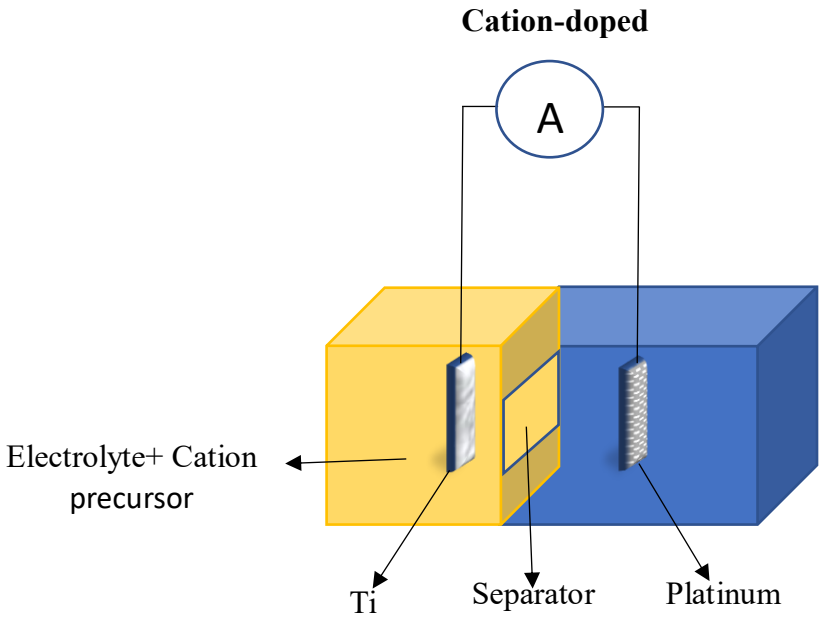

Figure 23: A sketch showing the design of a new electrochemical cell for cation doping. It has two parts separated with a porous separator to prevent deposition of cation on the Pt electrode.

Table 8: Conditions for TiO_2 nanotubes doping and detected dopant.

Sample	Anion precursor	Cation precursor	Doping technique	EDS (% atomic)
Undoped	-	-	-	-
N-doped	5% HMTA	-	PIE	5.8% N
Fe-doped	-	1% $FeCl_3$		0.07% Fe
N, C co-doped	5% HMTA, 5% ASC	-	PIE	1.2% N, 9% C
N, Fe co-doped	5% HMTA	1% $FeCl_3$	PS	5.79% N, 0.06% Fe

HMTA: hexamethylenetetramine, ASC: L-ascorbic acid, PIE: Precursor incorporation in the anodization electrolyte[90]: PS: Polarity switch. The percentage refers to weight percentage of the precursors in their corresponding solvent (ethylene glycol or water).

Scanning electron microscopy

Morphology and structure of the nanotubes were obtained by field emission SEM (JEOL JSM-7401F), with a built-in energy dispersive X-ray spectrometry (EDS) setup for elemental analysis (with Noran Software). Nanotubes on titanium substrates were sputtered with gold before the measurements.

Ultraviolet-visible (UV-VIS) spectroscopy

Optical spectra of TiO_2 nanotubes were characterized with a VWR UV-1600PC spectrophotometer. Free-standing nanotube samples were scraped from the Ti substrates (with a

doctor blade) and suspended in DI water for the measurements.

Electrochemical characterization

Electrochemical characterizations were performed with a Bio-logic SP-200 potentiostat, using a three-electrode configuration in argon-purged 0.5 M (pH = 6.5) Na_2SO_4 solution. Ti/TiO_2 (TiO_2 nanotubes grown on Ti substrate), platinum wire, and Ag/AgCl were used as working, counter, and reference electrodes, respectively. Electrochemical and photoelectrochemical (with 1 SUN, 100 mW/cm^2 irradiation using a 300 W xenon lamp) characterizations[102]–[107] were conducted with the following parameters:

Linear sweep voltammetry (LSV)

Scan rate: 10 mV/s, range: -1.0 ~ 2.5 V, with and without light irradiation.

Electrochemical impedance spectroscopy (EIS)

DC bias: 0.2 V, AC amplitude: 10 mV, frequency range: 100 kHz ~ 100 MHz.

Mott-Schottky analysis

Scan range: -1.0 ~ 1.6 V, frequency: 1 kHz, AC amplitude: 10 mV.

Open circuit potential (OCP)

The OCP was firstly monitored in dark to stabilize the readings, followed by irradiation until the change of OCP was small. The OCP decay curves were recorded after switching the light off.

Incident photon-to-current efficiency (IPCE)

IPCE was measured with chronoamperometry technique under 0.5 V (vs Ag/AgCl ref) bias, using monochromatic light (every 10 nm interval, from 600 to 350 nm, generated from a 150 W halogen lamp through a monochrometer (Princeton Instruments, Model: FA2448), with known irradiation

flux measured with a calibrated intensity meter (Newport, Model: 1918)) as excitation source. IPCE was calculated using the following formula;

$$IPCE(\lambda) = \frac{j_{ph}(mA \cdot cm^{-2}) \times 1239.8(V \times nm)}{P_{mono}(mW \cdot cm^{-2}) \times \lambda(nm)} \quad (22)$$

Where j_{ph} is the photocurrent density, and P_{mono} and λ are the intensity and the wavelength of the monochromatic light, respectively.

Photocatalytic methylene blue degradation test

Photocatalytic degradation of Methylene Blue (MB) was carried out in a capped quartz cuvette with a total amount of 150 nmol methylene blue solution and wireless Ti/TiO_2 samples (~ 1 cm^2 exposure area). The whole system was irradiated with 365 nm UV light (3 mW/cm^2) under gentle stirring. The absorption of the solution was measured at 0, 10, 40, 80 and 120 min using a calibrated UV spectrometer (VWR UV-1600PC), and the decrease of the absorption peak at 670 nm was used to calculate the quantum yield of MB degradation.

2.3 Result and discussion

The TiO_2 nanotube membranes were fabricated by using electrochemical anodization techniques, with tunable length, diameter, wall thickness by control of the applied voltage, growing time, and electrolyte composition. Simultaneous doping with different species was reported previously[21] , using either precursor-charged electrolyte (for anion doping) or polarity-switching technique (for cation doping). With different anion, cation combinations (Table 8), co-doped (anion-anion, cation-cation, anion-cation) TiO_2 nanotubes can be grown. Using the experimental parameters described above, we have obtained TiO_2 nanotubes with different co-dopants (anion-anion, anion-cation, etc.). Optical (ultraviolet-visible or UV-Vis) spectra also indicates the

incorporation of dopants and modulation of their optical bandgap. While Fe-doped and N, Fe-co-doped nanotubes show a minor change of the light absorption; N-doped and N, C co-doped samples show a clear extension of light absorption into the visible light region **Fig (24, b)**. The magnitude of the spectra shift could be attributed to the amount of the dopant in the nanotubes. Also, the anion-anion co-doped visible light absorption enhancement could be attributed as well to increase in carbon solubility compared to the mono-doped carbon content in our previous work[7] as shown in the element atomic percentage detected by EDS (**Table 8**).

The performance of the undoped/doped TiO_2 nanotubes in solar energy to chemical fuel conversion (converting photons-to-fuel) were evaluated using wired and wireless configurations. Compare to the standalone (wireless) test, measurements taken in a wired configuration, or with a photoelectrochemical device not only provides the total efficiency (or quantum yield) for

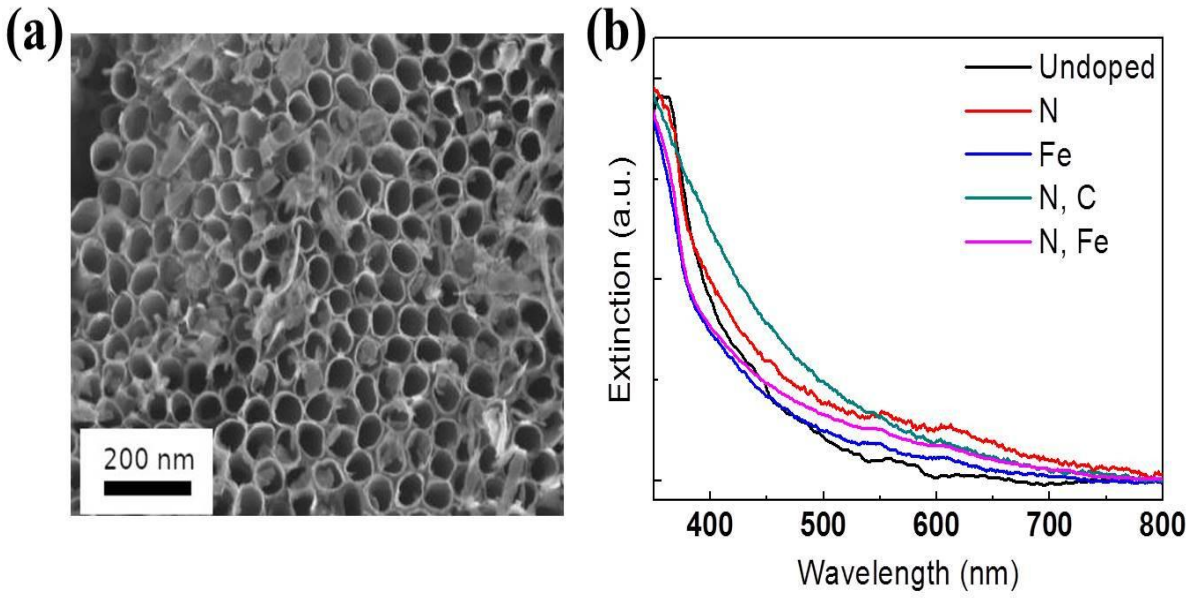

Figure 24: Field-emission scanning electron microscopy (FESEM) image of doped TiO_2 nanotubes(a). Ultraviolet-visible (UV-VIS) spectrum of undoped/doped TiO_2 nanotubes(b).

conversion of light into chemical fuels, but also reveals the efficiency of separate optoelectronic processes involved in the solar to chemical conversion, including the light capture, charge carrier generation, carrier transport and charge injection to the substrates. The nanotube array grown on the titanium substrate was directly used as photoelectrodes (photoanodes). Using a three-electrode configuration with TiO_2 nanotubes as the working electrode, current-voltage (I~V) behaviors were studied under dark and incident irradiation on the backside of the working electrode. Net photocurrent measured in photodynamic condition (Linear sweep voltammetry) is shown **in Fig (25, a)**, and the magnitude directly reflects the efficiency of solar energy conversion. Compared to other nanotubes, Fe-doped samples generate much lower photocurrent, showing no saturation behavior even up to 1.6 V applied bias. photocurrent saturation plateau usually appears around 1.2V[7],[84]. This indicates higher carrier charge trapping with iron doping, where a higher bias is required to fully collect the generated carriers and prevent charge recombination similar to Cu doped TiO_2 nanotube[84]. The anion mono-doped and co-doped photoanodes exhibited higher photocurrent response owing to bandgap narrowing, optical absorption enhancement.

To study the photoresponse of these nanotubes with different energy photon excitation, the incident photon-to-current efficiency (IPCE) measurements were conducted using the above mentioned LSV experiment setup. From the IPCE spectra, the onset of photocurrent with photon energy (noted electrochemical or "EC" bandgap) can be determined **Fig (25, b).** Similar to the optical spectra, EC bandgap shows a red-shift due to sub-bandgap light absorption. N-doped sample shows the highest energy conversion efficiency across the whole spectra. Co-doped (nitrogen with carbon or iron) nanotubes show better photoresponse in the longer wavelength spectra but surpassed by undoped nanotubes at higher energy part.

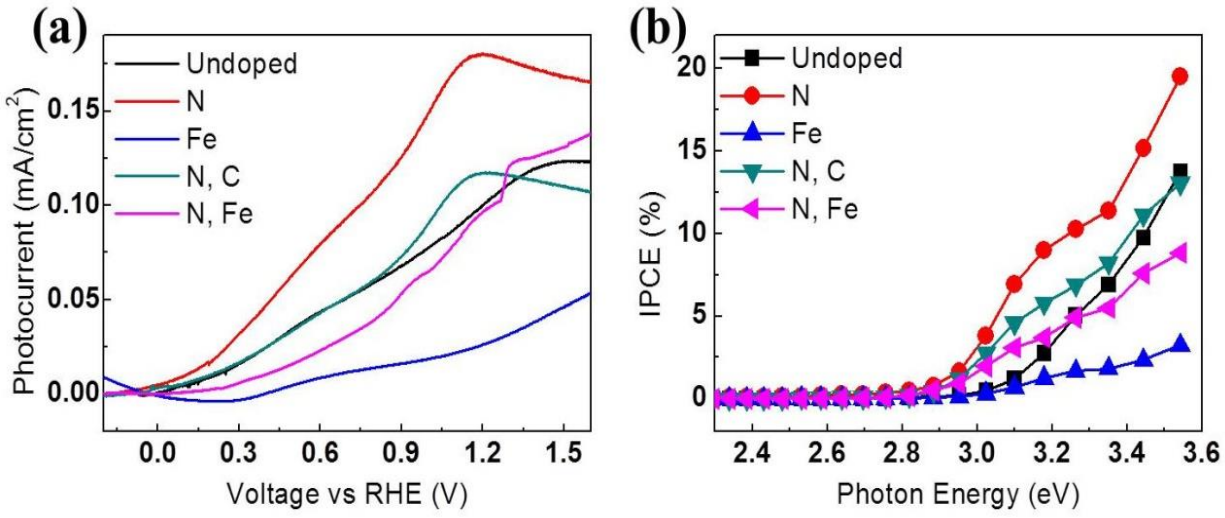

Figure 25 : (a) Photocurrent (difference of current density in dark and under light irradiation) generation from TiO_2 nanotube photoelectrodes, using linear sweep voltammetry (LSV) in a three-electrode configuration. (b) Incident photon-to-current efficiency (IPCE) of the nanotube photoelectrodes, measured in a three-electrode configuration (with 0.5 V bias vs. Ag/AgCl).

The photocurrent and IPCE measurements provide information on the efficiency of these nanotubes in solar energy conversion. However, it can be difficult to directly relate these efficiencies to the individual photon, charge carrier-involved processes. Therefore, we need to conduct characterizations to decouple these processes in order to fully understand the dopant (anionic, cationic, or both) effects. As the IPCE can be expressed as;

$$IPCE = \eta_{abs} \times \eta_{transport} \times \eta_{transfer} \quad (23)$$

Where the three efficiencies are related to light absorption, charge transport to the nanotube surface, and the charge transfer from to the surface adsorbed species (water in this case).

First, the charge transfer efficiency can be quantified by measuring how fast the surface-accumulated holes inject to water. The hole injection lifetime (or rate constant: k = 1/t) can be measured using the open circuit potential (OCP) change of the photoelectrode. Under irradiation, electron-hole pairs are generated, followed by hole transport to the photoanode (nanotube) surface

and cause the quick drop of OCP. The equilibrium between carrier generation, recombination and hole transfer to surface adsorbed water lead to a stable OCP value under continuous light excitation. Once the irradiation is switched off, the hole consumption through charge injection leads to the decay (exponential increase) of the OCP. And the charge transfer rate constant (k_{ct}) can be calculated using the following relationship;

$$V_{OCP} = A - Bexp(-k_{ct}t)\,, \tag{24}$$

where A, B are constants. A higher value of k_{ct} refers to a higher charge transfer efficiency. While no significant change of carrier injection lifetime was seen in Fe- or N, C-doped nanotubes, a two- to three-fold increase of rate constant was observed in N- and N, Fe-doped samples, indicating fast removal of photogenerated holes for water oxidation **Fig (26,a).**

Second, the efficiency of charge transport from the bulk semiconductor to the surface was evaluated by using the impedance, including the resistive and capacitive contributions. This was measured with electrochemical impedance spectroscopy under AC perturbation. In our study, the Nyquist plot is used to represent the relationship of capacitive impedance (imaginary part) and resistive impedance (real part). The impedance spectra **Fig (26, b)**, can also be fitted to an equivalent circuit **Fig (26, c)**, to help clarify the electronic transportation inside the nanotubes. This equivalent circuit contains three serially-connected parts for describing the solution (solution resistance Rs), solution-nanotube interface (charge transfer resistance R_{ct}, and double-layer capacitance C_{dl}) and the bulk nanotube (space charge layer resistance (R_{sc}) and capacitance (C_{sc}), charge trapping resistances and capacitances (R_1~R_3, C_1~C_3), which can be used for evaluating the electronic processes of charge conduction through electrolyte, charge transfer from nanotube

surface to water, and charge transport (including charge trapping) inside the nanotubes. Here, we evaluated how different (kinds of) dopants could affect the hole transport inside the nanotubes. Dopants could either be ionized to provide free carriers or act as trapping centers and ease the electron-hole recombination process. Therefore, charge trapping should be minimized in the nanotubes, and a smaller total capacitance ($C_{total} = C_{sc} + C_1 + C_2 + C_3$) is preferred. With single dopants (nitrogen or iron), we observed an increase of C_{total} (**Table 9, row 5**) indicating higher charge trapping. The large value of total capacitance in Fe-doped nanotubes is due to the formation of deep dopant levels, which could lead to severe electron-hole pair recombination and hence lower photocurrent generation (or energy conversion efficiency). On the other hand, co-doped samples (nitrogen with carbon or iron) show similar or even lower total capacitance compared to undoped nanotubes. The lower charge trapping is mainly attributed to the synergistic effect of co-dopants in charge compensation and removal of deep traps, which could help improve energy conversion efficiency. Apart from charge transport inside the bulk nanotubes, the charge transfer resistance extracted from the equivalent circuit can be used to evaluate the ease of hole injection to water. The N-doped and N, Fe co-doped nanotubes show about one magnitude smaller resistance than other samples, and similar to the OCP decay assay, these two samples show the highest charge transfer efficiency for water oxidation.

To further quantify the photophysical and photoelectrochemical properties of these co-doped nanotubes, the Mott-Schottky analysis was used to study the potential-capacitance behavior of these photoanodes. Useful characteristic parameters including the flat band potential and carrier density were calculated from the Mott-Schottky equation for n-type semiconductors,

$$C_{sc}^{-2} = \frac{2}{\varepsilon q N_d}\left(E - E_{fb} - \frac{k_B T}{q}\right) \quad (25)$$

$$C_{sc} = {}^{-1}/_{2\pi f Im(Z)} \quad (26)$$

where $\varepsilon = 31\varepsilon_0$ is the dielectric constant of the TiO_2 nnanotube, f is the frequency (Hz) used in the measurements, Im(Z) is the imaginary part of complex impedance (Ohm). Positive slopes of the nanotubes show typical n-type semiconductor characteristics. N-doped samples show a two-fold increase of the free-carrier density (**Table 9, row 6**) due to large doping amount, while Fe-doped samples show no significant change in carrier density due to lower iron incorporation. Interestingly, co-doped samples show lower carrier density compared to N-doped nanotubes, which could be explained by the charge compensation as mentioned previously. Doping also modifies the flatband potential of the nanotubes, as indicated by either the negative or positive shift of the Mott-Schottky curve **Fig (26,d)** Small negative shift of the flatband potential observed in Fe-doped nanotubes indicates n-type doping character of iron, and a positive shift in N-doped samples indicates p-type doping character of nitrogen. Due to charge compensation, co-doped samples show more negative flatband potential compared to the N-doped nanotubes.

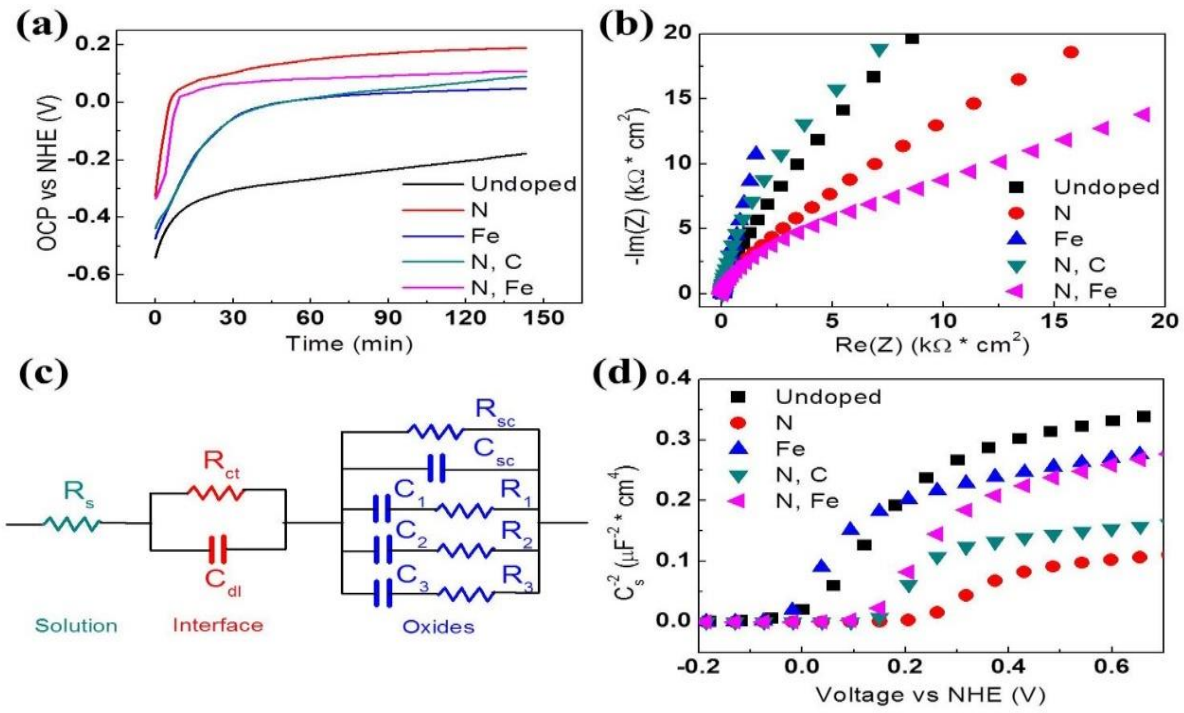

Figure 26 : (a) Open-circuit potential (vs. NHE) decay of TiO_2 nanotube photoelectrodes after switching off the light irradiation. (b) Nyquist plot of the EIS measurements, showing the imaginary and real part impedance of the nanotube electrodes. (c) Equivalent circuit diagram for fitting the impedance data. (d) Mott-Schottky plot of the TiO_2 nanotubes.

Table 9: Parameters extracted from (photo)electrochemical characterizations.

	Method	Undoped	N	Fe	N, C	N, Fe
J_{ph} (mA/cm^2)	LSV, 0.5 V vs Ag/AgCl	0.088	0.172	0.022	0.109	0.080
E_{pec} (eV)	IPCE	3.07	2.91	3.01	2.87	2.88
k_{ct} ($10^{-3}s^{-1}$)	OCP decay	0.967	2.27	0.954	0.870	2.77
R_{ct} ($k\Omega \cdot cm^2$)	PEIS	34.1	8.8	42.6	64.9	7.15
C_{total} ($\mu F/cm^2$)		21.1	26.8	320.4	15.7	21.9
n ($10^{18}cm^{-3}$)	Mott-Schottky	4.12	9.71	3.85	5.04	4.16

To further explore the photodynamic of charge carriers in these nanotubes, we conducted light-intensity dependent photocurrent measurement with the variation of incident photon energy (sub-bandgap to UV photons). The results are represented in a log-log plot, where the slope of the linear fit indicates different power laws of the photon flux-dependent photocurrent generation. Interestingly, both co-doped (N, C, and N, Fe) samples show increasing slopes with photon energy, which is the different from undoped or mono-doped nanotubes (cation- or anion-doped nanotubes) reported previously.[7], [84] Nominally, doped nanotubes demonstrate superlinear slopes with

bandgap excitation due to charge trapping, but higher energy photons demonstrate a linear relationship with photon flux. To describe this intriguing interplay of different photophysical processes in co-doped nanotubes, we developed a model **Fig (27,a)** to describe the photogeneration, charge recombination, trapping effect, and charge injection in these TiO_2 nanotubes.[7], [76], [84]. The photogenerated electron-hole pairs can be quenched through conduction band-valence band recombination, conduction band-hole dopant (or acceptor state) recombination, electron donor (or donor state)-valence band recombination, acceptor state-donor state recombination, electron trap-assisted recombination. Further, the photogenerated charge carriers can also be injected into adsorbed water molecules, leading to a photocatalytic or photoelectrochemical reduction of water to fuel molecules. These charge carriers can be generated directly from the conduction band, valence band, donor state, or acceptor state excitation. Due to the large concentration of donor and acceptor states in these co-doped nanotubes, the electrons relax from the conduction band to donor states quickly and holes "cool" down from the valence band to the acceptor states, effectively converting the nominal TiO_2 semiconductor conduction-valence band states into "hot-carrier" states. Therefore, since most of the photogenerated electrons and holes now reside in the nominal doped states of donors and acceptor in co-doped nanotubes. At steady state, using the charge balance and charge neutrality relationship, we can derive:

$$\frac{dp_a}{dt} = g - \alpha p_a n_d - \beta p_a n_t - r_a \times p_a \tag{27}$$

$$\frac{dn_d}{dt} = g - r_t n_d \left(1 - \frac{n_t}{N}\right) + r_{dt} n_t - r_a \times p_a \tag{28}$$

$$n_d + n_t = p_a \tag{29}$$

$$R = r_a \times p_a \tag{30}$$

where n_d is electron density in the donor state, and p_a is the hole density in the acceptor state; n_t

and N are trapped electrons and the total number of trap states available; r_t and r_{dt} are trapping and detrapping rate between donor state/conduction band and electron trap states; α is the rate constant for donor state-acceptor state recombination; β is the rate constant for trap-assisted recombination for acceptor state; g is the photogeneration rate; R is the photocatalysis rate, r_d and r_a are corresponding rate constant for electron and hole injection. The observed photocurrent is linearly proportional to the rate of photocatalysis (R). The key observation is that the entire photophysics is dominated by the dopant states in these co-doped nanotubes, compared to their mono-doped counterparts.[7], [84].

Unimolecular recombination results in linear slope between the rate of photogeneration and STFC rate (R∝g), which occurs in trapping-dominant recombination ($\alpha p_a n_d \ll \beta p_a n_t$). In this regime (observed for bandgap electrons in co-doped nanotubes, **Fig (27, b, c)** the primary recombination process occurs between the trapped electrons and photogenerated holes. Bimolecular recombination between photogenerated electrons and holes ($\alpha p_a n_d \gg \beta p_a n_t$) results in square root dependence between STFC rate with incident light intensity $R \propto g^{0.5}$. However, it is not observed in co-doped TiO_2 nanotubes due to the large recombination rate between trapped electrons and photogenerated holes, and the strong density of electron traps (oxygen vacancies) present in these metal-oxide nanostructures. In the case where the density of traps N is large,

$$g = \alpha p_a n_d + \beta p_a n_t + r_a \times p_a \,, \tag{29}$$

$$r_t n_d \left(1 - \frac{n_t}{N}\right) = \alpha p_a n_d + \beta p_a n_t + r_{dt} n_t \,, \tag{30}$$

Since we get,

$$n_d = p_a - n_t, \tag{31}$$

$$r_t(p_a - n_t)\left(1 - \frac{n_t}{N}\right) = \alpha p_a(p_a - n_t) + \beta p_a n_t + r_{dt} n_t, \quad (32)$$

Therefore, $n_t \propto p_a^{-x}$ and $g \propto p_a^{(1-x)}$, where x is between 0 and 1. This results in superlinear slope $R \propto g^{1/(1-x)}$, and the only photophysical regime observe din these co-doped nanotubes, which depends on the trapping rate and recombination rate. When illuminated with higher energy photons, the barrier height for charge trapping (using Marcus's electron transfer theory) decreases, leading to larger trapping rates, and hence more superlinear slope.[7], [76], [84], [108]. This relationship was confirmed experimentally between the photocatalysis rate and the input photon flux, using the intensity-dependent photocurrent measurement, using the same setup as for IPCE measurement. We this trend in both nitrogen-carbon, and nitrogen-iron co-doped TiO_2 nanotubes **Fig (27,b,c)**. With the increase of photon energy, the intensity-dependent photocurrent showed a transition from linear to superlinear **Fig (27,d)**, pointing to change in mechanism from the trap-dominant recombination, to photophysics dominated by trapped electrons (large number of trapped electrons due to excitation to higher energy electron states and lower activation energy for electron trapping) and photogenerated holes in donor state. This superlinear can be particularly useful for improved photodetection and increasing STFC rates for higher energy photons, especially with increasing photon flux.

The solar to chemical conversion efficiency was also evaluated using with a wireless configuration. Using a traditional method to measure the capability of the photocatalyst in organics degradation, photocatalytic methylene blue (MB) degradation tests were conducted. The light-induced holes were injected to the MB, and the oxidative degradation leads to the fading of MB, which can be quantified by the change of absorption at 670 nm **Fig (28, a).** The reaction shows first-order kinetics and the quantum yield of the photocatalytic reaction can thus be calculated from the amount of MB degraded using chemical stoichiometry. The quantum yield showed the same

trend as in the wired PEC test **Fig (28,b),** with a small quantum yield increase in N, Fe-co-doped samples likely due to improved light absorption and negligible dopant trapping.

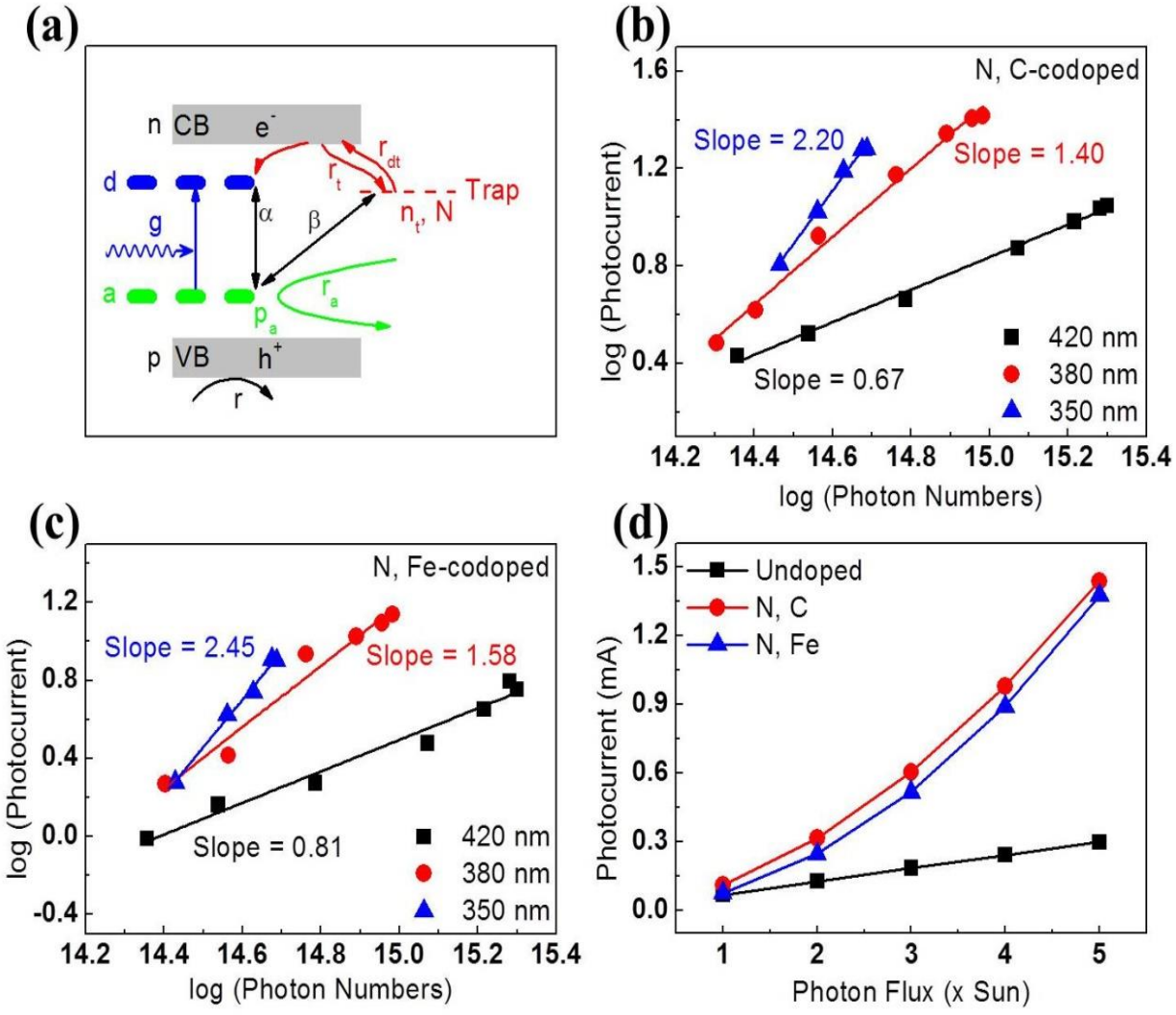

Figure 27: (a) Mechanisms of the photophysical processes (photogeneration, charge recombination, trapping, and injection) in the nanotubes under photon excitation. (b, c) Log-log plot of light intensity-dependent photocurrent of (b) N, C-co-doped and (c) N, Fe-co-doped TiO_2 nanotubes excited using monochromatic light at different wavelengths. (d) Photocurrent with photon flux, the photocurrent is calculated by integrating IPCE with AM 1.5G solar spectra.

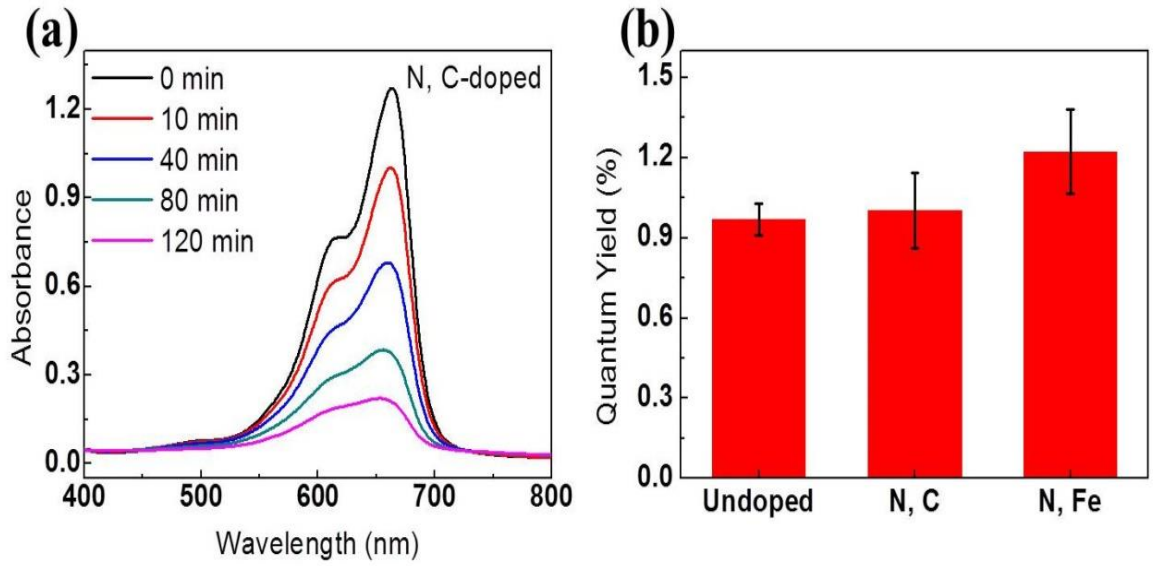

Figure 28: Photocatalytic methylene blue (MB) degradation with standalone TiO_2 nanotubes , showing the (a) decrease of MB absorption (around 670 nm, with N, C-co-doped nanotubes) and (b) the calculated quantum yield (QE).

2.4 Conclusion

Electrochemical anodization of Ti in a two-electrode electrochemical cell, with Ti as the anode and platinum mesh as the cathode, is by far the most used technique for TiO_2 nanotubes fabrication . Also, the nanotube morphology can be tuned and controlled by changing the anodization parameters such as the applied voltage, time, electrolyte composition and electrolyte pH.

In this work, a simple, inexpensive, simultaneous and sequential cation and/or anion doping technique to mono-dope and co-dope the TiO_2 nanotube was demonstrated. Mono-doping (N, Fe), co-doping (N-C, N-Fe) and undoped TiO_2 metal oxide nanotube were investigated as efficient materials for solar energy harvesting and solar-to-fuel conversion applications. Optical UV-Vis results indicated the successful incorporation of the dopant elements causing optical bandgap narrowing and found to successfully extend the absorption of TiO2 nanotube into the visible light

region. The photoelectrochemical water oxidation activity of the N doped and N-C/N-Fe was improved due to the effective separation of generated electron-hole pair and the promoted the electron transfer to the reaction sites. A detailed mechanistic model which explains the observed super-linear photoresponse characteristic in the co-doped nanotubes was developed. The new photophysical properties such as superlinear photoresponse, makes these chemically stable TiO_2 co-doped nanotubes attractive for photochemical and photoelectrochemical solar-to-fuel conversion.

Chapter 3

3 Synthesis and electrochemical performance of modified TiO_2 nanotube as anodes material for Li-ion Battery

3.1 Introduction

Without energy storage, renewable electricity generation such as wind and solar will be much less viable. Lithium-ion batteries (LIBs) are widely used as energy storage and power source for modern electronic devices such as cell phones, laptops and electric vehicles[109][110]. However, the safety and the durability of the currently used LIBs has become the main cause of concern that needs to be resolved in order to have safe, high energy/power density batteries. The safety concern of current used LIBs is mainly associated with the decomposing of the organic solvent-based electrolyte, which can cause ; i) increase in the battery internal pressure due to gas generation, ii) formation of lithium dendrite during Li intercalation/deintercalation [41],[111].

Currently carbon-based material such as graphite is the most used anode material in LIBs owing to their relatively high energy, long cycle life, and abundance[112]–[115]. However, their lithium intercalation/deintercalation voltage is low ,about 0.1V, which is near the decomposing voltage of the organic electrolyte[116]–[118]. Moreover, its low operating voltage could possibly lead to the formation of the lithium dendrite on the surface of the graphite, due to the high polarization, leading to short circuits and battery failure[119], [120]. Therefore, another class of materials such as transition metal oxides, MnO, CuO, ZnO, and TiO_2 has been widely investigated as alternative LIBs negative anode materials. These materials show relatively high Li-ion storage capacities, good cycling stability, and safe lithium intercalation voltage profile [121]–[126]. Lately, the feasibility to synthesis tuned nanostructure morphology of the metal oxides could enhance the electrolyte infiltration, fasten Li-ion diffusion, reduce the concentration polarization and provide large surface area for more intercalation/deintercalation sites.

Among several transition metal oxides, TiO_2 is considerate a very promising anode material owing to its safe lithium intercalation/deintercalation voltage(1.7 V vs Li/Li^+)[127]–[135], low volume

expansion (less than 4%) upon lithium intercalation and deintercalation, excellent cycling life, low cost and low toxicity[136]. However, the full application of TiO_2 as anode active material still far from the commercialization due to its low electronic conductivity (10^{-12}-10^{-7} S/cm^2) and poor lithium ionic diffusivity. However, nanostructures material such as self-organized TiO_2 nanotube could improve its electrochemical performance since the nanotube morphology has a large surface area that can enhance the diffusion kinetics via shorting the pathway of the charge transport. Another alternative strategy to improve TiO_2 anode performance is to combine the TiO_2 nanotube with conductive materials in order to enhance electronic properties [137], [138]. A further strategy to improve the electrical conductivity and create more space and site for storage and diffusion of the lithium-ion is to dope the nanotube with anion and/or cation elements [21]. Among different dopant element, Nitrogen is considered one of the most effective anions doping in terms of photocatalysis application[7]. However, there have only been limited studies on N-doped TiO_2 nanotube for LIBs applications.

The self-organized TiO_2 nanotube can be fabricated by anodizing Ti substrate in electrolyte contains a small amount of fluoride ion and its morphology such as length, pore diameter, and wall thickness can be tuned by controlling the anodization parameters (Voltage, electrolyte composition ,time)[139]–[141]. In the current study, TiO_2 nanotube was doped with N simultaneously by adding a small amount of the nitrogen precursor in the anodization electrolyte. Then we explore the effect of crystallinity and doping on electrochemical performance of the TiO_2 nanotube. We show that the nitrogen-doped electrode has increased the specific capacity and improved the cycling stability.

3.2 Preparation method

The titanium foil was purchased from STREM CHEMICALS, INC. purity 99.7% thickness 0.127 mm and cut into the desired dimension. Before anodization, the samples were degreased in acetone, ethanol deionized water in an ultrasonic bath for several minutes. Afterwards, the samples were chemically polished by dipping them in a mixture of a hydrofluoric acid (48 wt.%, Macron chemicals) and nitric acid (68 wt.%, Avantor) 1: 3 in volume for 15s. Then the samples were ultrasonicated in deionized water and dried in a N_2 stream.

Two-step nanotubes were prepared by first anodizing the Ti coupons at 40V for 4 h in a conventional electrochemical cell with Pt gauze as the cathode, and 1.27 cm^2 Ti coupons (protected backside) as an anode. The separating distance between the working and counter electrodes was 2cm. The grown film was peeled from the coupons by using scotch tape followed by ultrasonication in deionized (DI) water for 2 seconds. The second step anodization was conducted using the same pretreated procedure (4h at 40V). The nanotube growth was conducted at room temperature (~ 23 ºC) and the electrolytes for different samples are listed in **Table 10.**

After anodization, the samples were washed with deionized water and heat-treated at 300ºC in vacuum for 2 hours, then the samples were thermally treated at 550ºC in air to enhance crystallinity.

Table 10: Fabrication conditions for N-doped and undoped TiO_2 nanotubes.

	Undoped	Nitrogen
Solution Ethylene glycol	2% DI water, 0.5% Ammonium fluoride (NH_4F)	2% DI water, 5% hexamethylenetetramine, 0.5% ammonium fluoride (NH_4F)

Characterization of TiO_2 nanotube

The morphology and structure of TiO_2 nanotube were studied via a field-emission scanning electron microscope (TESCAN MIRA3 LMH Schottky). The Phase identification of the annealed doped and N-doped TiO_2 samples was made by using X-ray diffraction XRD, using a Scintag XDS 2000 X-ray diffractometer with Cu Ka radiation at 45 kV and 40 mA. The elemental composition was performed by energy-dispersive X-ray spectroscopy (EDS) embedded in an FE-SEM to investigate the nitrogen and carbon species and contents.

Electrochemical measurements of TiO_2 anode

The as-fabricated TiO_2 nanotubes were directly used without any additional binders or conductive agents since the backside of the TiO_2 nanotube electrode was used as a current collector. All electrochemical measurements were performed using CR2032 coin cell assembled in an argon-filled glovebox, H_2O and O_2 levels below 0.1 ppm, with Li foil as the counter electrode, glass fiber (GF/A, Whatman) as a separator. The electrolyte is 1.0 M LiPF6 in ethylene carbonate/diethyl carbonate (1:1 in volume).

Galvanostatic charge/discharge measurements were performed using a potential range of 0.7–3.0 V (versus Li+/Li) under different current densities. The specific capacity and current density were calculated based on the mass of TiO_2 nanotube which was measured by weighing the samples before and after sonication for 10h and strip the residual nanotubes by adhesive tape.

3.3 Result and discussion

To examine the crystallinity of the TiO_2 nanotube, XRD measurements were performed before and after anodization. All observed XRD diffraction peaks of the as-prepared TiO_2 corresponds to Ti metal which implies that the resulting samples after the anodization are amorphous TiO_2. The XRD diffraction peaks of the ambient air heat-treated samples can be assigned to anatase phase rather than rutile or brookite phases. **Fig (29)** shows main peaks at (101) (004) at 2θ= 25.14º and 38.4º respectively. The XRD results of the N doped TiO_2 nanotube shows that the crystal structure was preserved, no secondary phase, even after high level of N doping **Fig (29)**. The absence of the secondary could be attributed to the fact that Nitrogen (N^{3-}) and Oxygen (O^{2-}) ions have close radii 0.171 and 0.14 nm respectively[142]. Comparable ions radii usually lead to uniform incorporation of the dopant in the host material.

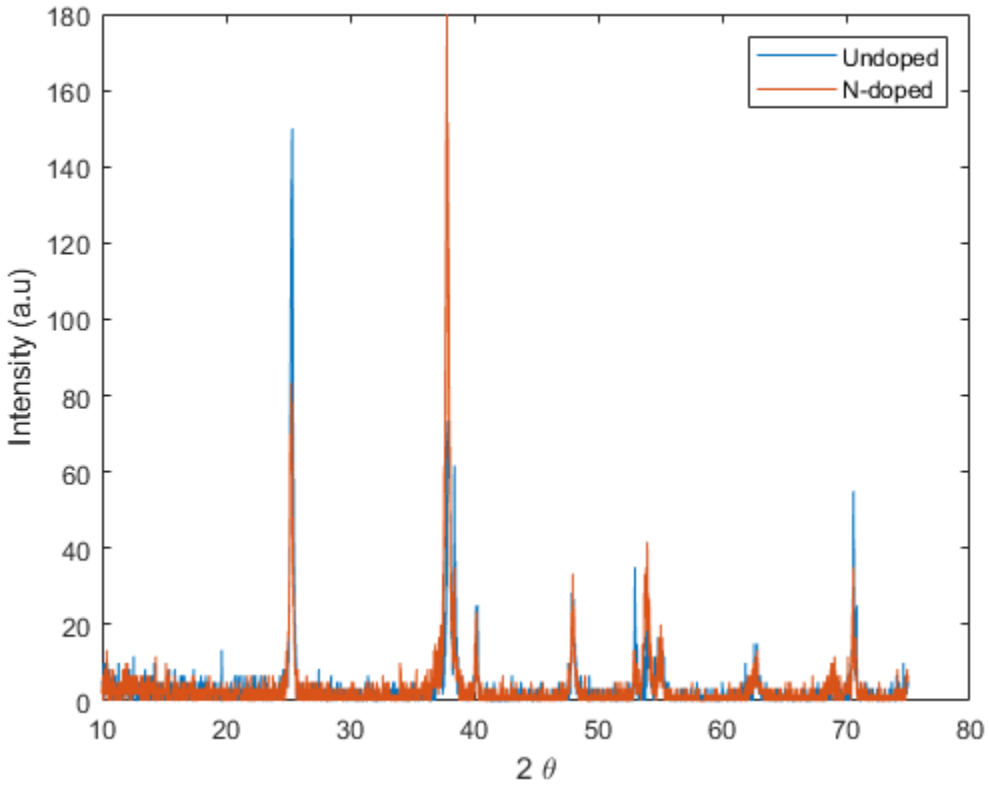

Figure 29: XRD patterns for undoped (blue) and nitrogen-doped (red) samples. All diffraction peaks corresponding to the anatase TiO_2 phase, indicating the absence of a secondary phase.

The electron micrographs SEM images show highly tubular, open-ended, and vertically aligned structure on the Ti substrate with 100nm pore diameter and less than 7nm wall thickness and structure is well preserved before and after doping **Fig (30, a, b)**.

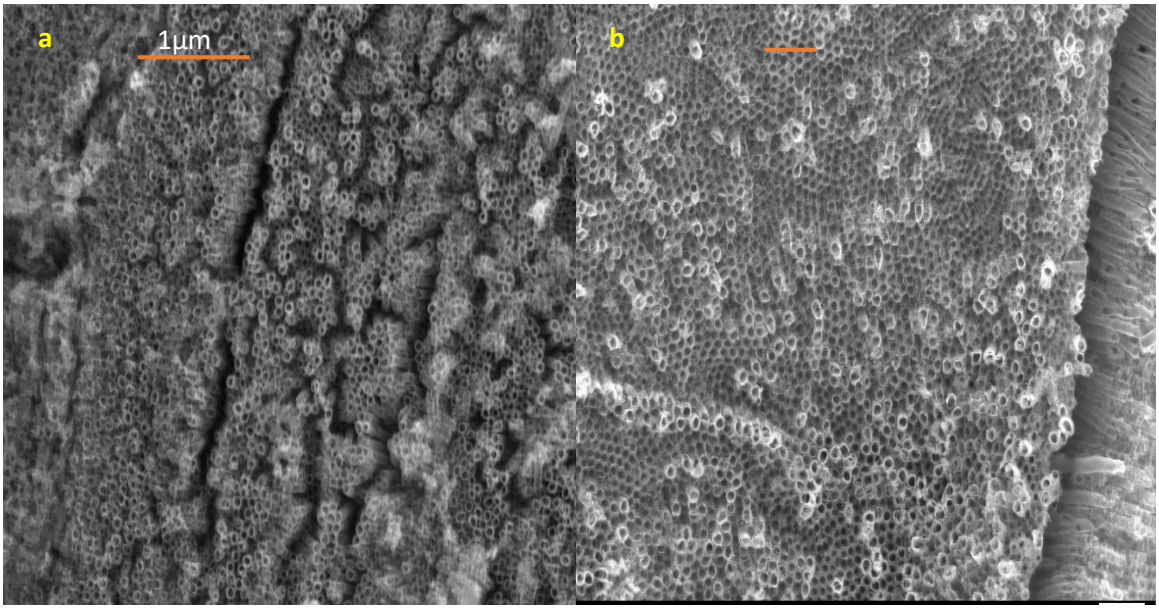

Figure 30 : Scanning electron micrographs (SEM) of TiO2 nanotube grown by electrochemical anodization (a) undoped, (b) nitrogen-doped.

The energy-dispersive X-ray spectroscopy (EDS**) Fig (31, a)** confirms the presence of N species in the TiO_2 nanotube and was calculated to be 1.99% in the anodization electrolyte contains 5% nitrogen precursor. However, the EDS result has revealed that the amount of dopant N species rely on the amount of the dopant precursor added to anodization electrolyte **Fig (31, b).** Also, EDS result confirms the presence of carbon species due to successful incorporation of the carbon in the residual electrolyte during the heat treatment.

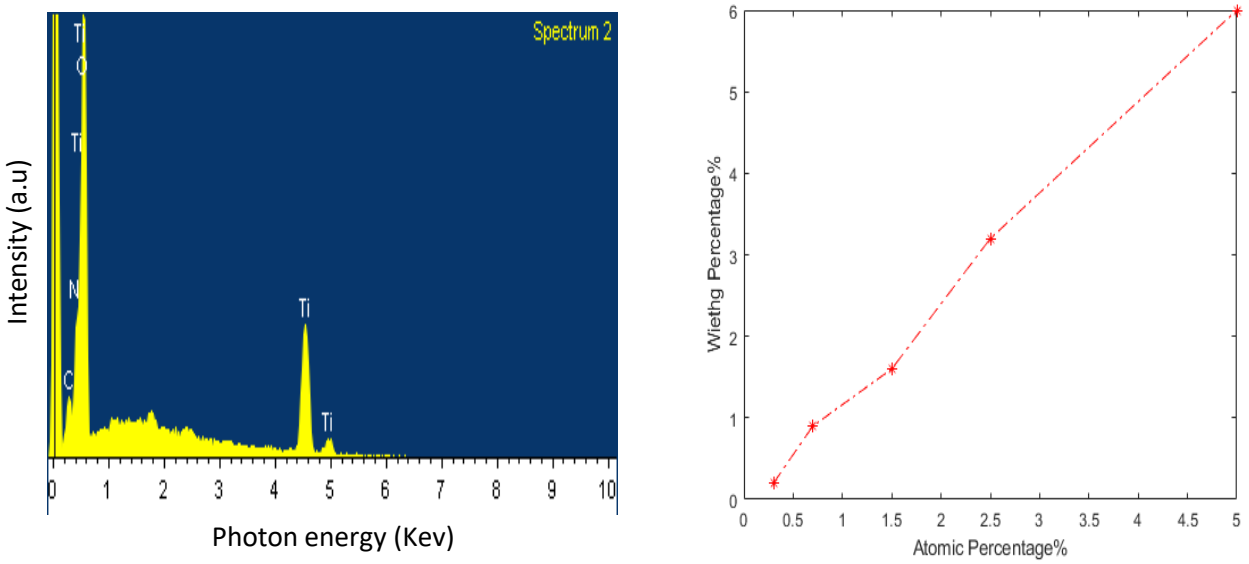

Figure 31: Energy dispersive spectroscopy (EDS) for N-doped (a). N concentration as function in N precursor weight in the anodization electrolyte (b).

Li reversible intercalation/deintercalation into polymorphs TiO_2 can be described as following;

$$TiO_2 + x\ Li+ + x\ e- \leftrightarrow Lix TiO_2\ (0 \leq x \leq 1). \quad (33)$$

Where x is the inserted lithium mole fraction which depends on the morphology and the crystal structure. The Ti^+ in tetragonal geometry of the TiO_2 anatase and rutile polymorphs is surrounded by 6 oxygen atoms forming octahedron geometry. The formed octahedral and tetrahedral sites between these octahedrons is thought to be the Lithium-ion intercalation/deintercalation sites.

In theory, the maximum theoretical specific capacity pure crystalline TiO_2 is about 334mAh/g. This capacity can be obtained when all octahedral and tetrahedral sites are filled by Li ions with $L1TiO_2$ composition.

Many Studies has revealed that electrochemical performance of the TiO_2 nanotubes as LIBs electrodes depend strongly on polymorphs, morphology, and modification such as elemental doping with anion or cation species[136]·[143].

First, the electrochemical properties of the undoped amorphous and crystalline sample are shown in **Fig (32, a).** The result shows charge/discharge galvanostatic test curves of the first cycle with the cut-off voltage range of 3-1 V vs Li/Li+ at 5mA/g. In the amorphous electrode, there is no well-defined lithium intercalation/deintercalation potential plateaus. Also, the profile of voltage vs intercalation/deintercalation shows a monotonic decrease in the potential which can be attributed to the different thermodynamics lithium intercalation reactions[144]–[146] since the amorphous phase has disordered structure and a large number of defects. The small pseudo-plateau at about 1.25V appeared due to irreversible phase Transition [147]. The initial charge and discharge specific capacities are about 400 and 300 mAh/g with 25% first cycle loss. respectively. The first cycle loss can be attributed to the creation of the solid electrolyte interface (SEI) on the TiO_2 nanotube upon the first lithium insertion due to undesired side reaction. Moreover, the first 18 reversible capacity cycles exhibit slight continuous fading **Fig (33, a)** with good coulombic efficacy. By contrast, there are well defined the lithium intercalation/deintercalation potential plateau of the crystalline TiO_2 nanotube, anatase, during the insertion and extraction of the Li from the interstitial octahedral sites of anatase TiO_2. **Fig(32, b)** shows voltage vs charge/discharge capacity curves of the first cycle, showing the Li-intercalation into the crystalline phase at approximately 1.73V whereas deintercalation potential is slightly higher about 1.88V. The initial charge and discharge specific capacities are about 220 and 160 mAh/g with 24% first cycle loss. Also, the first 16 reversible capacity cycles showed continuous fading **Fig (33, b)** with good coulombic efficacy similar to the amorphous sample.

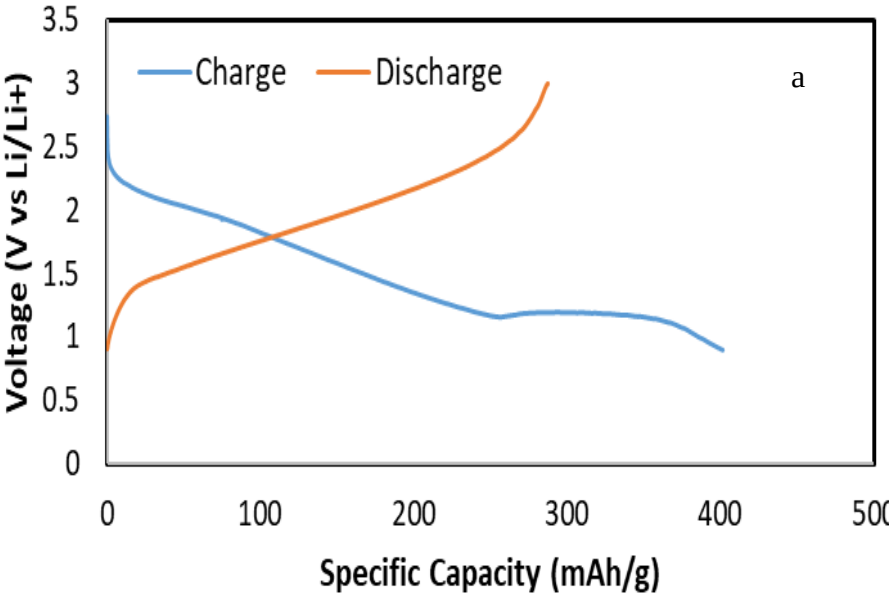

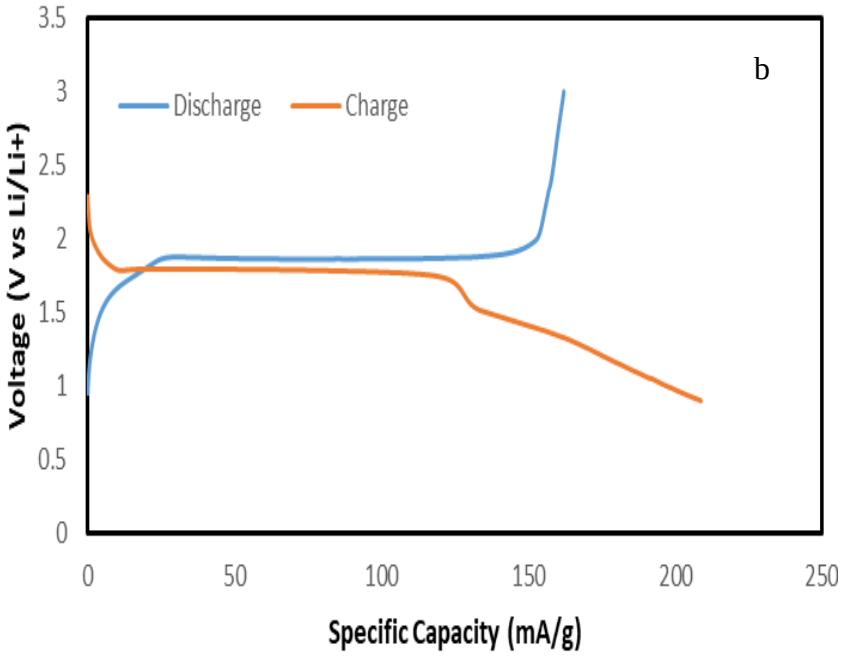

Figure 32: First cycle charge/discharge of as-prepared TiO_2 nanotube (amorphous) (a), and crystalline TiO_2 nanotube (anatase) (b).

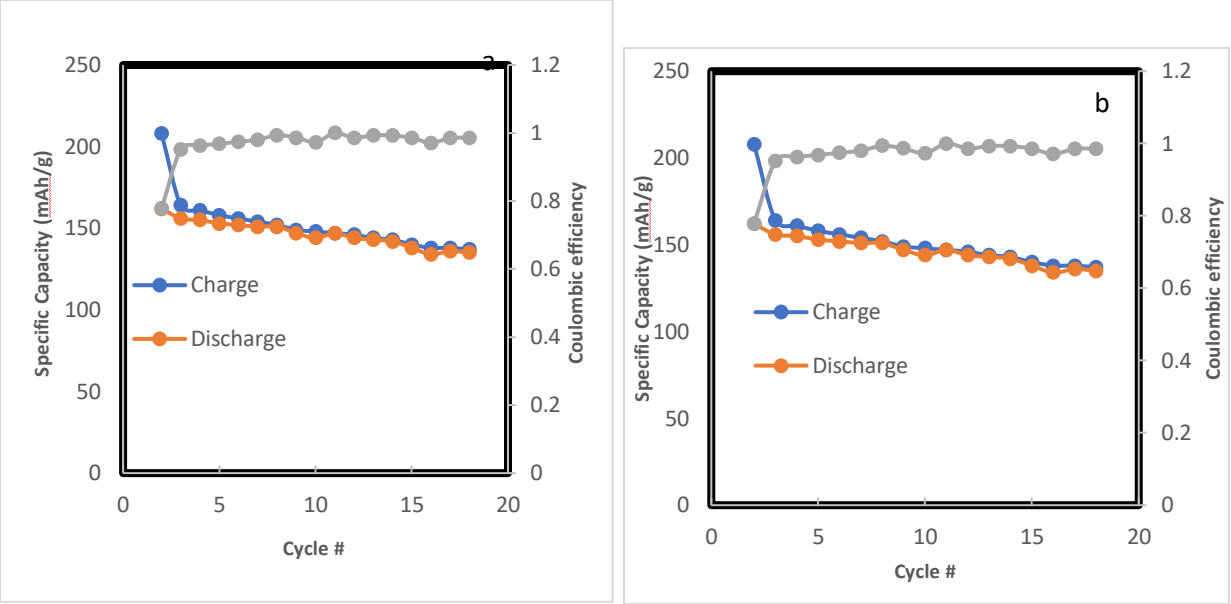

Figure 33: Coulombic efficiency and the first 18 charge/discharge cycle of (a) amorphous TiO_2, (b) crystalline TiO_2 nanotube (anatase).

Fig (34) shows the first three charge-discharge profile of N-doped and undoped sample run at very low current density 10mA/g. All the samples display a pair of S-shaped voltage profiles, which is the typical voltage plateaus of bulk TiO_2. The first charge/discharge capacity for the undoped nanotube 380mA g h^{-1} resulting in a coulombic efficiency of >90%. The initial capacity loss of the undoped sample could be due to Li-ion lost at undesirable irreversible sites inside the anatase crystal and solid electrolyte interface formation. On the other hand, the first discharge/charge capacities of the N-doped sample have increased by approximately 25% compared to the undoped sample. Both doped and undoped sample shows larger specific capacities than the theoretical of the TiO_2 and this could be attributed to the presence of carbon as extra doing species or thin carbon coating layer on the TiO_2 nanotube surface.

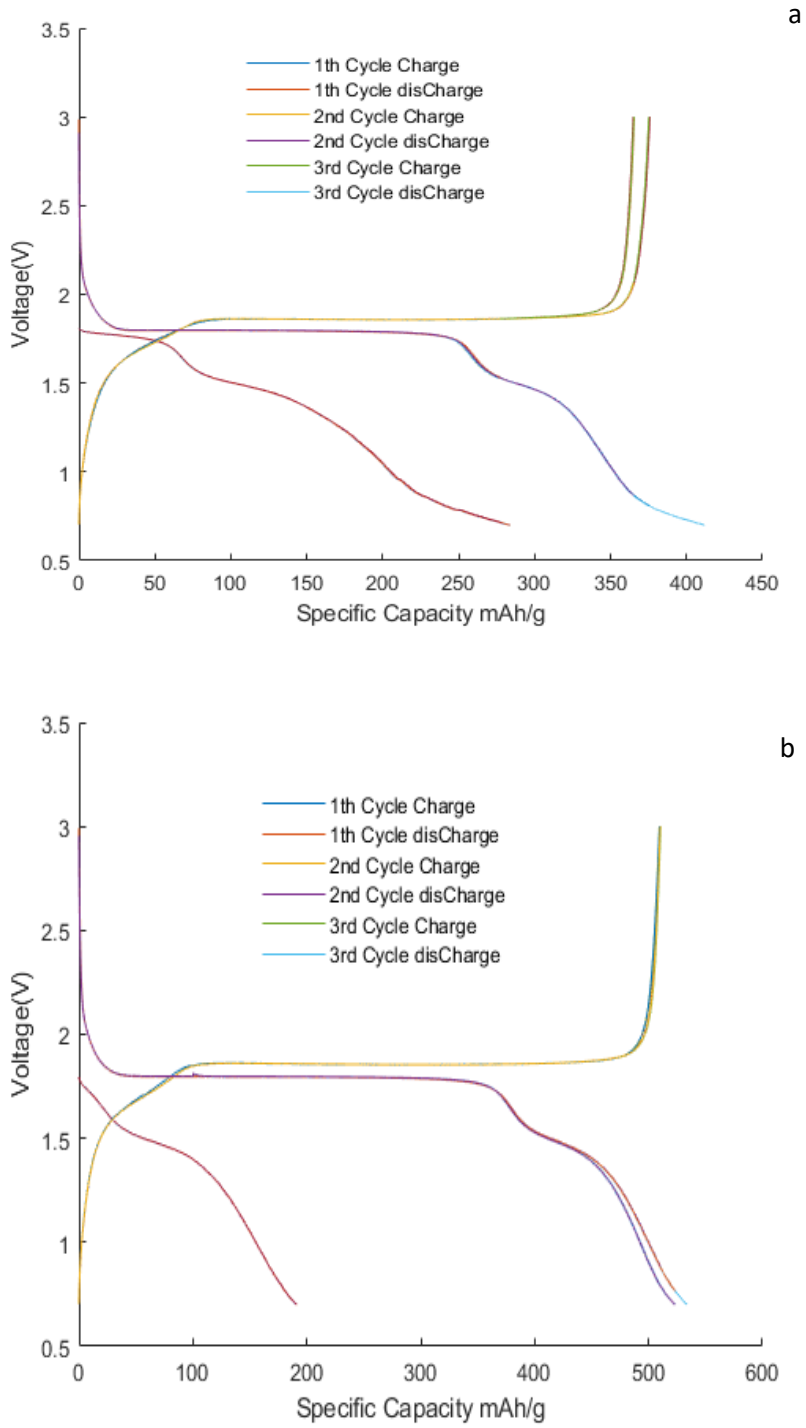

Figure 34: The first three charge/discharge voltage profiles of (a) Undoped sample, (b) N-doped sample at very low current density 10mA/g.

The cycling rate electrochemical performance of the undoped and N-doped TiO_2 run at different current densities: 10, 15, 20, 25, and 30mA/g are shown in **Fig (35).** The undoped sample showed a slightly rapid decrease in capacity in the first 8 cycles at 10mA/g current density.

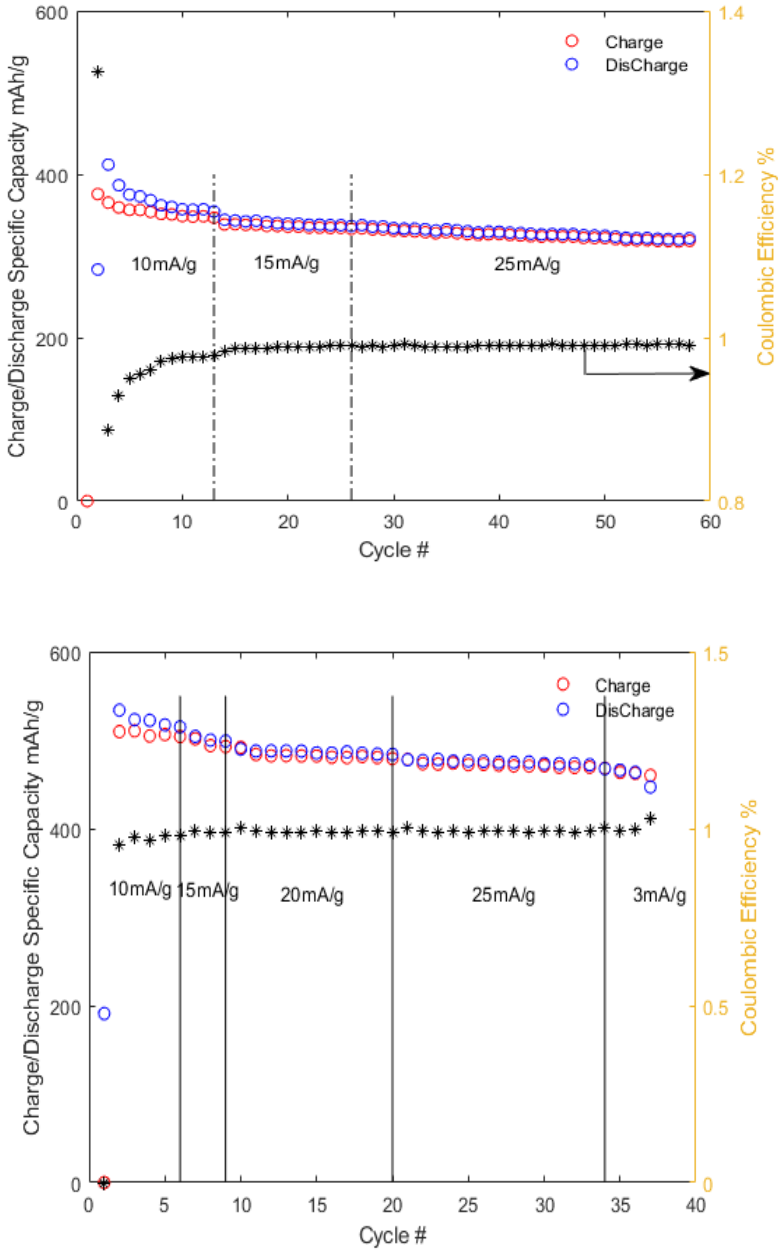

Figure 35 : Cycling rate electrochemical performance of (a) undoped and (b) N-doped TiO_2.

By contrast, the N-doped sample has less decline profile with starting stability at the 4th cycle at the same current density. When the current density increased rate increases to 25 mA/g the N-doped still show a higher capacity of 480mA/g, while TiO_2 shows just 300 mA/g. Moreover, the specific capacity of the N-doped sample is slightly more stable at higher current density compared to the undoped sample.

One possible explanation of the higher specific capacity of the undoped TiO_2 compared to its theoretical capacity is that the formation of the composite electrodes made from TiO_2 nanotube and a thin layer of the carbon film. The carbon film could possibly be formed due to our special two-step heat treatment of the as-prepared TiO_2 nanotube **Fig (36),** this assumption is further proved by EDS results that showed high Carbon content despite that fact that TiO_2's carbon solubility is low. The carbon thin layer can improve the electrochemical performance by taking more lithium and increasing the electron transfer.

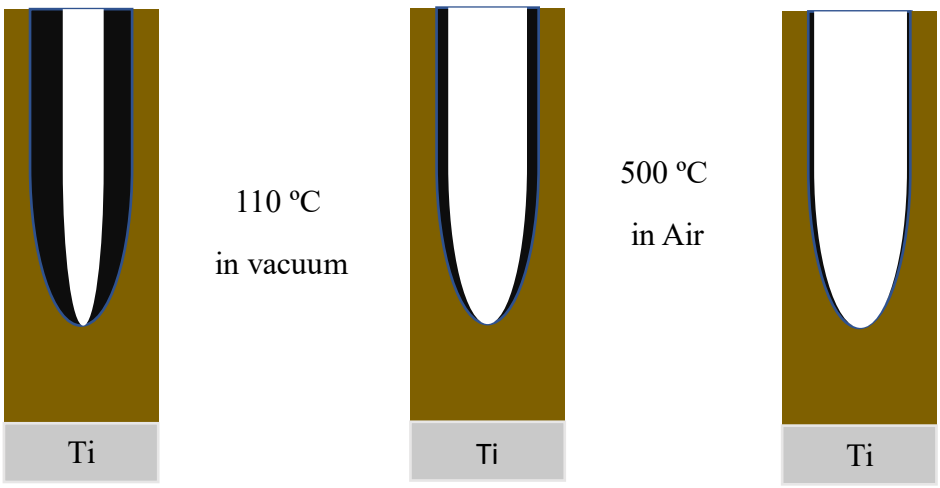

Figure 36: Schematic of the formation of thin carbon conductive layer on the TiO_2 surface.

Also, the high capacity of N-doped sample can be attributed to an increase in the unit cell inter-atomic distances and creating more lithium storage sites.

3.4 Conclusion

In conclusion, we introduce a sample, inexpensive and environmentally friendly route to fabricate doped and undoped metal oxide nanotubes as efficient anode materials for Lithium-ion application. The as-formed nanotubes are amorphous and anatase phase appeared after heat treatment in ambient air at 550°C. The electrochemical tests revealed that amorphous TiO_2 nanotube has higher first cycle discharge specific capacity than crystalline nanotube 400 mAh/g and 210 mAh/g respectively. However, about 25% of the capacity appears to be reversible for both samples with continuous capacity fading in the first 16 cycles. We Also investigated the electrochemical properties of N-doped TiO_2 nanotube anode which displayed a 25% increase in the capacity compared to undoped TiO_2 nanotube anodes fabricated and tested under the same conditions.

Chapter 4

4 Three-dimensional architecture of lithium-anodes made from graphite fibers coated with thin-films of silicon oxycarbide: Design, performance, and manufacturability

Abstract

Silicon oxycarbide (SiCO) is an amorphous molecular network of SiCO tetrahedra anchored to graphene-like carbon. The graphene forms a three-dimensional cellular network with a domain size of ~5 nm. Therefore, nanometer-thick films of SiCO grown on graphite may be expected to have unusual behavior. We grow these films on a bed of commercially available graphite fibers that serve the dual function of a current collector. The electrochemical behavior of the composite is measured as a function of the thickness of the SiCO films. Thick films approach the typical behavior of bulk SiCO (which has three times the capacity of graphite but suffers from poor first cycle efficiency). However, films, approximately 100 nm thick, show high first cycle efficiency as well as high capacity. The composite performs better than the prediction from the rule-of-mixtures, which further substantiates the unusual behavior of the thin-film architecture. The Raman spectra of these thin films also differ from bulk SiCO. The development of thin graphite fibers, with a high surface to volume ratio that has the same capacity as the current graphite-powder technology, coupled with the manufacturing of these thin-films by a liquid-polymer precursor based process can propel these results toward commercialization.

4.1 Introduction

The silicon-oxycarbides (SiCO) are a relatively new anode material for Li-ion batteries. They have the following special attributes,

(i) Their capacity ranges from 500 to 1000 mAh/g, which varies with the molar concentrations of the constituents[148], with the highest values being obtained near

the middle of the C-Si-O composition triangle e since they are amorphous and their composition varies, their capacity cannot be prescribed a theoretical value.

(ii) They have a pseudo-amorphous, molecular network structure constructed from a cellular graphene-like carbon, with a domain size of ~5 nm. Tetrahedral units of silicon, carbon, and oxygen are anchored to the graphene[149]. Thus, at the molecular level, they comprise a combination of silicon, carbon, and SiO_x, which, on their own, are candidates for anode materials. An analysis of Li-capacity data spanning a wide range of compositions, coupled with a nanodomain model for the structure of SiCO compounds, has shown that their high capacity arises from the migration of Li to the mixed bond C-SiO tetrahedral units[57].

(iii) SiCO materials have low density, typically 2 g/cm^3 and, therefore, an open molecular network, which enhances the diffusivity of Li within[150], leading to a good performance at high C-rates [151]. The low modulus and low volumetric expansion upon intercalation, which has been measured to be less than 8% (unpublished), endows very good cyclic stability and high resistance to failure. The chemical inertness of SiCO promotes safety.

(iv) The silicon oxycarbides are made from silicone resins, also known as siloxanes and silsesquioxanes. The silicon-carbon-oxygen chemistry is built into these liquid polymers and can be varied widely[152]. They convert to the inorganic phase when heated to 800-1000^0C. Thus, they are potentially low cost, not only as raw materials, but also from the point of view of manufacturability. The liquid polymer route can open the way for fabricating nanocomposites of various kinds for example by mixing the precursor with particles of silicone to further improve performance.

Up until now, SiCO has been implemented as anodes in powder form. The polymer precursor is cross-linked by heating to ~300 ºC, milled into powders and then pyrolyzed by heating in an inert atmosphere at ~800 ºC, which are then processed into anodes in the same way as graphite powders. The SiCO powders show high capacity with three times the capacity of graphite, good C-rate performance, and cyclic endurance, but suffer from low first cycle efficiency (65%-75%), and large hysteresis between charge and discharge cycles (0.75 V-1 .25 V) [153]. Since the intrinsic structure of these materials consists of graphene networks on the scale of ~5 nm, we wondered if films of them grown on graphite may lead to better properties. (Earlier work on thin films deposited on copper substrates did not show an improvement[154].) At the same time, a novel processing approach also presented itself where we were able to deposit thin films of SiCO using a flash-pyrolysis method where a small amount of the liquid precursor was sprayed onto a web of carbon fibers and pyrolyzed in just a few seconds at 800^0C[155]. The nearly perfect wetting of all surfaces of the fibers within the fiber-matt allowed all fibers to be immediately covered with thin films of SiCO. Films of nanometer thicknesses could be made by diluting the polymer precursor in a solvent and reducing the amount of this solution sprayed on to graphite-fiber matt. Successive cycles of deposition, repeated in quick succession, could be used to build up the film thickness to the desired level. The choice of graphite fibers in these experiments was limited by those available off-the-shelf. These widely available fibers are optimized for making graphite-reinforced-polymer-composites for structural applications; they are far from being optimized for Li sequestration. In the experiments reported below, we have therefore characterized their electrochemical behavior, as a baseline for evaluating the results after they have been coated with thin films of SiCO. The premise of these experiments was that the nature of the interface between the graphite and the SiCO films grown on it may influence the structure of the films. Thus the

synergy between the fibers and the coatings are studied in two ways, (i) first by increasing the thickness of the coating, expecting that whereas thick coatings would tend toward the bulk behavior of SiCO, thin coatings may reflect the nature of the graphite-SiCO interface, and (ii) by adding the Li capacity from the fibers and form the coating using the rule-of-mixtures, to see if the thin-film behavior deviates from it.

4.2 Preparation method

The anodes were prepared with Toray TGP-H-030 graphite paper. According to the manufacturer the fiber mesh has only 20% fill density, with an overall physical density of 0.4 g/ cm^3. The fibers are impregnated with a polymer resin. The paper is specified to have a flexural strength of 40 MPa, and flexural modulus of 8 GPa. The average fiber diameter was 7 mm. The polymer residue in these fibers (5% PTFE) was removed by heat-treating at 1000^0C in argon for 1 h. Coupons, 0.5″ in diameter, were punched from the fiber fabric. The fiber mesh was brittle and fragile after this heat treatment procedure. The coupons weighed 6.5-7.0 mg apiece. The polymer precursor for SiCO, 1 3,5,7-tetramethyl-tetravinylcyclotertrasiloxane (TTCS) was purchased from Gelest, USA. It was mixed with 1 wt% dicumyl peroxide, which served as a catalyst for cross-linking. If needed the precursor was diluted with THF, a common solvent. The SiCO-GF anodes were prepared in the following way. A drop of the precursor solution was placed on the fiber coupon. It spreads immediately over all surfaces of the fibers in the mesh. It is then cross-linked at ~170^0C, and finally pyrolyzed at ~800^0C when it converts into the amorphous SiCO ceramic phase. The last step was carried out in two ways, (i) by gradually heating the specimen, at a rate of 10^0C min^{-1} to the pyrolysis temperature, and holding for 5 h in argon atmosphere, and (ii) by flash pyrolysis where the specimen was exposed to approximately 800^0C under a radiant furnace for a few seconds. The

latter process was conducted within a glove box in an argon atmosphere with the oxygen content of less than 1 ppm. Both methods gave identical electrochemical behavior. Before the coating was applied the 0.500 diameter coupons were fragile, but after the coating, they were mechanically resilient and could be bent without fracture. The thickness of the coating could be anticipated by the following analysis. We write the coating thickness as δ, the fiber diameter as d, and the weight fraction of SiCO as Ws, the density of graphite and SiCO as ρ_G and SiCO, ρ_S. Consider a single fiber of a unit length; its weight is given by π (d^2 /4) ρ_G. Since $\delta \ll d$, the weight of the coating is given by $\pi d\ \delta\ \rho_G$. Therefore,

$$Ws = \frac{\pi\ \delta d \rho S}{\left(\frac{\pi d^4}{4}\right)\rho G + \pi\ \delta d \rho S} \tag{34}$$

Rearranging Eq. (1) leads to the following result

$$\frac{\delta}{d} = \frac{1}{4}\frac{\rho G}{\rho S}\frac{Ws}{1-Ws} \tag{35}$$

The fiber diameter was approximately 7 µm. Therefore, Ws of 5% and 10% translates into δ= 100 nm and 200 nm, setting (ρ_G /ρ_{SiCO}) ~ 1 since both have a density in the 2.0- 2.3 g/cm^3 range. Micrographs of the graphite mesh before and after coating with 11 wt% SiCO, along with their Raman spectra are shown in **Fig (37).** The enhanced contrast in **Fig (37, b)**, relative to bare fibers in **Fig (37, a)**, is most likely induced by the greater electron reflectivity of higher molecular weight SiCO. The Raman spectrum of the coated fibers is remarkably different from that of the bare fibers. The coating shows a sharp G peak, with broad shoulders that reach far, while the fibers show the characteristic D and G peaks of graphite. The Raman spectrum for SiCO [156] is included in **Fig (37, c)**; it is similar to that of the graphite fibers. In summary, the dual D and G peaks are seen in powder-SiCO, are replaced in the SiCO films by a single G peak with broad-reaching shoulders on either side of the peak.

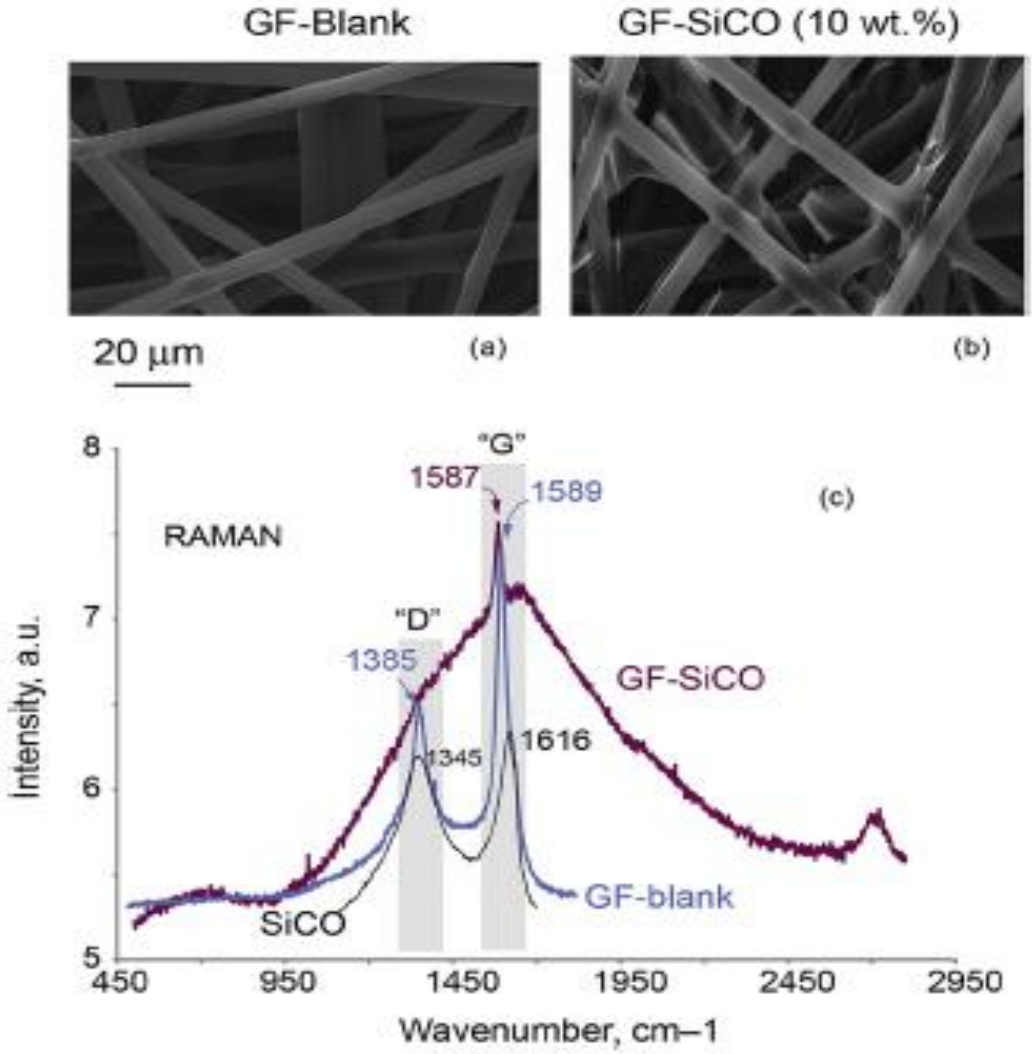

Figure 37: (a) and (b) Micrographs of GF-blank and GF-SiCO (c) Raman spectra for the fiber mesh, the coated fiber mesh, and SiCO by itself.

4.3 Electrochemical testing

The coupons prepared in the way described above are ready for electrochemical testing since the graphite fibers also serve as the current collector; the mesh makes electrical contact with the bottom cap in the CR2032-type coin cell. The liquid electrolyte permeates through the entire thickness of the electrode. Lithium-metal foil was used as the counter electrode, soulbraine1.0 M LiPF in EC/DEC ¼ 1/1 (V/V) as the electrolyte, and WhatmaneGlass Microfiber the membrane-

separator. The batteries were assembled, crimped and closed in an argon atmosphere. The principal variable in the electrochemical characterization was the current density, which ranged from 15 mA g^{-1} to ~600 mA g^{-1}, corresponding to absolute values of 0.1, 0.5, 1, 2.5 and 5 mA. (The current densities are expressed in terms of the total weight of the anode equal to the sum of the weight of the graphite fibers and SiCO.) The electrochemical cycles were constrained between 3 V and 0.01 V. In one instance we also tested the absolute capacity by holding the cell at 0.01 V at the end of the current cycle until saturation was achieved. The specific capacity, first cycle efficiency, hysteresis, and cyclic fading were measured. Baseline data were obtained for uncoated graphite-fiber coupons. The electrochemical properties of the composite were measured as a function of, *Ws* the weight fraction of SiCO. The data for the composites were analyzed by the rule-of mixtures.

4.4 Results

In a typical experiment, the cells were subjected to 10 cycles. (In one instance the cyclic durability was tested for GF-blank and GF-SiCO for more than 300 cycles.) The Coulombic efficiency and the capacity were measured as a function of the current density and the weight fraction of SiCO. The Coulombic efficiencies, after the first cycle, were always very close to 99.9%, and are therefore not reported; they can be approximately judged from the cyclic data, which is included in the graphs. The first cycle efficiency, however, is an important measure of performance, and is reported in detail. The hysteresis between the charge and the discharge cycles was measured as the voltage difference at the mid-point of the final capacity.

4.4.1 **Capacity, first cycle efficiency, and fading**: a comparison

Results from GF-blank and GF-SiCO are compared in **Fig (38, a-d)**. In all instances, the composite shows a significantly higher capacity than the GF-blank. The graphs in **Fig (38, a)** and **Fig (38, b)** compare the data obtained at ~15 mA g^{-1}, and at ~400 mA g^{-1}. **Fig (38, c)** shows the change in capacity with a continuous increase in the current density. **Fig (38, d)** gives the cyclic durability at 81 mA g^{-1}; note that while GF-blank fails after ~275 cycles, the composite continues to perform well at >300 cycles.

The variability in the capacity in **Fig (38, c)** is notable. Lowest variability and the highest capacities are obtained at 16 mAg^{-1}. The variability is somewhat abated by the SiCO coating but remains an unusual feature of these results. We have conjectured that perhaps the electrical resistance of the fiber bed may have varied because of the uncertainty in the mechanical force that is used to press the coin cells. Therefore, we measured the change in the electrical resistivity of the fiber bed under mechanical pressure. The specimens for these measurements were cut into 32 mm x 32 mm squares from the graphite paper. The thickness of the paper was 110 mm. Silver paint was applied to the opposite edges of the sheet; the electrical resistance was measured between these edges. Pressure was applied by placing a weight on the paper. The voltage was measured as a function of the current up to 250 mA; the overall slope was linear supporting Ohmic behavior.

The resistivity of the uncoated fiber mesh was 0.036-0.040 Ωcm without the pressure, and 0.031-0.035 Ωcm with the pressure. The resistivity of the coated fiber mesh was 0.042 Ωcm and remained unchanged under pressure.

Therefore, electrical resistance cannot explain the variability in electrochemical performance. We now suspect that bubbles may have become trapped within the fiber mesh during electrolyte

infiltration, resulting in variable performance. Future experiments will continue to explore the origins of this variability.

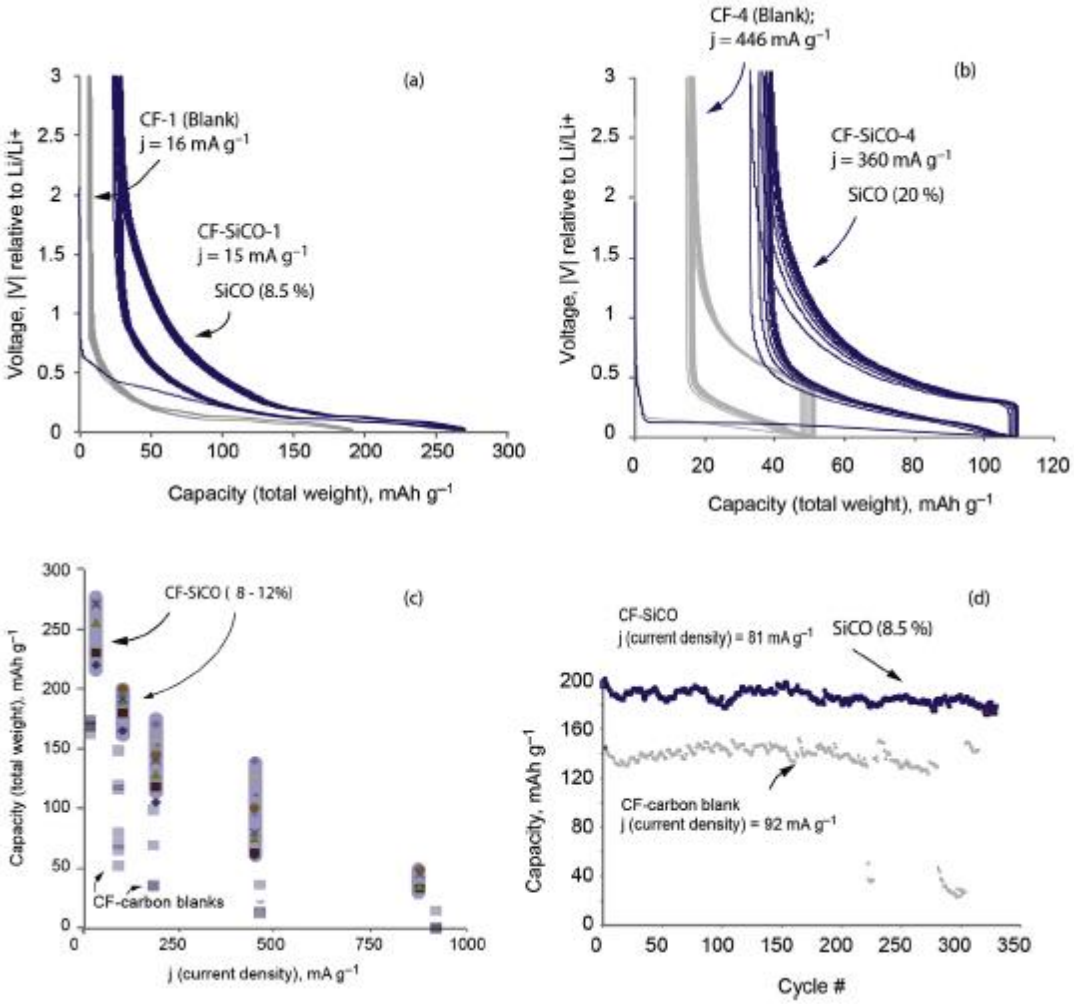

Figure 38: A comparison of SiCO-GF performance relative to GF-blanks. Note that the fiber-based anodes have a higher capacity (a), lower hysteresis (b), less variability (c) and much better resistance to failure (d).

The hysteresis of bulk SiCO and SiCO films deposited on copper show a high hysteresis, in the range of 0.75 V-1.25 V [153], [154]. In Fig. 2(a) it is about 0.25 V. We find such low hysteresis to be a consistent feature of the GF-SiCO electrodes.

4.4.2 The influence of SiCO wt.%

The capacity, the first cycle efficiency, and the hysteresis voltage were measured as a function of *Ws*, at similar values of the current density, in the range 70-90 mA g^{-1}. These plots are shown in **Fig (39, a-c)**. The weight fraction of SiCO, *Ws*, was varied from 4% to more than 50%. Interestingly, the performance parameters remain essentially independent of the weight fraction for $4\% \leq Ws \leq 8\%$; this implies that the performance is dominated by the properties of the graphite-SiCO interface rather than by the thickness of the film. The first cycle efficiency of these thin-film GF-SiCO electrodes varies from 85% to 90%; in comparison the values for bulk SiCO range from 65% to 75% [157],[151]. Likewise, the hysteresis for these thin films is only about 0.1 V whereas the values for bulk SiCO are much higher (0.75-1.25 V). These are very significant differences between bulk SiCO and thin-film GF-SiCO.

The graphs in **Fig (40)** refer to current densities of 70-90 mA g^{-1}. The capacity and the shape of the electrochemical cycles at lower and higher current densities, for *Ws* = 8.5% -10% are shown in **Fig (40)**. Most noteworthy here is that hysteresis remains low even at high currents (in bulk SiCO hysteresis becomes more severe with the higher current). Data for 10 cycles are presented here. The near-ideal overlap of the cycle shapes shows that the Coulombic efficiency is close to 100%.

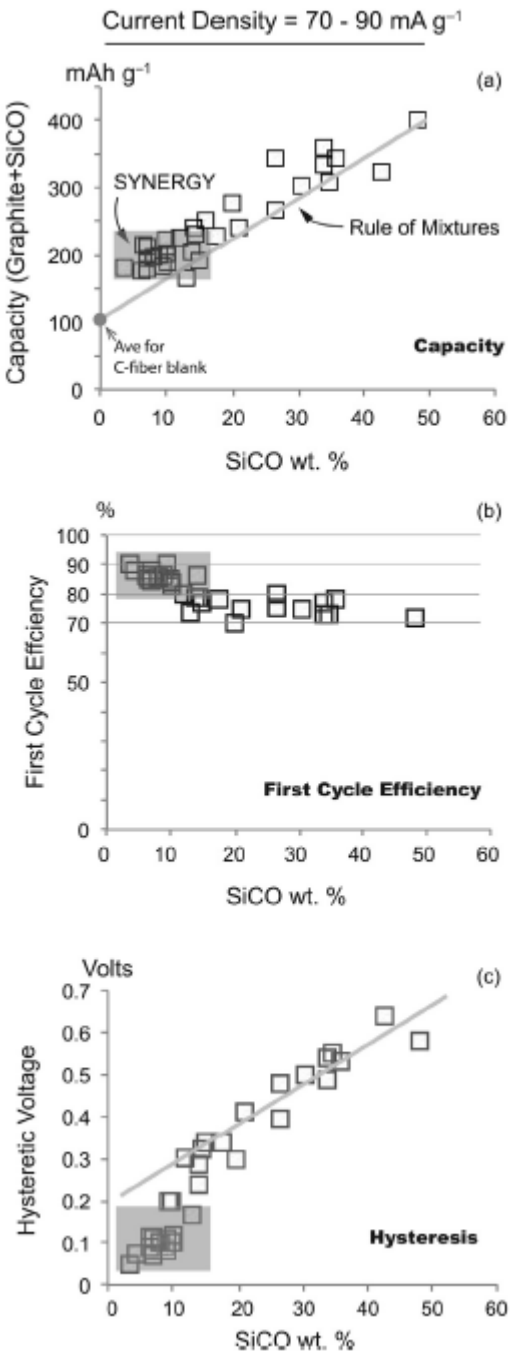

Figure 39: The influence of SiCO wt. % on (a) the capacity, (b) first cycle efficiency (b), and (c) hysteresis. Significant improvement over SiCO powder is seen for less than 12 wt%.

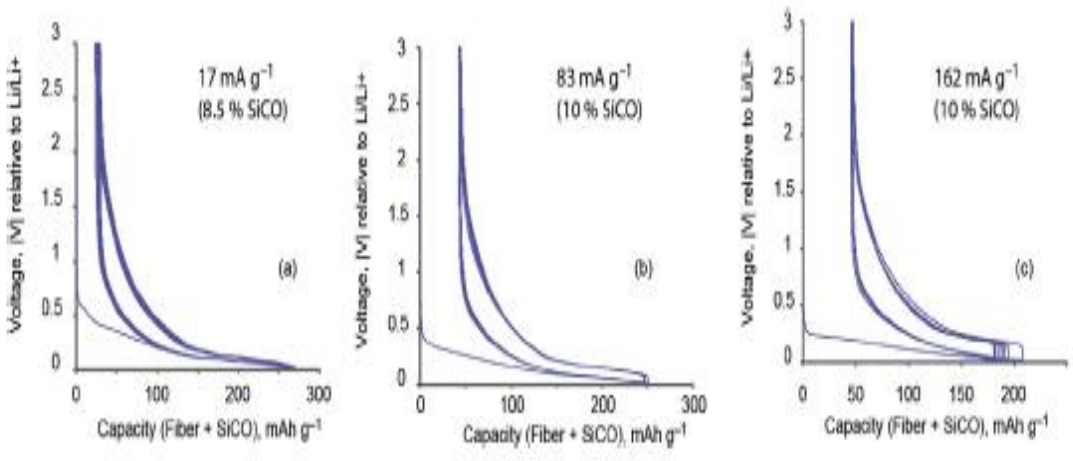

Figure 40: Influence of current density on the cyclic behavior of SiCO (~10 wt%)-GF composite anode.

4.4.3 Capacity with voltage hold at 0.01 V

The capacity of the GF-SiCO, 10%, and GF-blank were measured after holding the cell at 0.01 V until the current dropped down to negligible values. The Li was intercalated into the electrodes at a current density of 90 mA g^{-1}. The capacity of the GF blanks increased from 150 mA g^{-1} to 175 mA g^{-1}, while that of GF-SiCO increased from 230 mA $g^{-1}$to 285 mA $g^{-1}$when held at 0.01 V.

4.4.4 Thick film GF-SiCO - comparison with the bulk (powder)

Thick films are expected to approach the behavior of bulk SiCO, which is measured with powders. The results for powder-SiCO are compared with GF-SiCO (*Ws*= 48%) in **Fig (41)**. At this weight fraction, the capacity is dominated by SiCO; therefore, the capacity has been normalized with respect to the weight of the SiCO. Data for ten cycles are given. Two observations are of note. The cycles in the composite overlap nearly exactly, indicating nearly ideal coulombic efficiency; the performance of the powder anode shows some drift suggesting a slightly less than full coulombic efficiency. Second, the hysteresis in the composite is ~0.6 V as compared to nearly 1 V in the

powder-based anode. Given the high weight fraction of SiCO, these differences could not have arisen from the graphite-SiCO interface. It is likely that they arise from the morphology of the SiCO phase in the composite, which, at this high weight fraction, was in the form of a web-like structure spread continuously over the conducting fibers.

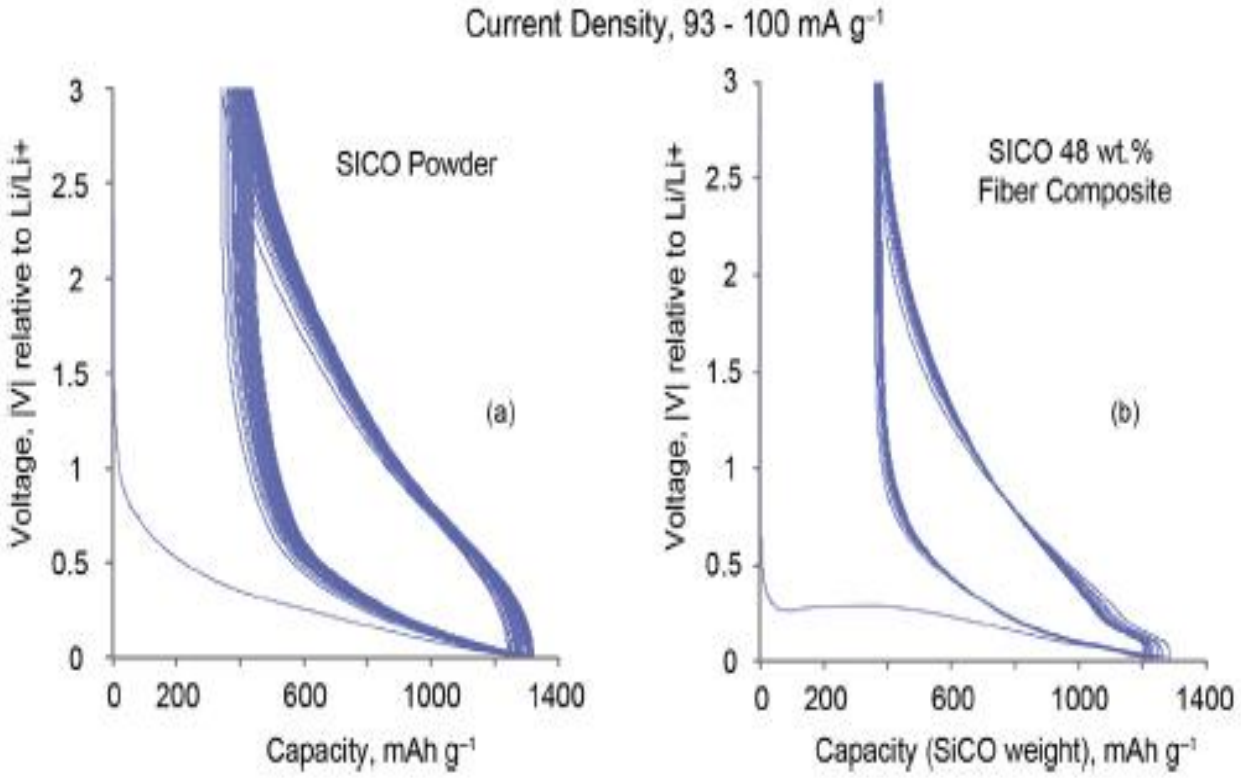

Figure 41 : (a) The cyclic behavior of SiCO powder anode made by the conventional method. (b) The cyclic behavior of a composite with 48 wt% SiCO at the same current density. The capacity has been normalized with respect to the SiCO weight. At this composition the contribution of the graphite fibers to the capacity is minor.

4.4.5 Surface area capacity in mAh cm^{-2}

Since the electrolyte permeates throughout the graphite-fiber bed, and since all fibers serve as current collectors, the integrated capacity of the GF-SiCO anodes is expected to continue to increase as the thickness of the graphite-fiber bed is increased. The implication is that the capacity expressed in terms of the surface area of the electrode can be increased to very high values,

essentially without limit. We have tested this expectation by measuring the capacity for 2, 3, 4, and 5-layer stacks of GF-SiCO anodes, each one individually is the same as used in the experiments described in the earlier figures.

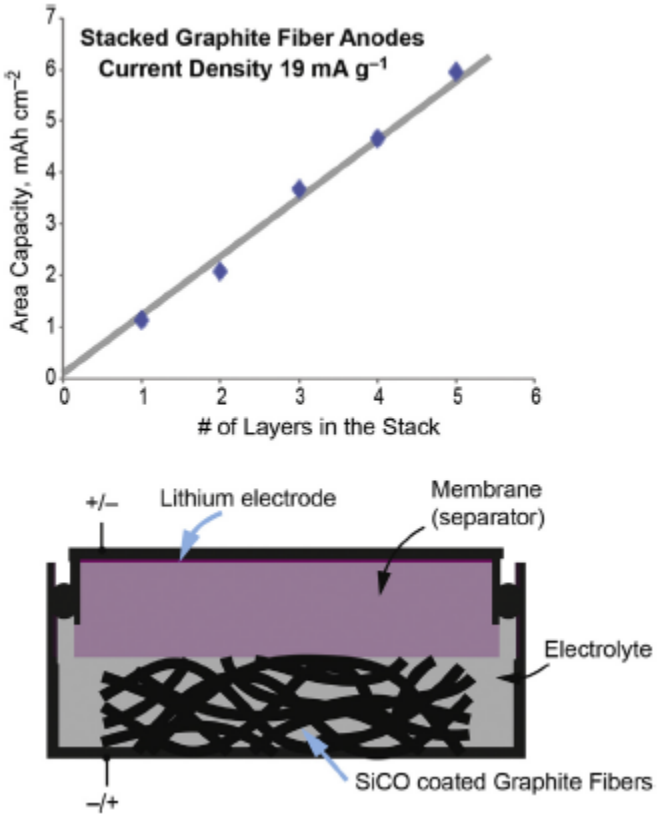

Figure 42: Since all graphite fibers are current collectors, and since the electrolyte makes contact with all of them, the thickness of the anode can be increased without limit to increase the area capacity of the anodes. This is affirmed in these data where the area capacity increases linearly with the number of layers in an anode stack.

In this instance, the capacity is expressed in terms of the surface area of the electrodes. The results are described in **Fig (42)** where the surface capacity is shown to increase linearly with the number of layers in the stack.

4.4.6 Prediction from the rule-of-mixtures

The rule-of-mixtures prediction is analyzed by combining the data from GF-blank and from bulk SiCO, that is, by assuming that the capacities of the fibers and SiCO add as if they were independent of each other. According to the rule-of-mixtures we have that.

$$q^*(\mathrm{V})=(1-Ws)q_{GF}(V) + Wsq_{SiCO}(V), \quad (36)$$

Here $q^*(\mathrm{V})$ is the gravimetric capacity of the composite, measured as a function of the voltage. Similarly, q_{GF} and q_{SiCO} are the capacities of graphite-fiber and SiCO powder at the same voltage, measured independently, at the same current density. Eq. (36) may now be applied to the entire electrochemical cycle. The results from the rule-of-mixtures, calculated from Eq. (36), are given in **Fig (43)**. The capacities for GF-blank and for SiCO powder are shown in **Fig (43, a)** and **Fig (43, b)**. The prediction from the rule-of-mixtures is compared with an experiment in **Fig (43, a)**. The measured performance is much better than predicted by the rule-of-mixtures. The first cycle efficiency is higher, as is the reversible capacity. The reduction in hysteresis is very significant.

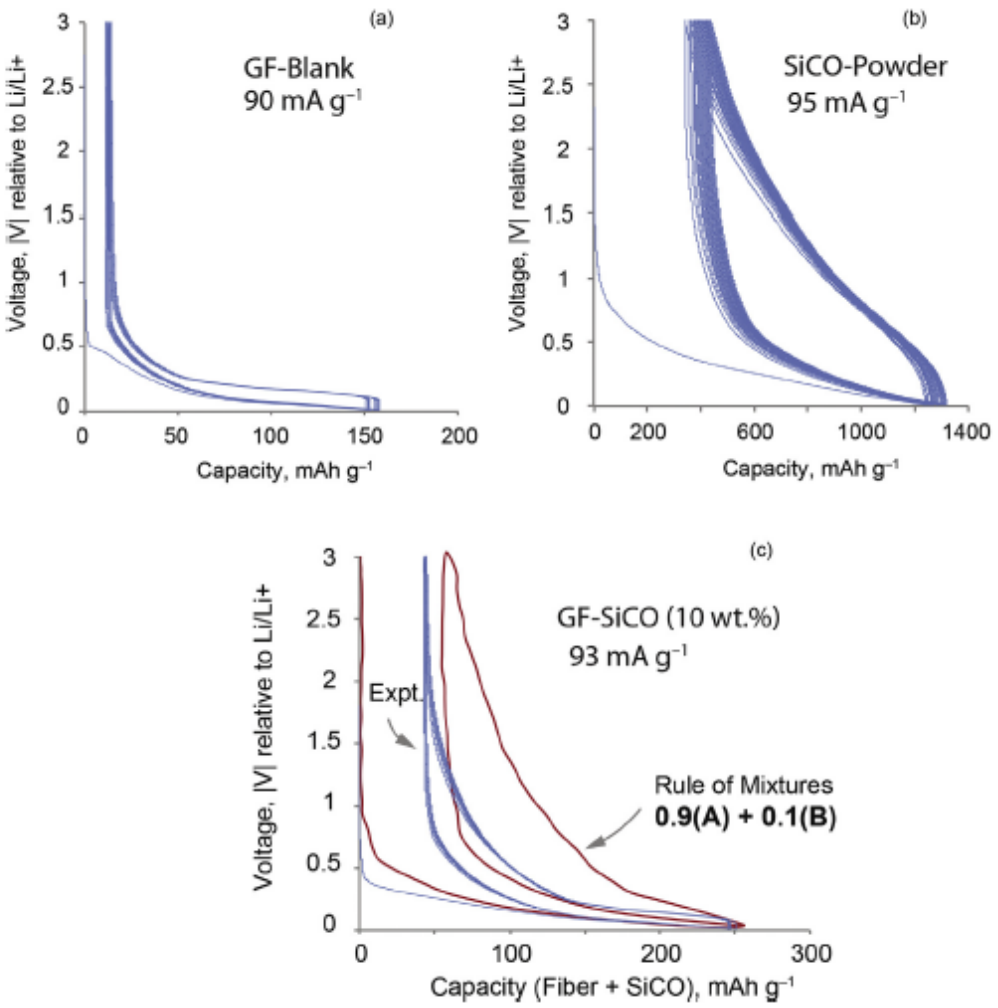

Figure 43: (a) The capacity of GF-Blank and (b) SiCO powder tested separately. (c) The capacity of the composite compared with the calculation from the rule-of-mixtures that combines the results in (a) and (b), using Eq. (36).

Discussion

In this section, we discuss the following topics: (i) the performance of the GF-SiCO thin-film architecture, ostensibly related to the nature of the graphite-SiCO interface, (ii) the design of the GF-SiCO architecture in order to enhance the gravimetric and volumetric capacities of the anodes, and (iii) manufacturability and scale-up.

The GF-SiCO interface

Bulk SiCO powders are endowed with high capacity, nearly three times that of graphite, high cyclic stability and the ability to perform at very high C-rates without failure [151], [153], [157]. However, they suffer from low first cycle efficiency (65-75%) and high hysteresis (0.75-1.25 V). As shown in **Fig (39)**, thin films of SiCO, represented by a weight fraction of less than ~8%, leading to first cycle efficiencies of 85-95% and hysteresis of less than 0.2 V. Furthermore, with these thin-films the capacity becomes essentially independent of the thickness, implying that the behavior is dominated by the graphite- SiCO interface. According to Eq. (35) these films have a thickness of 100e200 nm. These results have both scientific and technological implications. The unusual nature of these thin films is underpinned by the Raman spectra shown in **Fig(37, c)**. Bulk SiCO powders show a pattern that is similar to that of the graphite fibers with dual D and G peaks that are distinctly separated. Instead, the thin films show one, sharp G peak with broad shoulders that extend widely on either side of the peak. The pointed G peak resembles graphene. Graphene is a zero band-gap material; perhaps the electrical conductivity of these thin-films, which is necessary for electron transfer from the surface of the films to the graphite substrate, is explained by the presence of this G peak.

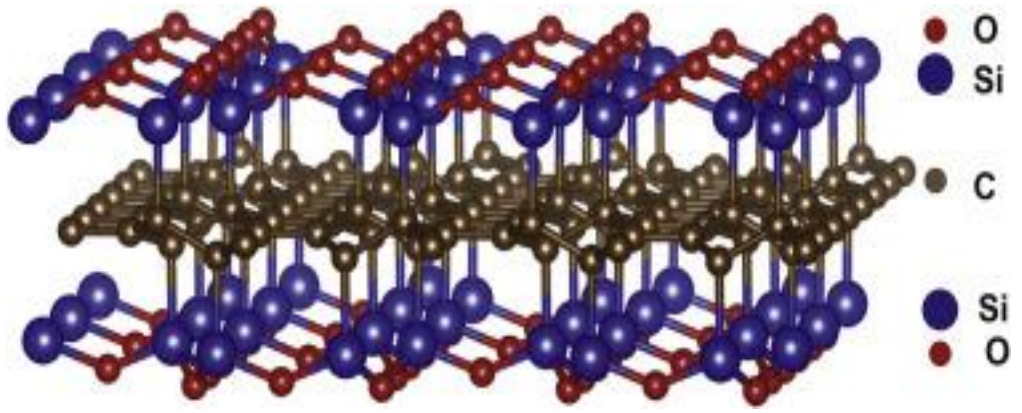

Figure 44: A 2-D crystal of monolayers of silicon on graphene with a binding energy of −1.2 eV per silicon atom. The stoichiometry of this structure is 2:4:3:Si:C:O [158].

therefore, quite conceivable that the presence of the graphite surface alters this evolution to create a different structure. Secondly, recent first-principle calculations of the structure of SiCO have predicted a low-energy 2D structure shown in **Fig (44)**. This structure has a very high density of mixed-bonds between C-Si-O, which are known to sequester large amounts of Li. It can be postulated that these 2D layers begin to form on the graphite surface, to some extent, and continue to form until the films gets quite thick.

Design considerations: gravimetric and volumetric capacity

The SiCO thin-film on the graphite-fiber architecture of the anodes offers new design and materials selection opportunities to enhance their performance. The fibers in the present experiments, which have been developed for fiber-reinforced polymer composites, have only one third the capacity of the state-of-the-art graphite-powders used in Li-ion batteries. It is well known that carbon made from different sources has widely different capacity for Li[159].

The selection of the precursors of SiCO is likely already optimized in view of the experiments on materials with a wide range of chemistries. However, the relationship between precursor chemistry and the growth of thin films on graphite substrates is not known.

The most obvious benefits are likely to come from the geometrical design of the anode architecture, which has two main elements, the fiber diameter, *d*, and the packing density of fibers in the mesh, *f*. The film thickness should also be considered, but, in view of the results presented here, we shall assume that the films are thin so that the capacity is controlled essentially by the interface; this is rather a strong assumption and, therefore, the approximate nature of the analysis below must be kept in mind. The assumption simplifies the analysis considerably, since now the capacity is proportional to the surface area in the composite measured as a function of the weight, or the volume.

The gravimetric surface area is written by the well-recognized parameter, SSA, or the specific surface area, commonly expressed in units of $m^2\ g^{-1}$. For fibers, it can be immediately written that

$$SSA = 4/d\rho g \tag{37}$$

Using the form of Eq. (36) we may then write that

$$q^* = \pi\frac{d^2}{4}\ \rho g\ q_{GF} + (\frac{4}{d\rho g})\sigma_{SiCO} \tag{38}$$

where σ_{SiCO} is the capacity of the film per unit area of the film, with units of $mAhm^{-2}$. Note that the term is the brackets represents *SSA*. Inspection of Eq. 38 shows that smaller values of *d* would make the second term larger than the first. If we assume that the second term is dominant then a two-fold reduction in fiber diameter would lead to a two-fold increase in the capacity of the

composite, and so on. The volumetric capacity of the composite, Φ*, expressed in mAh cm^{-3} is given by a simple transformation of Eq. (38) by converting the weight into the volume

$$\Phi^* = f \rho_g q^* \tag{39}$$

where *f* is the packing factor (=0.2 in the present experiments). Note that in Eq. (39) q* is in units of mAh g^{-1}, and ρ_g in units of g cm^{-3}. Finally, we compared the present results to the case of a standard electrode made from 10 mm thick copper foil coated on both sides with 44 mm thick graphite powder as the active material; in this case the area capacity (of the total anode) is estimated to be 3.5 mA cm^{-2}, the gravimetric capacity as 150 mAh g^{-1}, and the volumetric capacity as 350 mAh cm^{-3}. In the present anodes, the gravimetric capacity of about 240 mAh g^{-1} exceeds this benchmark.

However, the volumetric capacity of the present electrodes is a factor of three to four lower. The packing density of the current fiber paper was 20%. It can be increased by a factor of three. Furthermore, graphite fibers of a smaller diameter would increase the gravimetric capacity, which from Eq. (29), immediately translates into a higher volumetric capacity, as well.

Manufacturability and scale-up

The simplicity of one-step processing of the SiCO-on-fiber anode, which can be immediately inserted into the battery, is notable. The anode is mechanically resilient e it bends without fracture e and can be stored in air. The additive manufacturing approach, described in Ref [21]is already being developed to deposit thin films of controlled thicknesses on the nanoscale on graphite-fiber substrates. Two special features of this approach are (i) the liquid precursor solution spreads throughout the fiber mesh because of its wetting behavior, and (ii) the ultra-thin films of the

polymer can be pyrolyzed in just a few seconds without forming defects. The scale-up of this approach for coating large sheets of graphite paper is under consideration [155].

4.5 Summary

(i) Thin films of SiCO, which is a candidate material for anodes, are deposited as continuous layers on the surfaces of graphite fibers, where the fibers serve the dual function of the current collector. The liquid electrolyte permeates through the entire thickness of the fiber-mesh providing an intimate, large area interface for the electrochemical reaction. expectedly, the films are apparently electrically conducting for the transfer of electrons from the surface of SiCO to the graphite substrate lying underneath.

(ii) Raman spectra show that thin films have a different structure than bulk SiCO. They show a sharp G peak similar to graphene. The D peak, seen in bulk SiCO, is replaced by broad shoulders on either side of the G peak. First-principle calculations suggest the possibility of two-dimensional structures where a layer of Si and O atoms covers a sheet of graphene [158], shown in **Fig (44)**. It is possible that the growth of SiCO on graphite from polymer precursors invokes structures of this kind. Films that range in thickness from 100 to 200 nm yield capacities that are essentially independent of the film thickness (see **Fig (39)**), suggesting a strong role of the interface structure in electrochemical performance.

(iii) The thin-film architecture consistently shows much higher first cycle efficiency (85-90%) and lower hysteresis (0.1- 0.2 V), than bulk SiCO. The equivalent values for bulk SiCO are 65-75% and 0.75-1.5 V.

(iv) The one-step manufacturing of the anodes can be cost-effective and conducive to scale-up [155]. The anodes are mechanically resilient and can be stored in air. Additive manufacturing of

the composites is facilitated by the wetting behavior of the polymer precursor and “flash pyrolysis” for its conversion into SiCO.

(v) Eqs. (38) and (39) provide guidelines for increasing the gravimetric and volumetric capacity by reducing the fiber diameter and increasing the packing density in the fabric.

Chapter 5

5 TiO_2 nanotube as chemical and gas sensor

5.1 Introduction

In our daily life, we use different kinds of sensors that detect and respond to electrical or optical signals. Their applications include daily monitoring of hazardous gases, air quality, real-time gas monitoring, and human disease detection via analyzing the human exhaled breath (biosensors). Recently, nanostructures of wide bandgap semiconductors metal oxide-based gas sensors have attracted significant attention owing to their excellent high sensitivity, good response time, portability , relatively low synthesis cost TiO_2[160], SnO_2[161], WO_3[162], ZnO[163] and In_2O_3[164]. Among them, TiO_2 nanostructures gas sensors have received considerable attention due to effective sensing of certain gases such as H_2[165], [166],[167]. These nanotube structures are attractive due to their large surface, more gas adsorption sites, inert surface properties, and high sensitivity.

In this work, our goal is to fabricate and characterize doped and undoped TiO_2 nanotube gas sensor that can quickly detect a low concentration of different chemical and target gases, usually gases that have unwanted effect when exceeds a certain limit. To achieve this goal, the TiO_2 metal oxide nanotube structure was synthesized and doped with different anion and/or cation dopants by using the electrochemical anodization technique. Also, the fabricated nanotubes gas sensor in this work will operate at ambient room temperature.

5.2 Experimental setup

The preparation of the doped and undoped TiO_2 nanotube has been demonstrated in detail in chapter 2. Briefly, the Ti sheet was first was cut into 20x30 mm followed by ultrasonic cleaning in acetone, ethanol, methanol and DI water for 10 min each. The sample was then anodized in ethylene glycol electrolyte containing 2 wt% DI water 0.5wt% ammonium fluoride at 40 V for 4hours. The anion and/or the cation doping samples were prepared by adding a small percent of

the anion precursor in the anodization electrolyte and switching the polarity in the cation doping electrolyte. The samples were immersed in ethanol for 15 minutes and rinsed with DI then dried with N_2 stream. The fabricated nanotubes were heat-treated at 550°C for 2 h in the air in order to transform the amorphous phase to the crystalline phase.

Characterization

A field-emission scanning electron microscope (TESCAN MIRA3 LMH Schottky) was used to study the surface morphologies of the TiO2 nanotubes. The elemental composition was obtained by energy-dispersive X-ray spectroscopy.

Chemical sensing measurement

The gas sensing properties of the doped and undoped TiO_2 nanotube were obtained by introducing different chemicals, reducing and oxidative gases with different concentration into vacuum chamber contain different doped and undoped TiO_2 nanotube sensors samples connected to the power source through electrical feedthrough. The chamber was pumped down to approximately 1 mToor by using both a rotary vane vacuum pump and Turbo vacuum pump. The pressure was increased gradually, using the needle valve, up to the saturation pressure of each chemical and to the ambient pressure of the gases. The pressure and gas concentration inside the chamber were measured by three different pressure gauges. A schematic of the experimental setup is shown in **Fig (45)**. The current-Voltage measurement was done by sweeping the voltage and measure the current by using a Keithley source meter (Keithley 2612A, Tektronix Inc.). The positive bias was connected to the nanotube and the negative bias to the Ti metal.

The gas concentration was measured by the following equation;

$$Gas\ Concentration(ppm) = (\frac{\text{measured pressure(Torr)}}{760})* 10^6. \quad (40)$$

Also, the sensor response was measured by the following equation;

$$\Delta I = \left(\frac{Ig-Iv}{Iv}\right) * 100. \quad (41)$$

Here, *Ig* is the sensor current in the presence of the target gases or chemical and *Iv* id the sensor current in Vacuum which is about 35mTorr.

The sensitivity can be obtained by calculating the slope of the calibration which is the sensor response vs the concentration.

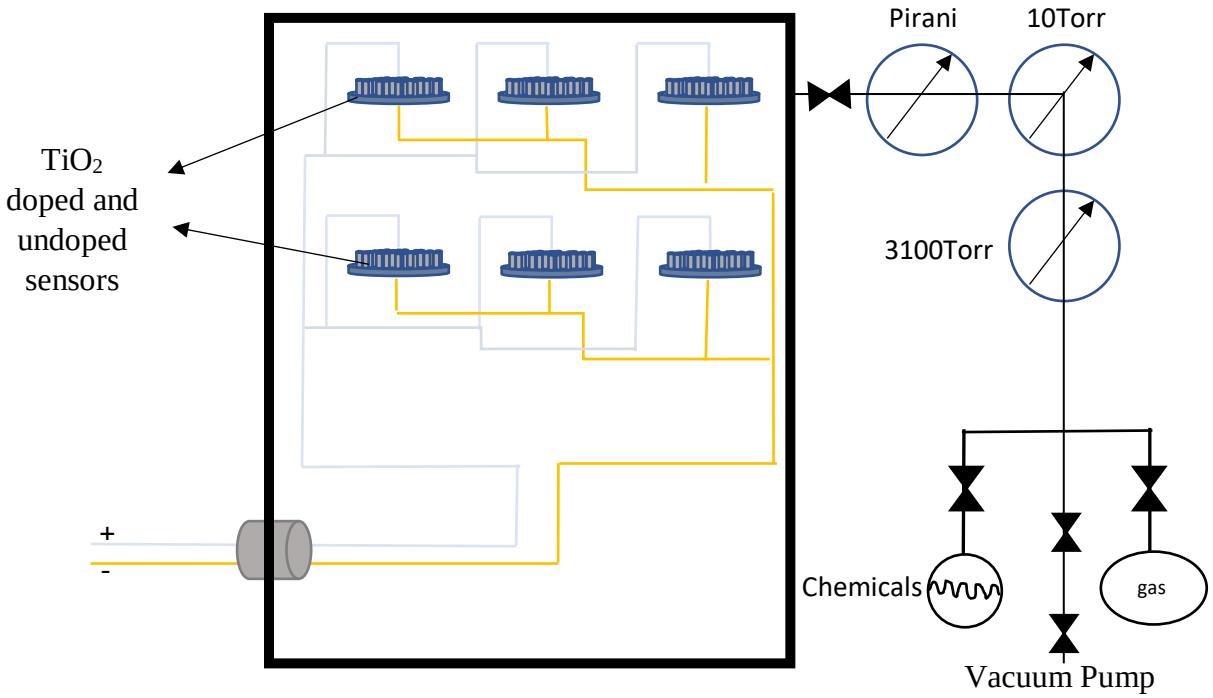

Figure 45: Schematic of the experimental setup used during gas sensitivity measurements.

The sensed chemicals were water, acetone, ethanol, and methanol. Table11 shows the partial pressure of the chemicals at ambient temperature 25ºC and humidity ~55%.

Table 11:Partial pressure and chemical formula for the sensed chemicals.

Analyte	Chemical formula	Partial pressure (Torr) at 25^0C
Water	H_2O	20
Acetone	$(CH_3)_2$ CO	197
Ethanol	C_2H_5OH	47
Methanol	CH_3OH	97

Gas sensing measurement

The gas sensing measurements of carbon monoxide were done in a flow-type homemade chamber sensor test system. The TiO_2 CO sensing was evaluated by controlling the flow rate of the gas mixture (CO&dry air) by using the mass flow controllers connected to high purity dry air tank in order to eliminate the effect humidity in ambient air and dilute the dangerous CO gas.

5.3 Result and discussion

Field emission scanning electron microscopy (FESEM) morphology of Niobium doped TiO_2 nanotube is shown in **Fig (46).** The SEM picture revealed that the nanotube diameter ranging from 80 to 100nm and the wall thickness is ranging from 5 to 8 nm. The length of the nanotube mainly depends on the anodization time and according to previous work[21], the length should be about 16µm when the anodization lasts 4 hours.

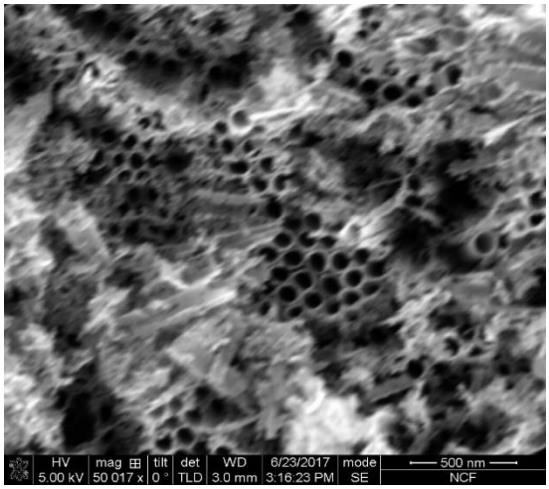

Figure 46: Scanning electron micrographs (SEMs) of the top view of niobium doped TiO_2 nanotube grown by electrochemical anodization.

The energy dispersive X-ray microanalysis (EDX) of niobium doped TiO_2 nanotube was obtained in the binding energy range from 0 to 10keV. The peak of the spectrum confirms the existence of niobium doping in the TiO_2 nanotube **Fig (47).**

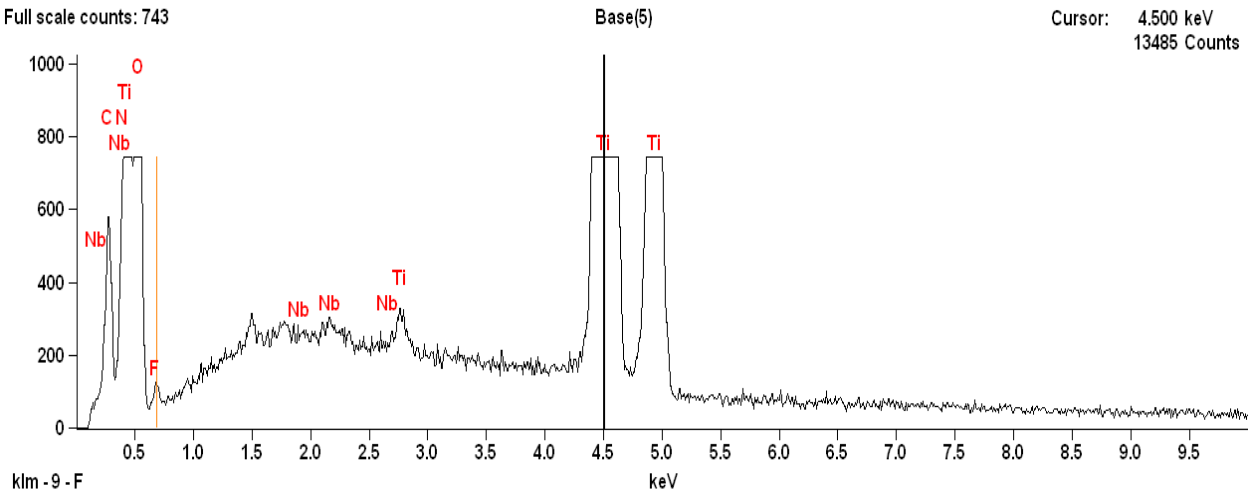

Figure 47: EDX analysis of Nb-doped TiO2 nanotubes.

TiO_2 sensing mechanism

The metal oxide, TiO_2 nanotube, sensing mechanism is still under debate, but there is a general agreement that the detection mechanism depends on the change in the electronic properties of the TiO_2 nanotube and this change can be explained by surface/depletion model[167]–[170]. This model suggests, that the reaction between the TiO_2 nanotube's oxygen vacancies and adsorbed reducing gases leads to change in the electrical resistivity of the TiO_2 nanotube. The as-prepared TiO_2 has an excess of electrons due to the formation of the oxygen vacancies (missing oxygen atoms in the TiO_2 crystal structure) which function as electron's donor. These vacancies can be created by sputtering, electron bombardment or by high-temperature heat treatment of the metal oxide surface in vacuum or in reducing atmosphere such as argon and N_2 gas. The presence of oxygen vacancies was confirmed by scanning tunneling spectroscopy (STS) used in our previous work [21]. The results showed that the Fermi level of the samples has been shifted toward the conduction band confirming the n-type conductivity of TiO_2 nanotube with the free electron as charge carriers.

Here, when the oxygen molecule at high temperature adsorbs on the TiO_2 surface, it captures the available free electron from the TiO_2 conduction band due to the fact that the lower edge of the TiO_2 conduction band (4.3 eV) is higher than the oxygen chemical potential (5.7 eV) on the vacuum level scale. As the electrons depleted from the TiO_2 surface, a thin depletion layer will be developed on the TiO_2 surface accompanied with very strong electrical field **Fig (48)**.

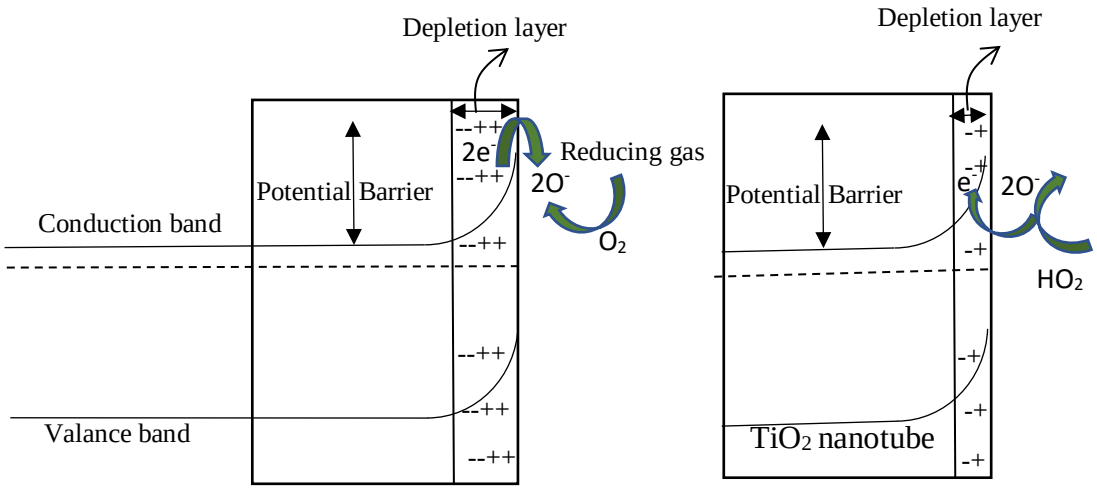

Figure 48**:** Schematic diagram of band bending and gas reaction of a TiO2 nanotubes-based sensor.

Undoped and doped TiO_2 nanotube chemicals sensing

The current-voltage measurements revealed that TiO_2 nanotube has the electrical-chemical gating behavior, especially for water, which was explained in details in previous work[168]. For example, the current has increased by approximately two orders of magnitude at 2V when the concentration of the water molecules inside the vacuum chamber was gradually increased (from 30 mTorr to 4Torr) **Fig (49)**. However, doping TiO_2 nanotube with anion dopant could possibly affect the nanotube sensing performance. For instance, the nitrogen-doped TiO_2 nanotube showed no response to different chemicals probably due to quenching the conduction band electron **Fig (50).** On the other hand, the carbon-doped sample showed better sensing performance probably due to the increase of the oxygen vacancies **Fig (51).** Doping with cation dopant such as niobium can also affect sensing performance. The I-V characteristics of Nb-doped sample with different water concentrations are shown in **Fig (52).**

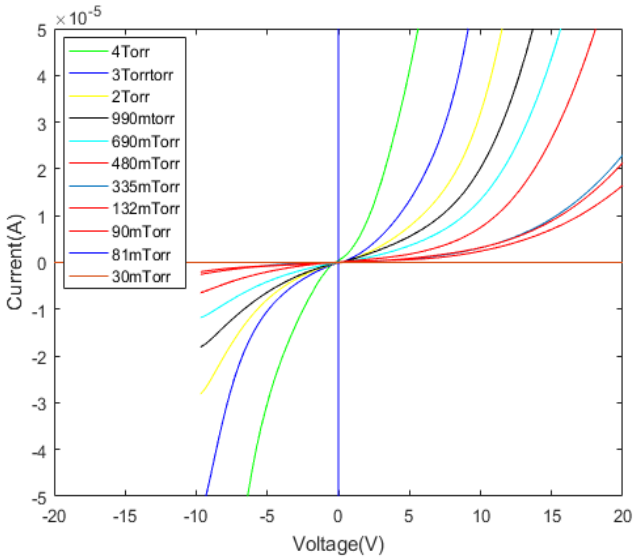

Figure 49: Characteristics of undoped TiO_2 at different water concentration.

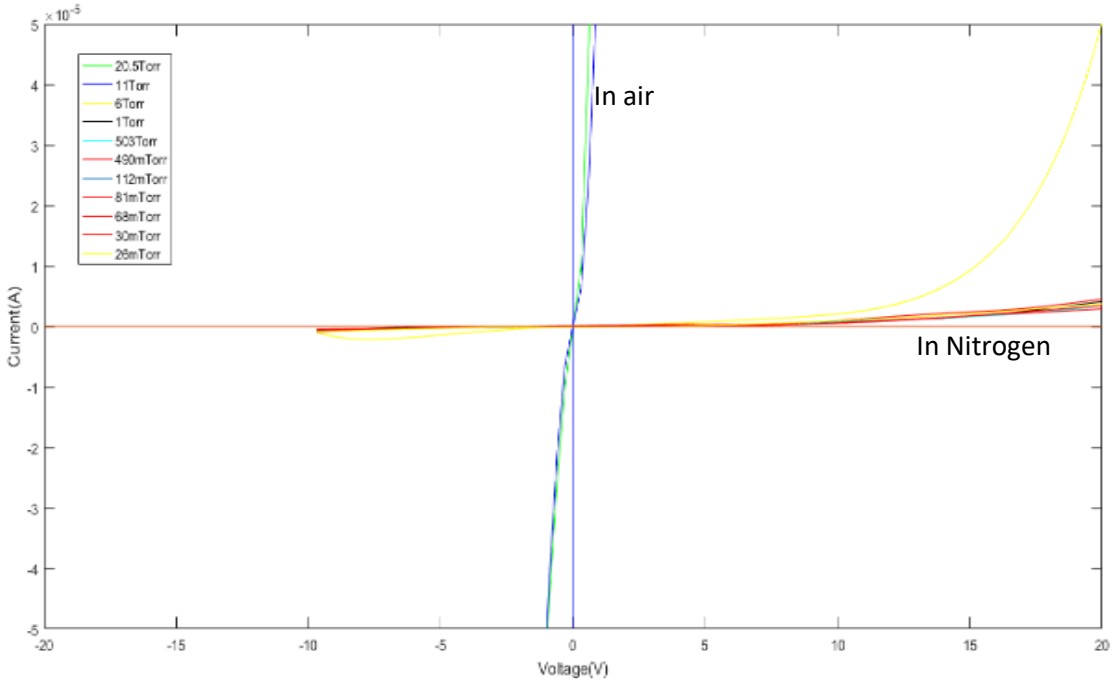

Figure 50: I–V characteristics of nitrogen-doped TiO_2 nanotubes different water concentration.

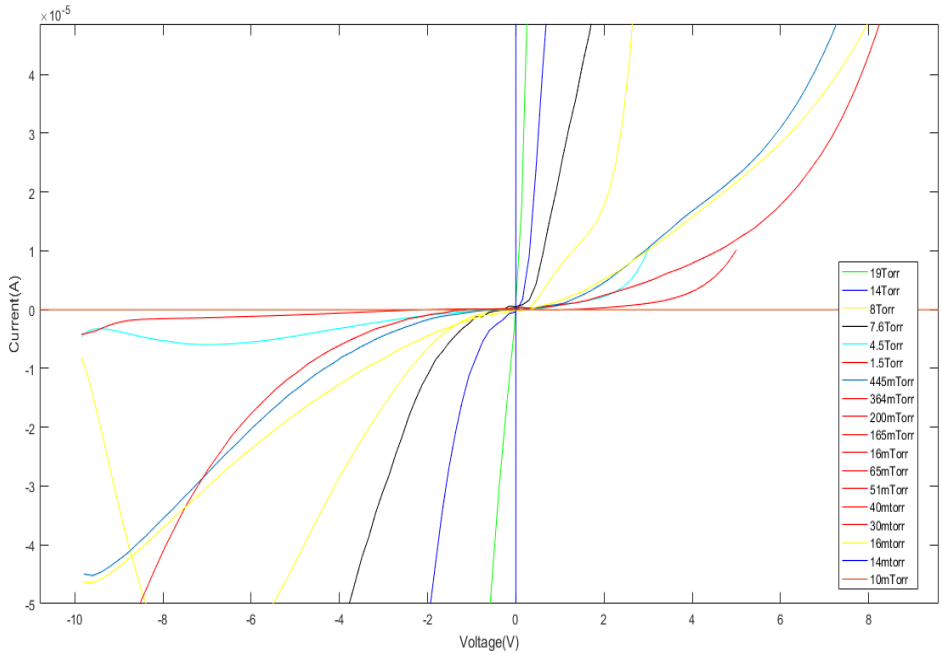

Figure 51: I–V characteristics of carbon-doped TiO_2 different water concentration.

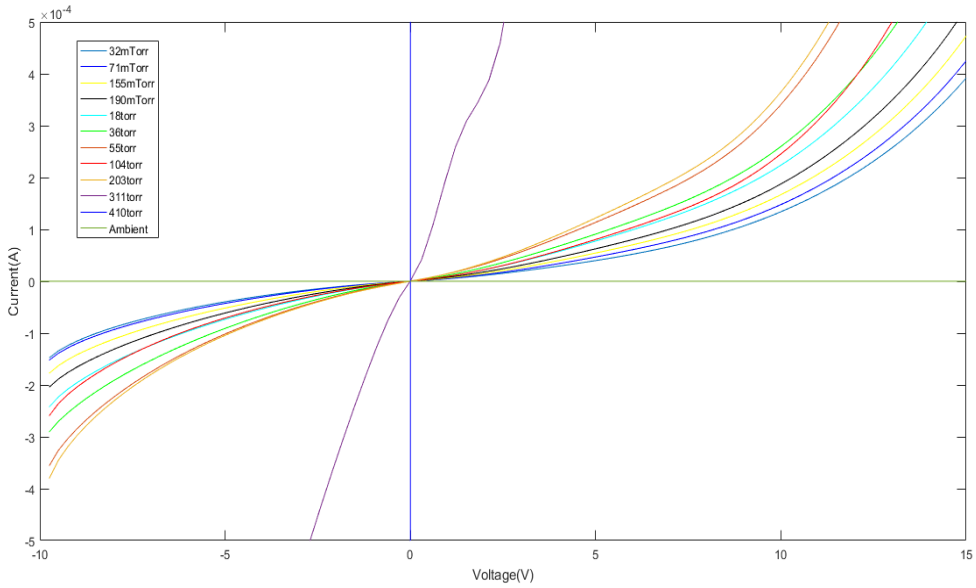

Figure 52: I–V characteristics of Niobium-doped TiO_2 different water concentration.

Undoped and doped TiO_2 nanotube gas sensing

To understand the sensitivity of the TiO_2 nanotube toward gases, doped and undoped nanotubes were prepared for sensing different conventional gases**.** It was noticed that gases such as oxygen and nitrogen have no appreciable effect on the electrical properties of TiO2 nanotubes at room temperature. The I-V electrical response of the TiO_2 nanotube to varying concentrations of nitric oxides, reducing gas, with fixed water concentration is shown in **Fig (53)**. Without water, the sensor shows no response. One can see that there is an increase in the electrical resistance upon exposure to different concertation of NO at room temperature. The electrical resistance of NO gas has decreased due to the fact that NO function as electron acceptor decreasing the electron concertation in the conduction band as well as increasing the depletion layer width.

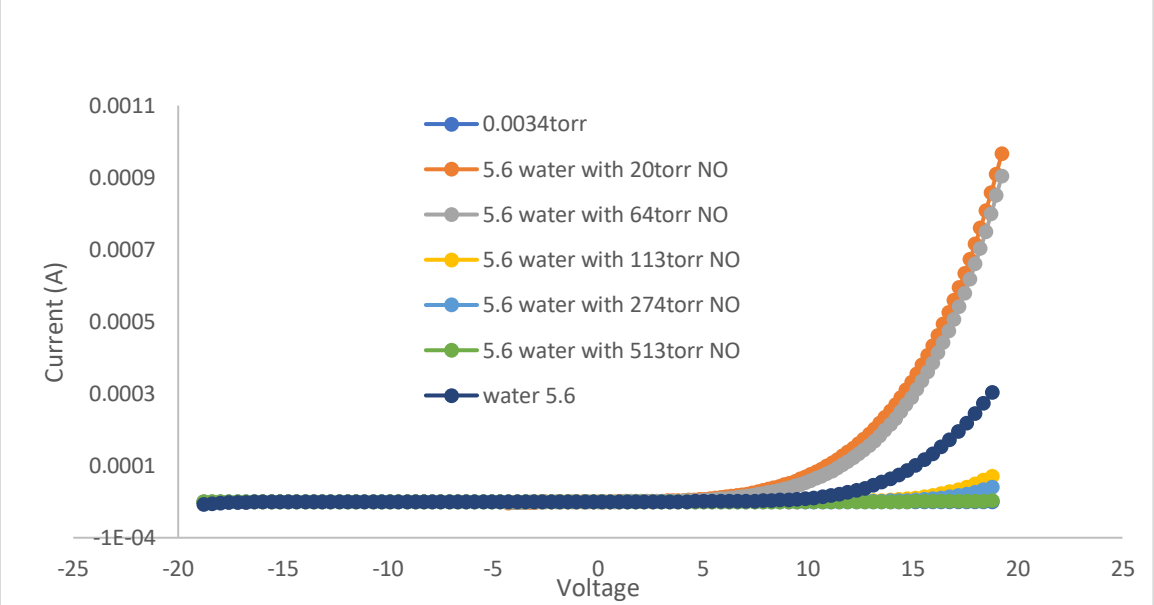

Figure 53: I-V electrical response of the TiO_2 nanotube to varying concentrations of nitric oxides with fixed water concentration at room temperature.

Also, undoped TiO_2 respond to carbon monoxide, an oxidizing gas, was negligible owing to the strongly charge-depleted nanotube surface. However, the electrical response of niobium doped TiO_2 nanotube samples to varying concentrations of carbon monoxide, an oxidizing gas, showed an increase in the electrical resistivity **Fig (54).**

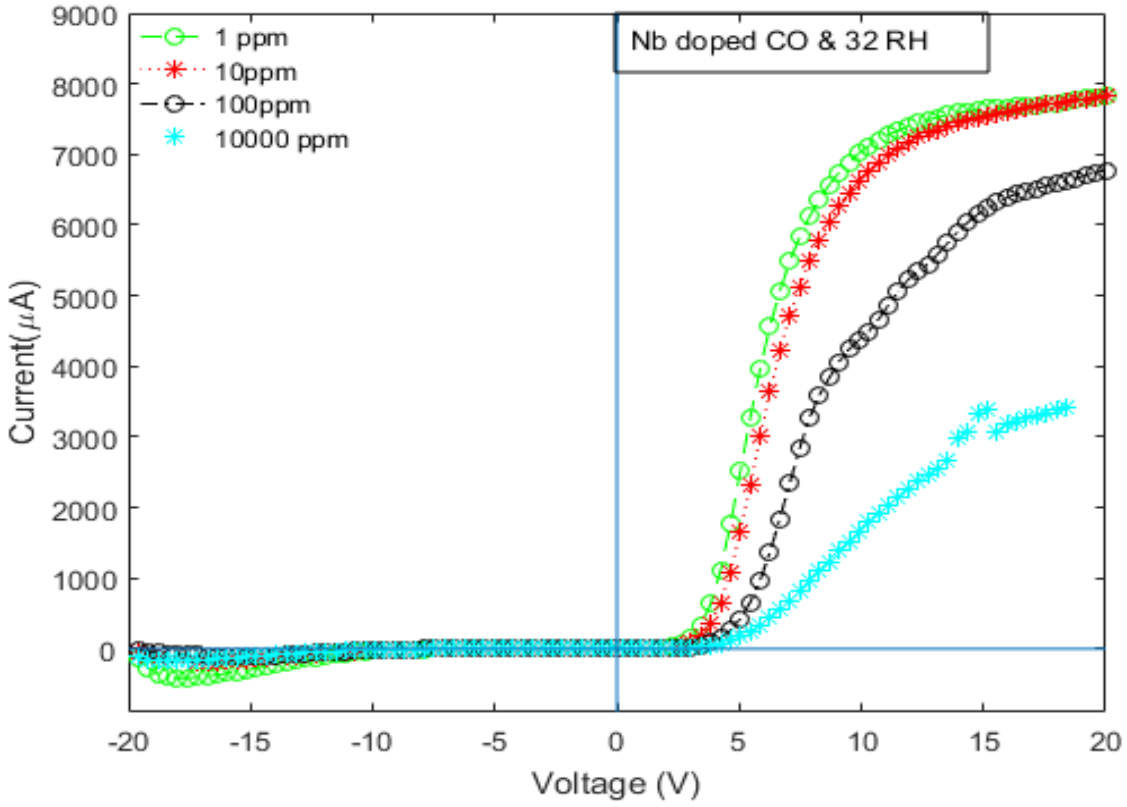

Figure 54: I-V electrical response of the Nb-doped TiO_2 nanotube to varying concentrations of Carbon monoxide with fixed water concentration at room temperature.

Undoped and doped TiO_2 nanotube multianalyte gas sensing

To further exploit these tunable electronic properties of co-doped TiO_2 nanotubes, we evaluated their potential for multianalyte gas sensing. While we had previously demonstrated strong sensing signal for different chemical analytes using undoped nanotubes, primarily using the tunable depletion width and concept of chemical gating undoped nanotubes,[78], [79] these analytes

cannot be detected as mixtures given the fixed sensitivity of undoped nanotubes for each analyte. In order to utilize the tunable electronic properties of nanotubes via doping and tune the sensitivity of different gas analytes as a portable multianalyte sensor, we tested different doped and co-doped nanotube response to small partial pressures of these analytes **Fig (55).** Using same analytes with multiple doped and co-doped nanotubes mounted together as a portable device, we observed that doping could modulate the depletion width and hence the sensitivity of the nanotubes for the same analyte (acetone here, **Fig (55, b)**. Further, the sensitivity of each nanotube was different for the different analyte **Fig (55, c)**, demonstrating their potential as a potable multianalyte chemical sensor (for example, for human breath sensing). Using the varying sensitivity of 5 different analytes with 5 different undoped and co-doped nanotubes as a calibration matrix (matrix **S Fig (55, d)**, we can easily detect their respective concentrations using electronic readout/current output simultaneously from the five detectors (Concentrations $\mathbf{C} = \ln \mathbf{I} \times \mathbf{S}^{-1}$). Therefore, the real-time output from portable doped and co-doped nanotubes sensors can allow a real-time output of different chemical concentrations, using a stable background signal with time compared to thin-film sensors where the nanoparticle or grain size changes with time leading to changing sensitivity and baseline current. Further, the high chemical stability, large surface-area-to-volume ratio, and portable, inexpensive, standalone nanotube membranes can be an ideal alternative for traditional thin-film sensing applications.

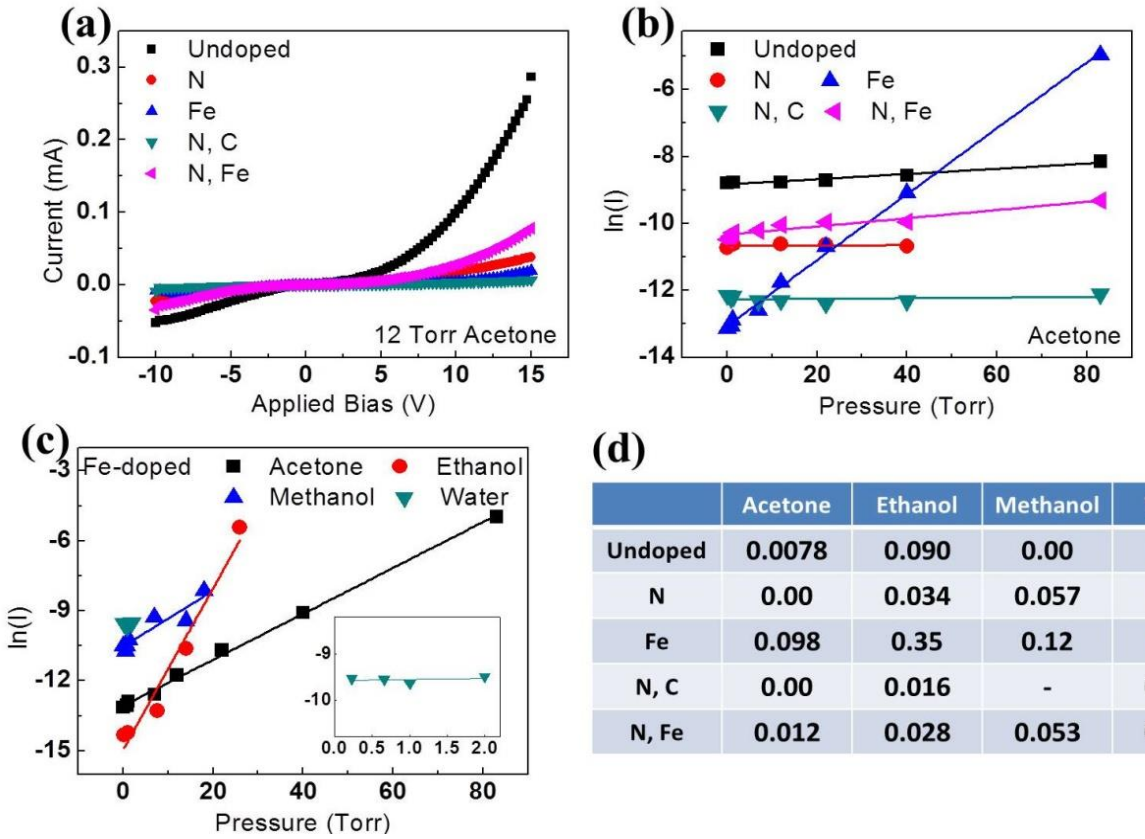

	Acetone	Ethanol	Methanol	Water
Undoped	0.0078	0.090	0.00	0.26
N	0.00	0.034	0.057	0.14
Fe	0.098	0.35	0.12	0.00
N, C	0.00	0.016	-	0.013
N, Fe	0.012	0.028	0.053	0.033

Figure 55**:** Using nanotubes as gas/vapor sensors, showing (a) the I~V curve of the nanotubes with 12 torr acetone vapor; (b) The pressure-dependent current change (represented as ln(I)~pressure plot, with 12 V applied bias under acetone vapor); (c) The pressure-dependent current change (with 12 V applied bias) with Fe-doped nanotubes for different analyte sensing; (d) The extracted sensing coefficient (matrix **S**) with different nanotube/analyte combinations.

5.4 Conclusion

In summary, we have demonstrated that the detection sensitivity of the hollow semiconductor TiO_2 nanotube with a large surface area could be increased by mono-doping and co-doping with anion or/and cation elements. The undoped and doped sample showed good sensitivity to several chemicals such as water, acetone, ethanol, methanol, nitric oxide, and carbon monoxide. Also, the sensitivity of TiO_2 nanotube toward gases such as CO increases when doped with cation dopant. These results highlight the potential for the development of a new class of metal oxide sensor can be used multianalyte detection in human breath or air-quality monitoring.

References

[1] UN DESA, "World population projected to reach 9.8 billion in 2050, and 11.2 billion in 2100 | UN DESA | United Nations Department of Economic and Social Affairs," *un.org*, 2017. [Online]. Available: https://www.un.org/development/desa/en/news/population/world-population-prospects-2017.html. [Accessed: 29-Mar-2019].

[2] C. F. Shih, T. Zhang, J. Li, and C. Bai, "Powering the Future with Liquid Sunshine," *Joule*, vol. 2, no. 10, pp. 1925–1949, 2018.

[3] EPA, "Global Greenhouse Gas Emissions by Gas Trends in Global Emissions," vol. 2000, no. 2007, pp. 2007–2009, 2014.

[4] S. Y. Lee and S. J. Park, "TiO2 photocatalyst for water treatment applications," *Journal of Industrial and Engineering Chemistry*, vol. 19, no. 6, pp. 1761–1769, 2013.

[5] L. Zhong and F. Haghighat, "Photocatalytic air cleaners and materials technologies - Abilities and limitations," *Building and Environment*, vol. 91, pp. 191–203, 2015.

[6] J. C. Yu, W. Ho, J. Lin, H. Yip, and P. K. Wong, "Photocatalytic activity, antibacterial effect, and photoinduced hydrophilicity of TiO2 films coated on a stainless steel substrate," *Environmental Science and Technology*, vol. 37, no. 10, pp. 2296–2301, 2003.

[7] Y. Ding and P. Nagpal, "Standalone anion- and co-doped titanium dioxide nanotubes for photocatalytic and photoelectrochemical solar-to-fuel conversion," *Nanoscale*, vol. 8, no. 40, pp. 17496–17505, 2016.

[8] P. Wang, Y. Bai, J. Bisquert, I. Mora-Seró, and F. De Angelis, "Titanium Dioxide Nanomaterials for Photovoltaic Applications," *Chemical Reviews*, vol. 114, no. 19, pp. 10095–10130, 2014.

[9] K. Nakata and A. Fujishima, "TiO 2 photocatalysis: Design and applications," *Journal of*

Photochemistry and Photobiology C: Photochemistry Reviews, vol. 13, no. 3, pp. 169–189, 2012.

[10] K. Fujishima, A., & Honda, "Electrochemical Photolysis of Water One and Two-dimensional Structure of Poly (L-Alanine) shown by Specific Heat Measurements at Low," *Nature*, vol. 238, pp. 37–38, 1972.

[11] X. Kang, S. Liu, Z. Dai, Y. He, X. Song, and Z. Tan, *Titanium Dioxide: From Engineering to Applications*, vol. 9, no. 2. 2019.

[12] V. I. Lakshmanan, A. Bhowmick, and M. A. Halim, "Titanium dioxide: Production, Properties, and Applications," *Chemical Physics Research Journal*, vol. 7, no. 1, pp. 1935–2492, 2014.

[13] D. A. H. Hanaor and C. C. Sorrell, "Review of the anatase to rutile phase transformation," *Journal of Materials Science*, vol. 46, no. 4, pp. 855–874, 2011.

[14] S. J. Smith *et al.*, "Heat capacities and thermodynamic functions of TiO2 anatase and rutile: Analysis of phase stability," *American Mineralogist*, vol. 94, no. 2–3, pp. 236–243, 2009.

[15] J. E. S. Haggerty *et al.*, "High-fraction brookite films from amorphous precursors," *Scientific Reports*, vol. 7, no. 1, pp. 1–11, 2017.

[16] Y. C. Nah, I. Paramasivam, and P. Schmuki, "Doped TiO2 and TiO2 nanotubes: Synthesis and applications," *ChemPhysChem*, vol. 11, no. 13, pp. 2698–2713, 2010.

[17] V. Galstyan, E. Comini, G. Faglia, and G. Sberveglieri, "TiO2 nanotubes: Recent advances in synthesis and gas sensing properties," *Sensors (Switzerland)*, vol. 13, no. 11, pp. 14813–14838, 2013.

[18] J. Wang, Q. Xie, Q. Meng, X. Li, and H. Dong, "Water splitting on TiO2 nanotube arrays," *Catalysis Today*, vol. 165, no. 1, pp. 145–149, 2011.

[19] K. C. Sun, M. B. Qadir, and S. H. Jeong, "Hydrothermal synthesis of TiO2 nanotubes and their application as an over-layer for dye-sensitized solar cells," *RSC Advances*, vol. 4, no. 44, pp. 23223–23230, 2014.

[20] T. Maiyalagan, B. Viswanathan, and U. V. Varadaraju, "Fabrication and characterization of uniform TiO2 nanotube arrays by sol-gel template method," *Bulletin of Materials Science*, vol. 29, no. 7, pp. 705–708, 2006.

[21] Y. Alivov, V. Singh, Y. Ding, L. J. Cerkovnik, and P. Nagpal, "Doping of wide-bandgap titanium-dioxide nanotubes: Optical, electronic and magnetic properties," *Nanoscale*, vol. 6, no. 18, pp. 10839–10849, 2014.

[22] K. Indira, U. K. Mudali, T. Nishimura, and N. Rajendran, "A Review on TiO2 Nanotubes: Influence of Anodization Parameters, Formation Mechanism, Properties, Corrosion Behavior, and Biomedical Applications," *Journal of Bio- and Tribo-Corrosion*, vol. 1, no. 4, pp. 1–22, 2015.

[23] D. Regonini, C. R. Bowen, A. Jaroenworaluck, and R. Stevens, "A review of growth mechanism, structure and crystallinity of anodized TiO2 nanotubes," *Materials Science and Engineering R: Reports*, vol. 74, no. 12, pp. 377–406, 2013.

[24] D. Khudhair *et al.*, "Anodization parameters influencing the morphology and electrical properties of TiO2 nanotubes for living cell interfacing and investigations," *Materials Science and Engineering C*, vol. 59, pp. 1125–1142, 2016.

[25] F. Keller, M. S. Hunter, and D. L. Robinson, "Structural Features of Oxide Coatings on Aluminum," *Journal of The Electrochemical Society*, vol. 100, no. 9, p. 411, 2007.

[26] P. Hoyer, "Formation of a Titanium Dioxide Nanotube Array," *Langmuir*, vol. 12, no. 6, pp. 1411–1413, 2002.

[27] M. Assefpour-Dezfuly, C. Vlachos, and E. H. Andrews, "Oxide morphology and adhesive bonding on titanium surfaces," *Journal of Materials Science*, vol. 19, no. 11, pp. 3626–3639, 1984.

[28] V. Zwilling, M. Aucouturier, and E. Darque-Ceretti, "Anodic Oxidation of Titanium and TA6V Alloy in Chromic Media," *Electrochimica Acta*, vol. 45, no. 6, pp. 921–929, 1999.

[29] I. Ion, "of the Ultimate Shear Strength of a Metal-Ceramic Interface," vol. 37, no. 4, pp. 1265–1270, 1989.

[30] S. Ozkan, N. Truong, A. Mazare, I. Cerri, and P. Schmuki, "Electrochemistry Communications Controlled spacing of self-organized anodic TiO 2 nanotubes," *Electrochemistry Communications*, vol. 69, pp. 76–79, 2016.

[31] J. M. Macak, H. Tsuchiya, L. Taveira, S. Aldabergerova, and P. Schmuki, "Smooth anodic TiO2 nanotubes," *Angewandte Chemie - International Edition*, vol. 44, no. 45, pp. 7463–7465, 2005.

[32] H. Tsuchiya *et al.*, "Self-organized TiO2 nanotubes prepared in ammonium fluoride containing acetic acid electrolytes," *Electrochemistry Communications*, vol. 7, no. 6, pp. 576–580, 2005.

[33] Q. Cai, L. Yang, and Y. Yu, "Investigations on the self-organized growth of TiO2 nanotube arrays by anodic oxidization," *Thin Solid Films*, vol. 515, no. 4, pp. 1802–1806, 2006.

[34] M. Paulose *et al.*, "Anodic growth of highly ordered TiO2 nanotube arrays to 134 μm in length," *Journal of Physical Chemistry B*, vol. 110, no. 33, pp. 16179–16184, 2006.

[35] S. P. Albu, A. Ghicov, J. M. Macak, and P. Schmuki, "250 μm long anodic TiO2 nanotubes with hexagonal self-ordering," *Physica Status Solidi - Rapid Research Letters*, vol. 1, no. 2, pp. 65–67, 2007.

[36] N. K. Allam and C. A. Grimes, "Formation of vertically oriented TiO2 nanotube arrays using a fluoride free HCl aqueous electrolyte," *Journal of Physical Chemistry C*, vol. 111, no. 35, pp. 13028–13032, 2007.

[37] C. Ruan, M. Paulose, O. K. Varghese, G. K. Mor, and C. A. Grimes, "Fabrication of highly ordered TiO 2 nanotube arrays using an organic electrolyte," *Journal of Physical Chemistry B*, vol. 109, no. 33, pp. 15754–15759, 2005.

[38] S. Yoriya and C. A. Grimes, "Self-Assembled TiO2 nanotube arrays by anodization of titanium in diethylene glycol: Approach to extended pore widening," *Langmuir*, vol. 26, no. 1, pp. 417–420, 2010.

[39] J. Hu *et al.*, " TiO 2 Nanotube Films Prepared by Anodization in Glycerol Solutions for Photocathodic Protection of Stainless Steel ," *Journal of The Electrochemical Society*, vol. 161, no. 4, pp. C231–C235, 2014.

[40] G. K. Mor, O. K. Varghese, M. Paulose, K. Shankar, and C. A. Grimes, "A review on highly ordered, vertically oriented TiO2 nanotube arrays: Fabrication, material properties, and solar energy applications," *Solar Energy Materials and Solar Cells*, vol. 90, no. 14, pp. 2011–2075, 2006.

[41] J. M. Tarascon and M. Armand, "Issues and challenges facing rechargeable lithium batteries.," *Nature*, vol. 414, no. 6861, pp. 359–67, 2001.

[42] Y. Cen, R. Sisson, Q. Qin, and J. Liang, "Current Progress of Si/Graphene Nanocomposites for Lithium-Ion Batteries," *C*, vol. 4, no. 1, p. 18, 2018.

[43] P. Li *et al.*, "Recent progress on silicon-based anode materials for practical lithium-ion battery applications," *Energy Storage Materials*, vol. 15, no. May, pp. 422–446, 2018.

[44] A. R. Kamali and D. J. Fray, "Tin-based materials as advanced anode materials for lithium ion batteries: A review," *Reviews on Advanced Materials Science*, vol. 27, no. 1, pp. 14–24, 2011.

[45] S. Bernard and P. Miele, "Polymer-derived boron nitride: A review on the chemistry, shaping and ceramic conversion of borazine derivatives," *Materials*, vol. 7, no. 11, pp. 7436–7459, 2014.

[46] P. Greil, "Polymer derived engineering ceramics," *Advanced Engineering Materials*, vol. 2, no. 6, pp. 339–348, 2000.

[47] A. VIARD, P. MIELE, and S. BERNARD, "Polymer-derived ceramics route toward SiCN and SiBCN fibers: from chemistry of polycarbosilazanes to the design and characterization of ceramic fibers," *Journal of the Ceramic Society of Japan*, vol. 124, no. 10, pp. 967–980, 2016.

[48] G. Mera, M. Gallei, S. Bernard, and E. Ionescu, "Ceramic Nanocomposites from Tailor-Made Preceramic Polymers," *Nanomaterials*, vol. 5, no. 2, pp. 468–540, 2015.

[49] P. Colombo, G. Mera, R. Riedel, and G. D. Sorarù, "Polymer-Derived Ceramics: 40 Years of Research and Innovation in Advanced Ceramics1)," *Ceramics Science and Technology, Applications*, vol. 4, pp. 245–320, 2013.

[50] S. Widgeon *et al.*, "Nanostructure and energetics of carbon-rich SiCN ceramics derived from polysilylcarbodiimides: Role of the nanodomain interfaces," *Chemistry of Materials*, vol. 24, no. 6, pp. 1181–1191, 2012.

[51] S. R. Shah and R. Raj, "Mechanical properties of a fully dense polymer derived ceramic made by a novel pressure casting process," *Acta Materialia*, vol. 50, no. 16, pp. 4093–4103, 2002.

[52] L. A. Liew, W. Zhang, V. M. Bright, L. An, M. L. Dunn, and R. Raj, "Fabrication of SiCN ceramic MEMS using injectable polymer-precursor technique," *Sensors and Actuators, A: Physical*, vol. 89, no. 1–2, pp. 64–70, 2001.

[53] R. RIEDEL, G. MERA, R. HAUSER, and A. KLONCZYNSKI, "Silicon-Based Polymer-

Derived Ceramics: Synthesis Properties and Applications-A Review," *Journal of the Ceramic Society of Japan*, vol. 114, no. 1330, pp. 425–444, 2006.

[54] L. An, R. Riedel, C. Konetschny, H.-J. Kleebe, and R. Raj, "Newtonian Viscosity of Amorphous Silicon Carbonitride at High Temperature," *Journal of the American Ceramic Society*, vol. 81, no. 5, pp. 1349–1352, 2010.

[55] Y. Wang, W. Fei, and L. An, "Oxidation/corrosion of polymer-derived SiAlCN ceramics in water vapor," *Journal of the American Ceramic Society*, vol. 89, no. 3, pp. 1079–1082, 2006.

[56] I. Saleh and R. Raj, "Three-dimensional architecture of lithium-anodes made from graphite fibers coated with thin-films of silicon oxycarbide: Design, performance and manufacturability," *Journal of Power Sources*, vol. 310, pp. 18–25, 2016.

[57] P. E. Sanchez-Jimenez and R. Raj, "Lithium insertion in polymer-derived silicon oxycarbide ceramics," *Journal of the American Ceramic Society*, vol. 93, no. 4, pp. 1127–1135, 2010.

[58] H. G. Moon *et al.*, "Self-activated ultrahigh chemosensitivity of oxide thin film nanostructures for transparent sensors," *Scientific Reports*, vol. 2, pp. 1–7, 2012.

[59] M. Phillips *et al.*, "Volatile organic compounds in breath as markers of lung cancer: A cross-sectional study," *Lancet*, vol. 353, no. 9168, pp. 1930–1933, 1999.

[60] A. Dey, "Semiconductor metal oxide gas sensors: A review," *Materials Science and Engineering B: Solid-State Materials for Advanced Technology*, vol. 229, no. December 2017, pp. 206–217, 2018.

[61] T. Anukunprasert, C. Saiwan, and E. Traversa, "The development of gas sensor for carbon monoxide monitoring using nanostructure of Nb-TiO2," *Science and Technology of Advanced Materials*, vol. 6, no. 3-4 SPEC. ISS., pp. 359–363, 2005.

[62] M. Righettoni, A. Amann, and S. E. Pratsinis, "Breath analysis by nanostructured metal oxides as chemo-resistive gas sensors," *Materials Today*, vol. 18, no. 3, pp. 163–171, 2015.

[63] J. P. Dakin and P. Chambers, "REVIEW OF METHODS OF OPTICAL GAS Detection by Direct Optical Spectroscopy, with Emphasis on Correlation Spectroscopy," *Optical Chemical Sensors*, pp. 457–477, 2006.

[64] B. W. H. Brattain and J. Bardeent, "The Bell System Surface Properties of Germanium," *American Telephone and Telegraph Company*, vol. 32, pp. 1–41, 1952.

[65] T. Seiyama, A. Kato, K. Fujiishi, and M. Nagatani, "A New Detector for Gaseous Components Using Semiconductive Thin Films," *Analytical Chemistry*, vol. 34, no. 11, pp. 1502–1503, 1962.

[66] N. Taguchi, "Gas detecting device," *US patent*, vol. 3, no. 631, p. 436, 1971.

[67] Z. Zhang and P. Wang, "Optimization of photoelectrochemical water splitting performance on hierarchical TiO2 nanotube arrays," *Energy & Environmental Science*, vol. 5, p. 6506, 2012.

[68] S. S. Mao, X. B. Chen, L. Liu, and P. Y. Yu, "Increasing Solar Absorption for

Photocatalysis with Black Hydrogenated Titanium Dioxide Nanocrystals," *Science*, vol. 331, no. 6018, pp. 746–750, 2011.

[69] S. Piskunov *et al.*, "C-, N-, S-, and Fe-Doped TiO2 and SrTiO3 Nanotubes for Visible-Light-Driven Photocatalytic Water Splitting: Prediction from First Principles," *The Journal of Physical Chemistry C*, p. 150730154333006, 2015.

[70] B. O'Regan and M. Grätzel, "A low-cost, high-efficiency solar cell based on dye-sensitized colloidal TiO2 films," *Nature*, vol. 353, pp. 737–740, 1991.

[71] A. L. Linsebigler, G. Q. Lu, and J. T. Yates, "Photocatalysis on Tio2 Surfaces - Principles, Mechanisms, and Selected Results," *Chemical reviews*, vol. 95, no. 3, pp. 735–758, 1995.

[72] S. C. Roy, O. K. Varghese, M. Paulose, and C. A. Grimes, "Toward Solar Fuels: Photocatalytic Conversion of Carbon Dioxide to Hydrocarbons," *Acs Nano*, vol. 4, no. 3, pp. 1259–1278.

[73] X. Chen and S. S. Mao, "Titanium dioxide nanomaterials: Synthesis, properties, modifications and applications," *Chemical Reviews*, vol. 107, no. 7, pp. 2891–2959, 2007.

[74] Y. Ma, X. L. Wang, Y. S. Jia, X. B. Chen, H. X. Han, and C. Li, "Titanium Dioxide-Based Nanomaterials for Photocatalytic Fuel Generations," *Chemical Reviews*, vol. 114, no. 19, pp. 9987–10043, 2014.

[75] J. Schneider *et al.*, "Understanding TiO2 Photocatalysis: Mechanisms and Materials," *Chemical Reviews*, vol. 114, no. 19, pp. 9919–9986, 2014.

[76] V. Singh, I. J. C. Beltran, J. C. Ribot, and P. Nagpal, "Photocatalysis deconstructed: Design of a new selective catalyst for artificial photosynthesis," *Nano Letters*, vol. 14, no. 2, pp. 597–603, 2014.

[77] P. Roy, S. Berger, and P. Schmuki, "TiO2 nanotubes: Synthesis and applications," *Angewandte Chemie - International Edition*, vol. 50, no. 13, pp. 2904–2939, 2011.

[78] Y. Alivov, H. H. Funke, V. Singh, and P. Nagpal, "Air-pressure tunable depletion width, rectification behavior, and charge conduction in oxide nanotubes," *ACS Applied Materials and Interfaces*, vol. 7, no. 4, pp. 2153–2159, 2015.

[79] Y. Alivov, H. Funke, and P. Nagpal, "Air-gating and chemical-gating in transistors and sensing devices made from hollow TiO2semiconductor nanotubes," *Nanotechnology*, vol. 26, no. 29, 2015.

[80] V. Galstyan, E. Comini, G. Faglia, and G. Sberveglieri, "TiO2 Nanotubes: Recent Advances in Synthesis and Gas Sensing Properties," *Sensors*, vol. 13, no. 11, pp. 14813–14838, 2013.

[81] J. Lee, D. H. Kim, S. H. Hong, and J. Y. Jho, "A hydrogen gas sensor employing vertically aligned TiO2 nanotube arrays prepared by template-assisted method," *Sensors and Actuators, B: Chemical*, vol. 160, no. 1, pp. 1494–1498, 2011.

[82] A. Amann and D. Smith, *Volatile Biomarkers*. 2013.

[83] T. Malwela, B. Mwakikunga, M. Beukes, V. Saasa, C.-P. Liu, and M. Mokgotho, "Sensing Technologies for Detection of Acetone in Human Breath for Diabetes Diagnosis and Monitoring," *Diagnostics*, vol. 8, no. 1, p. 12, 2018.

[84] Y. Ding and P. Nagpal, “Titanium dioxide nanotube membranes for solar energy conversion: effect of deep and shallow dopants,” *Phys. Chem. Chem. Phys. Phys. Chem. Chem. Phys*, vol. 19, no. 19, pp. 10042–10050, 1004.

[85] R. Asahi, T. Morikawa, T. Ohwaki, K. Aoki, and Y. Taga, “0334.Science2001,293,269.pdf,” vol. 293, no. July, pp. 2000–2002, 2001.

[86] K. Huo *et al.*, “Carbon-Doped TiO₂ Nanotube Array Platform for Visible Photocatalysis,” *Nanoscience and Nanotechnology Letters*, vol. 5, no. 12, pp. 1251–1257, 2013.

[87] D. D. Qin *et al.*, “Phosphorus-doped TiO2 nanotube arrays for visible-light-driven photoelectrochemical water oxidation,” *Sustainable Energy and Fuels*, vol. 1, no. 2, pp. 248–253, 2017.

[88] N. Lu, H. Zhao, J. Li, X. Quan, and S. Chen, “Characterization of boron-doped TiO2 nanotube arrays prepared by electrochemical method and its visible light activity,” *Separation and Purification Technology*, vol. 62, no. 3, pp. 668–673, 2008.

[89] S. W. Shin, J. Y. Lee, K. S. Ahn, S. H. Kang, and J. H. Kim, “Visible light absorbing TiO<inf>2</inf> nanotube arrays by sulfur treatment for photoelectrochemical water splitting,” *Journal of Physical Chemistry C*, vol. 119, no. 24, pp. 13375–13383, 2015.

[90] M. M. Momeni, Y. Ghayeb, and Z. Ghonchegi, “Fabrication and characterization of copper doped TiO<inf>2</inf> nanotube arrays by in situ electrochemical method as efficient visible-light photocatalyst,” *Ceramics International*, vol. 41, no. 7, pp. 8735–8741, 2015.

[91] H. Liu, G. Liu, and Q. Zhou, “Preparation and characterization of Zr doped TiO2 nanotube arrays on the titanium sheet and their enhanced photocatalytic activity,” *Journal of Solid State Chemistry*, vol. 182, no. 12, pp. 3238–3242, 2009.

[92] A. Ghicov, B. Schmidt, J. Kunze, and P. Schmuki, “Photoresponse in the visible range from Cr doped TiO2 nanotubes,” *Chemical Physics Letters*, vol. 433, no. 4–6, pp. 323–326, 2007.

[93] F. P. Ã, L. Cai, H. Yu, H. Wang, and J. Yang, “Synthesis and characterization of substitutional and interstitial nitrogen-doped titanium dioxides with visible light photocatalytic activity,” vol. 181, pp. 130–136, 2008.

[94] B. Prajapati, “Investigation of the physical properties of Fe : TiO 2 -diluted magnetic semiconductor nanoparticles,” pp. 4257–4267, 2017.

[95] T. M. Suzuki, G. Kitahara, T. Arai, Y. Matsuoka, and T. Morikawa, “Nitrogen and transition-metal codoped titania nanotube arrays for visible-light-sensitive photoelectrochemical water oxidation,” *Chemical Communications*, vol. 50, no. 57, pp. 7614–7616, 2014.

[96] M. Zhang, D. Lu, G. Yan, J. Wu, and J. Yang, “Fabrication of Mo+N-codoped TiO2 nanotube arrays by anodization and sputtering for visible light-induced photoelectrochemical and photocatalytic properties,” *Journal of Nanomaterials*, vol. 2013, 2013.

[97] T. Cottineau *et al.*, “One step synthesis of niobium doped titania nanotube arrays to form

(N,Nb) co-doped TiO<inf>2</inf> with high visible light photoelectrochemical activity," *Journal of Materials Chemistry A*, vol. 1, no. 6, pp. 2151–2160, 2013.

[98] D. Lu, M. Zhang, Z. Zhang, Q. Li, X. Wang, and J. Yang, "Self-organized vanadium and nitrogen co-doped titania nanotube arrays with enhanced photocatalytic reduction of CO2 into CH4," *Nanoscale Research Letters*, vol. 9, no. 1, pp. 1–9, 2014.

[99] M. Zhang, J. Wu, D. Lu, and J. Yang, " Enhanced Visible Light Photocatalytic Activity for TiO 2 Nanotube Array Films by Codoping with Tungsten and Nitrogen ," *International Journal of Photoenergy*, vol. 2013, pp. 1–8, 2013.

[100] A. Mohamed, S. Barghi, and S. Rohani, "N- and C-Modified TiO2 Nanotube Arrays: Enhanced Photoelectrochemical Properties and Effect of Nanotubes Length on Photoconversion Efficiency," *Nanomaterials*, vol. 8, no. 4, p. 198, 2018.

[101] G. Yan, M. Zhang, J. Hou, and J. Yang, "Photoelectrochemical and photocatalytic properties of N + S co-doped TiO2nanotube array films under visible light irradiation," *Materials Chemistry and Physics*, vol. 129, no. 1–2, pp. 553–557, 2011.

[102] J. Bisquert, "Theory of the impedance of charge transfer via surface states in dye-sensitized solar cells," *Journal of Electroanalytical Chemistry*, vol. 646, no. 1–2, pp. 43–51, 2010.

[103] R. Kern, R. Sastrawan, J. Ferber, R. Stangl, and J. Luther, "Modeling and interpretation of electrical impedance spectra of dye solar cells operated under open-circuit conditions," *Electrochimica Acta*, vol. 47, pp. 4213–4225, 2002.

[104] J. F. McCann, "Equivalent Circuit Analysis of the Impedance Response of Semiconductor/Electrolyte/Counterelectrode Cells," *Journal of The Electrochemical Society*, vol. 129, p. 551, 1982.

[105] R. Memming, *Semiconductor Electrochemistry*. Wiley, 2015.

[106] Z. Chen, H. N. N. Dinh, and E. Miller, *Photoelectrochemical water splitting : standards, experimental methods, and protocols*. .

[107] N. Baram and Y. Ein-Eli, "Electrochemical impedance spectroscopy of porous TiO2 for photocatalytic applications," *Journal of Physical Chemistry C*, vol. 114, pp. 9781–9790, 2010.

[108] P. Nagpal and V. I. Klimov, "Role of mid-gap states in charge transport and photoconductivity in semiconductor nanocrystal films," *Nature Communications*, vol. 2, p. 7, 2011.

[109] J. B. Goodenough and K. S. Park, "The Li-ion rechargeable battery: A perspective," *Journal of the American Chemical Society*, vol. 135, no. 4, pp. 1167–1176, 2013.

[110] B. Scrosati, J. Hassoun, and Y. K. Sun, "Lithium-ion batteries. A look into the future," *Energy and Environmental Science*, vol. 4, no. 9, pp. 3287–3295, 2011.

[111] T. R. Jow, S. A. Delp, J. L. Allen, J.-P. Jones, and M. C. Smart, " Factors Limiting Li + Charge Transfer Kinetics in Li-Ion Batteries ," *Journal of The Electrochemical Society*, vol. 165, no. 2, pp. A361–A367, 2018.

[112] Ali Reza Kamali and Derek J. Fray, "Review on Carbon and Silicon Based Materials as

Anode Materials for Lithium Ion Batteries," *Journal of New Materials for Electrochemical Systems*, vol. 13, pp. 147–160, 2010.

[113] P. Onnerud, J. Shi, R. Chamberlain, S. K. Singh, and B. Barnett, "Benchmarking Graphite Materials Used as Anodes in Lithium-Ion Batteries," p. 100.

[114] J. Liu, D. R. Vissers, K. Amine, I. V. Barsukov, and J. E. Doninger, "Surface Treated Natural Graphite As Anode Material for High-Power Li-Ion Battery Applications," *New Carbon Based Materials for Electrochemical Energy Storage Systems: Batteries, Supercapacitors and Fuel Cells*, pp. 283–292, 2006.

[115] P. G. Stansberry and A. H. Stiller, "Learn more about Carbon Anode Coal-Derived Carbons THERMAL PROPERTIES OF GRAVI- TY-FREE GAS-ARC DISCHARGE MEA-," 1999.

[116] L. Liang, Y. Qi, F. Xue, S. Bhattacharya, S. J. Harris, and L. Q. Chen, "Nonlinear phase-field model for electrode-electrolyte interface evolution," *Physical Review E - Statistical, Nonlinear, and Soft Matter Physics*, vol. 86, no. 5, pp. 1–5, 2012.

[117] S. J. An, J. Li, C. Daniel, D. Mohanty, S. Nagpure, and D. L. Wood, "The state of understanding of the lithium-ion-battery graphite solid electrolyte interphase (SEI) and its relationship to formation cycling," *Carbon*, vol. 105, pp. 52–76, 2016.

[118] M. Noel and R. Santhanam, "Electrochemistry of graphite intercalation compounds," *Journal of Power Sources*, vol. 72, no. 1, pp. 53–65, 1998.

[119] A. Maraschky and R. Akolkar, " Mechanism Explaining the Onset Time of Dendritic Lithium Electrodeposition via Considerations of the Li + Transport within the Solid Electrolyte Interphase ," *Journal of The Electrochemical Society*, vol. 165, no. 14, pp. D696–D703, 2018.

[120] L. Li, S. Li, and Y. Lu, "Suppression of dendritic lithium growth in lithium metal-based batteries," *Chemical Communications*, vol. 54, no. 50, pp. 6648–6661, 2018.

[121] O. Rhee, G. Lee, and J. Choi, "Highly Ordered TiO2 Microcones with High Rate Performance for Enhanced Lithium-Ion Storage," *ACS Applied Materials and Interfaces*, vol. 8, no. 23, pp. 14558–14563, 2016.

[122] F. Di Lupo *et al.*, "Mesoporous TiO 2 nanocrystals produced by a fast hydrolytic process as high-rate long-lasting Li-ion battery anodes," *Acta Materialia*, vol. 69, pp. 60–67, 2014.

[123] Z. Ren *et al.*, "Preparation of carbon-encapsulated ZnO tetrahedron as an anode material for ultralong cycle life performance lithium-ion batteries," *Electrochimica Acta*, vol. 146, pp. 52–59, 2014.

[124] H. Jiang, Y. Hu, S. Guo, C. Yan, P. S. Lee, and C. Li, "Rational design of MnO/carbon nanopeapods with internal void space for high-rate and long-life li-ion batteries," *ACS Nano*, vol. 8, no. 6, pp. 6038–6046, 2014.

[125] J. Kim and J. Cho, "Rate Characteristics of Anatase TiO[sub 2] Nanotubes and Nanorods for Lithium Battery Anode Materials at Room Temperature," *Journal of The Electrochemical Society*, vol. 154, no. 6, p. A542, 2007.

[126] M. Madian *et al.*, "Anodically fabricated TiO2-SnO2 nanotubes and their application in lithium ion batteries," *Journal of Materials Chemistry A*, vol. 4, no. 15, pp. 5542–5552, 2016.

[127] M. Anji Reddy, V. Pralong, U. V. Varadaraju, and B. Raveau, "Crystallite Size Constraints on Lithium Insertion into Brookite TiO[sub 2]," *Electrochemical and Solid-State Letters*, vol. 11, no. 8, p. A132, 2008.

[128] D. Dambournet, I. Belharouak, and K. Amine, "Tailored preparation methods of TiO2 anatase, rutile, brookite: Mechanism of formation and electrochemical properties," *Chemistry of Materials*, vol. 22, no. 3, pp. 1173–1179, 2010.

[129] M. Mancini, P. Kubiak, M. Wohlfahrt-Mehrens, and R. Marassi, "Mesoporous Anatase TiO[sub 2] Electrodes Modified by Metal Deposition: Electrochemical Characterization and High Rate Performances," *Journal of The Electrochemical Society*, vol. 157, no. 2, p. A164, 2009.

[130] T. Ohzuku, T. Kodama, and T. Hirai, "Electrochemistry of anatase titanium dioxide in lithium nonaqueous cells," *Journal of Power Sources*, vol. 14, no. 1–3, pp. 153–166, 1985.

[131] T. Fröschl *et al.*, "High surface area crystalline titanium dioxide: Potential and limits in electrochemical energy storage and catalysis," *Chemical Society Reviews*, vol. 41, no. 15, pp. 5313–5360, 2012.

[132] Y. S. Hu, L. Kienle, Y. G. Guo, and J. Maier, "High lithium electroactivity of nanometer-sized rutile TiO2," *Advanced Materials*, vol. 18, no. 11, pp. 1421–1426, 2006.

[133] E. Baudrin, S. Cassaignon, M. Koelsch, J. P. Jolivet, L. Dupont, and J. M. Tarascon, "Structural evolution during the reaction of Li with nano-sized rutile type TiO2 at room temperature," *Electrochemistry Communications*, vol. 9, no. 2, pp. 337–342, 2007.

[134] P. Kubiak *et al.*, "Electrochemical evaluation of rutile TiO2 nanoparticles as negative electrode for Li-ion batteries," *Journal of Power Sources*, vol. 194, no. 2, pp. 1099–1104, 2009.

[135] H. Usui, Y. Domi, S. Yoshioka, K. Kojima, and H. Sakaguchi, "Electrochemical Lithiation and Sodiation of Nb-Doped Rutile TiO 2," *ACS Sustainable Chemistry and Engineering*, vol. 4, no. 12, pp. 6695–6702, 2016.

[136] M. Madian, A. Eychmüller, and L. Giebeler, "Current Advances in TiO2-Based Nanostructure Electrodes for High Performance Lithium Ion Batteries," *Batteries*, vol. 4, no. 1, p. 7, 2018.

[137] Y. X. Wang, J. Xie, G. S. Cao, T. J. Zhu, and X. B. Zhao, "Electrochemical performance of TiO 2 /carbon nanotubes nanocomposite prepared by an in situ route for Li-ion batteries," *Journal of Materials Research*, vol. 27, no. 2, pp. 417–423, 2012.

[138] H. Huang *et al.*, "Hybrid nanoarchitecture of TiO2 nanotubes and graphene sheet for advanced lithium ion batteries," *Materials Research Bulletin*, vol. 96, pp. 425–430, 2017.

[139] R. V. Chernozem, M. A. Surmeneva, and R. A. Surmenev, "Influence of Anodization Time and Voltage on the Parameters of TiO2 Nanotubes," *IOP Conference Series: Materials Science and Engineering*, vol. 116, no. 1, 2016.

[140] K. Srimuangmak and S. Niyomwas, “Effects of voltage and addition of water on photocatalytic activity of TiO2nanotubes prepared by anodization method,” *Energy Procedia*, vol. 9, pp. 435–439, 2011.

[141] A. Haring, A. Morris, and M. Hu, “Controlling morphological parameters of anodized titania nanotubes for optimized solar energy applications,” *Materials*, vol. 5, no. 10, pp. 1890–1909, 2012.

[142] T. H. Kim, G.-M. Go, H.-B. Cho, Y. Song, C.-G. Lee, and Y.-H. Choa, “A Novel Synthetic Method for N Doped TiO2 Nanoparticles Through Plasma-Assisted Electrolysis and Photocatalytic Activity in the Visible Region,” *Frontiers in Chemistry*, vol. 6, no. October, pp. 1–10, 2018.

[143] W. J. H. Borghols *et al.*, “Lithium Storage in Amorphous TiO[sub 2] Nanoparticles,” *Journal of The Electrochemical Society*, vol. 157, no. 5, p. A582, 2010.

[144] Z. Guo, X. Dong, D. Zhou, Y. Du, Y. Wang, and Y. Xia, “TiO2(B) nanofiber bundles as a high performance anode for a Li-ion battery,” *RSC Advances*, vol. 3, no. 10, pp. 3352–3358, 2013.

[145] F. F. Cao, S. Xin, Y. G. Guo, and L. J. Wan, “Wet chemical synthesis of Cu/TiO2 nanocomposites with integrated nano-current-collectors as high-rate anode materials in lithium-ion batteries,” *Physical Chemistry Chemical Physics*, vol. 13, no. 6, pp. 2014–2020, 2011.

[146] Y. Xiao, C. Hu, and M. Cao, “Compositing amorphous TiO2 with N-doped carbon as high-rate anode materials for lithium-ion batteries,” *Chemistry - An Asian Journal*, vol. 9, no. 1, pp. 351–356, 2014.

[147] J. Duan *et al.*, “In situ Ti3+-doped TiO2nanotubes anode for lithium ion battery,” *Journal of Porous Materials*, vol. 23, no. 3, pp. 837–843, 2016.

[148] M. Fehse *et al.*, “Nb-doped TiO2 nanofibers for lithium ion batteries,” *Journal of Physical Chemistry C*, vol. 117, no. 27, pp. 13827–13835, 2013.

[149] A. Saha, R. Raj, and D. L. Williamson, “A model for the nanodomains in polymer-derived SiCO,” *Journal of the American Ceramic Society*, vol. 89, no. 7, pp. 2188–2195, 2006.

[150] P. D. Weidman, D. Ahn, and R. Raj, “Diffusive relaxation of Li in particles of silicon oxycarbide measured by galvanostatic titrations,” *Journal of Power Sources*, vol. 249, pp. 219–230, 2014.

[151] D. Ahn and R. Raj, “Cyclic stability and C-rate performance of amorphous silicon and carbon based anodes for electrochemical storage of lithium,” *Journal of Power Sources*, vol. 196, no. 4, pp. 2179–2186, 2011.

[152] H. Fukui, H. Ohsuka, T. Hino, and K. Kanamura, “Influence of polystyrene/phenyl substituents in precursors on microstructures of Si-O-C composite anodes for lithium-ion batteries,” *Journal of Power Sources*, vol. 196, no. 1, pp. 371–378, 2011.

[153] D. Ahn and R. Raj, “Thermodynamic measurements pertaining to the hysteretic intercalation of lithium in polymer-derived silicon oxycarbide,” *Journal of Power Sources*, vol. 195, no. 12, pp. 3900–3906, 2010.

[154] J. Shen and R. Raj, "Silicon-oxycarbide based thin film anodes for lithium ion batteries," *Journal of Power Sources*, vol. 196, no. 14, pp. 5945–5950, 2011.

[155] L. Zoli, D. Sciti, L. A. Liew, K. Terauds, S. Azarnoush, and R. Raj, "Additive Manufacturing of Ceramics Enabled by Flash Pyrolysis of Polymer Precursors with Nanoscale Layers," *Journal of the American Ceramic Society*, vol. 99, no. 1, pp. 57–63, 2016.

[156] T. J. Cross, R. Raj, S. V. Prasad, and D. R. Tallant, "Synthesis and tribological behavior of silicon oxycarbonitride thin films derived from poly(Urea)methyl vinyl silazane," *International Journal of Applied Ceramic Technology*, vol. 3, no. 2, pp. 113–126, 2006.

[157] A. M. Wilson, G. Zank, K. Eguchi, W. Xing, and J. R. Dahn, "Pyrolysed silicon-containing polymers as high capacity anodes for lithium-ion batteries," *Journal of Power Sources*, vol. 68, no. 2, pp. 195–200, 1997.

[158] L. Yu and R. Raj, "On the thermodynamically stable amorphous phase of polymer-derived silicon oxycarbide," *Scientific Reports*, vol. 5, no. iii, pp. 1–13, 2015.

[159] J. R. Dahn, T. Zheng, Y. Liu, and J. S. Xue, "Lithium Insertion Mechanisms for in Carbonaceous Materials," *Advancement Of Science*, vol. 270, no. 5236, pp. 590–593, 2011.

[160] Y. Wang, T. Wu, Y. Zhou, C. Meng, W. Zhu, and L. Liu, *Tio 2 -based nanoheterostructures for promoting gas sensitivity performance: Designs, developments, and prospects*, vol. 17, no. 9. 2017.

[161] Y. J. Choi, I. S. Hwang, J. G. Park, K. J. Choi, J. H. Park, and J. H. Lee, "Novel fabrication of an SnO2 nanowire gas sensor with high sensitivity," *Nanotechnology*, vol. 19, no. 9, 2008.

[162] B. Cao, J. Chen, X. Tang, and W. Zhou, "Growth of monoclinic WO3 nanowire array for highly sensitive NO2 detection," *Journal of Materials Chemistry*, vol. 19, no. 16, pp. 2323–2327, 2009.

[163] L. Zhu and W. Zeng, "Room-temperature gas sensing of ZnO-based gas sensor: A review," *Sensors and Actuators, A: Physical*, vol. 267, pp. 242–261, 2017.

[164] S. P. Patil *et al.*, "Spray pyrolyzed indium oxide thick films as NO 2 gas sensor," *Ceramics International*, vol. 42, no. 14, pp. 16160–16168, 2016.

[165] E. Şennik, Z. Çolak, N. Kilinç, and Z. Z. Öztürk, "Synthesis of highly-ordered TiO2 nanotubes for a hydrogen sensor," *International Journal of Hydrogen Energy*, vol. 35, no. 9, pp. 4420–4427, 2010.

[166] H. Miyazaki, T. Hyodo, Y. Shimizu, and M. Egashira, "Hydrogen-sensing properties of anodically oxidized TiO2 film sensors," *Sensors and Actuators B: Chemical*, vol. 108, no. 1–2, pp. 467–472, 2004.

[167] S. Joo, I. Muto, and N. Hara, "Hydrogen Gas Sensor Using Pt- and Pd-Added Anodic TiO[sub 2] Nanotube Films," *Journal of The Electrochemical Society*, vol. 157, no. 6, p. J221, 2010.

[168] Y. Alivov, H. Funke, and P. Nagpal, "Air-gating and chemical-gating in transistors and

sensing devices made from hollow TiO2 semiconductor nanotubes," *Nanotechnology*, vol. 26, no. 29, 2015.

[169] R. Fujimura, R. Zhang, Y. Kitamoto, M. Shimojo, and K. Kajikawa, "Modeling of semi-shell nanostructures formed by metal deposition on dielectric nanospheres and numerical evaluation of plasmonic properties," *Japanese Journal of Applied Physics*, vol. 53, no. 3, pp. 143–167, 2014.

[170] F. Léonard, A. A. Talin, B. S. Swartzentruber, and S. T. Picraux, "Diameter-dependent electronic transport properties of Au-Catalyst/Ge- nanowire Schottky diodes," *Physical Review Letters*, vol. 102, no. 10, pp. 1–4, 2009.